UNIVERSITY OF SÃO PAULO

SCHOOL OF ENGINEERING OF SÃO CARLOS

PEDRO RENATO TAVARES AVILA

Manufacture and optimization of nanostructured Cr-Al-N coatings produced by reactive magnetron sputtering

São Carlos

2021

UNIVERSIDADE DE SÃO PAULO

ESCOLA DE ENGENHARIA DE SÃO CARLOS

PEDRO RENATO TAVARES AVILA

Manufacture and optimization of nanostructured Cr-Al-N coatings produced by reactive magnetron sputtering

Versão Corrigida

Tese apresentada ao programa de Pós-Graduação em Ciência e Engenharia de Materiais da Universidade de São Paulo, como parte dos requisitos para obtenção do título de Doutor em Ciências.

Área de concentração: Desenvolvimento, Caracterização e Aplicação de Materiais.

Orientador(a): Haroldo Cavalcanti Pinto

São Carlos

2021

Ficha catalográfica elaborada pela Biblioteca Prof. Dr. Sérgio Rodrigues Fontes da EESC/USP com os dados inseridos pelo(a) autor(a).

T231m

Tavares Avila, Pedro Renato
Manufacture and optimization of nanostructured Cr-Al-N coatings produced by reactive magnetron sputtering / Pedro Renato Tavares Avila; orientador Haroldo Cavalcanti Pinto. São Carlos, 2021.

Tese (Doutorado) - Programa de Pós-Graduação em Ciência e Engenharia de Materiais e Área de Concentração em Desenvolvimento, Caracterização e Aplicação de Materiais -- Escola de Engenharia de São Carlos da Universidade de São Paulo, 2021.

1. Cr-Al-N. 2. Coatings. 3. Magnetron Sputtering. 4. HiPIMS. 5. DCMS. 6. DGLAD. I. Título.

Eduardo Graziosi Silva - CRB - 8/8907

FOLHA DE JULGAMENTO

Candidato: Engenheiro **PEDRO RENATO TAVARES AVILA.**

Título da dissertação: "Manufatura e otimização de recobrimentos nanoestruturados de Cr-Al-N produzidos por pulverização catódica reativa".

Data da defesa: 24/03/2021.

Comissão Julgadora	**Resultado**
Prof. Associado **Haroldo Cavalcanti Pinto (Orientador)** (Escola de Engenharia de São Carlos/EESC)	**APROVADO**
Prof. Dr. **Conrado Ramos Moreira Afonso** (Universidade Federal de São Carlos/UFSCar)	**APROVADO**
Dr. **Juliano Avelar Araujo** (Mahle Metal Leva SA)	**APROVADO**
Prof. Dr. **Pedro Augusto de Paula Nascente** (Universidade Federal de São Carlos/UFSCar)	**APROVADO**
Prof. Dr. **Roberto Martins de Souza** (Escola Politécnica/EP-USP)	**APROVADO**

Coordenador do Programa de Pós-Graduação em Engenharia de Materiais:
Prof. Associado **Marcelo Falcão de Oliveira**

Presidente da Comissão de Pós-Graduação:
Prof. Titular **Murilo Araujo Romero**

Aos meus queridos pais Donizeti e Rosângela, ao meu irmão Matheus e à minha esposa Mariana, pois sem o apoio de vocês esta tese seria impossível.

Acknowledgments

To professor Dr. Haroldo Cavalcanti Pinto for his supervising, guidance, teachings, and dedication that were fundamental for the development and success of this work.

To my friends and collaborators, professors Dr. Alisson Mendes Rodrigues, Dr. Erenilton Pereira da Silva and Dr. Julian Arnaldo Avila Diaz for the support, discussions, and teamwork.

To my colleagues and friends of laboratory at the group of Physicall Metallurgy, Raíra Chefer Apolinário, Maiara Moreno, Bruno César Noronha Marques de Castilho, Monica Costa Rodrigues Guimarães, Bruna Callegari, Leandro Guimarães and Valdir Boldin.

To the technical staff of the Materials Engineering Department at EESC-USP for the support in the production and characterization of the samples. Particularly to Dr. Alberto Cury, Ms. Wagner Correr, Ms. Ricardo Gomes and Denílson Vila.

To the undergraduate interns that worked with me at the Physical Metallurgy group and did part of the experimental work present in this thesis, Pedro Cornachioni, André Vianna, Caio Gora and Gustavo Bertolli and specially to Anna Meierfrankenfeld, who became a friend.

To professor Dr. Magdalena Walczak and her student Fabíola Piñera from PUC-Chile for the GDOES measurements and professor Dr. Flavio Soldera and his student Katherine Aristizíbal from Saarland University for several FIB preparations.

To the National Council for Scientific and Technological Development (CNPq) for the funding of this work (process number 165060/2017-4).

To the Brazilian National Nanotechnology Laboratory (LNNano-CNPEM) for the access to their facilities and support in the electronic microscopy analysis. I specially acknowledge Fabiano Emmanuel Montoro and Dr. Jefferson Bettini for the preparation

of FIB lamellas and for training me to operate the transmission electron microscope, respectively.

To the São Carlos School of Engineering and to the Department of Materials Engineering for providing the required infrastructure for the development of this project.

To all the friends I made in all those years of USP with which I shared good times!

“Não diga que a vitória está perdida se é de batalhas que se vive a vida.”

Raul Seixas.

RESUMO

AVILA, P. R. T**. Manufatura e otimização de recobrimentos nanoestruturados de Cr-Al-N produzidos por pulverização catódica reativa.** 135 p. Tese (Doutorado) – Escola de Engenharia de São Carlos, Universidade de São Paulo, São Carlos, 2021.

A deposição de recobrimentos cerâmicos duros é fundamental na engenharia de superfícies como uma das estratégias para proteção de superfícies metálicas contra condições de desgaste severo em aplicações industriais. Dentre as opções de materiais disponíveis para essa finalidade, nitretos de metais de transição são algumas das mais comuns. Cr-Al-N apresenta interessantes propriedades mecânicas e de resistência à oxidação, sendo uma opção relevante. Além da escolha do material, a via de deposição é um importante parâmetro a ser levado em consideração e estudado em detalhes quando se desenvolve soluções de recobrimentos. Nesta tese, recobrimentos de Cr-Al-N foram depositados sobre substratos de aço inoxidável fazendo uso das técnicas de HiPIMS e dcMS. O impacto da escolha de técnicas e de seus parâmetros nas propriedades dos filmes foram investigados. Os recobrimentos apresentaram altos teores de N, provavelmente devido ao processo de envenenamento dos alvos ricos em Al durante a pulverização catódica reativa. As amostras produzidas usando alvos precursores com composição atômica de 70/30 % Al/Cr mostram propriedades mecânicas mais relevantes do ponto de vista de dureza e H^3/Er^2 devido à adição de maiores quantidades de Al em solução sólida. Os filmes produzidos por HiPIMS apresentaram maior dureza e densificação em comparação aos produzidos por dcMS devido à maior taxa de ionização, e subsequente maior energia de deposição da técnica pulsada. Os nitretos foram fabricados utilizando uma técnica recentemente desenvolvida, em que o substrato é continuamente oscilado na frente do alvo durante a deposição, garantindo a variação constante do ângulo de chegada do fluxo de material proveniente do alvo com relação à superfície da amostra. Esta técnica recebeu o nome de DGLAD (*Dynamic Glancing Angle Deposition*). A variação no ângulo de incidência do fluxo causa a formação de nanoestruturas ao longo do filme, com grãos apresentando formatos corrugados. Observou-se que estas estruturas geram gradientes de *misorientations* ao longo dos grãos, e em combinação com a natureza em zigue zague dos contornos de grãos são capazes de aumentar a

dureza e a resistência ao desgaste dos recobrimentos, especialmente quando fabricados utilizando-se grandes limites de ângulos de oscilação. A técnica DGLAD se mostrou capaz de controlar positivamente o desempenho e a taxa de deposição dos filmes de Cr-Al-N, posicionando-se como uma importante alternativa para aplicações industriais.

Palavras-chave: Cr-Al-N. Recobrimentos. Pulverização Catódica. HiPIMS. DCMS. DGLAD

ABSTRACT

AVILA, P. R. T**. Manufacture and optimization of nanostructured Cr-Al-N coatings produced by reactive magnetron sputtering.** 135 p. Tese (Doutorado) – Escola de Engenharia de São Carlos, Universidade de São Paulo, São Carlos, 2021.

Deposition of ceramic hard coatings are paramount in surface engineering as a strategy for protecting metallic surfaces of severe wear, many times present in industrial applications. Among the options of materials for this purpose, the transition metal nitrides are some of the most common. Cr-Al-N present interesting mechanical and anti-oxidation properties. Along with the choice of materials, the route of deposition is a major parameter to be taken in consideration and thoroughly studied to optimize the performance of the film solution. In this thesis, Cr-Al-N coatings were deposited over stainless steel substrate using dcMS and HiPIMS and its impact on the properties of the films were investigated. The coatings presented high concentration of N, possibly due to target poisoning during reactive depositions. The samples produced using 70/30 at % target exhibited better mechanical performance as consequence of the larger amount of Al in solid solution. HiPIMS films presented improved properties and densification caused by the higher ionization and consequently higher energy in comparison with dcMS manufactured samples. The nitride coatings were produced using a novel technique in which the substrate is oscillated continuously in front of the target to produce nanostructured coatings by varying the angle of incidence of the sputtered material. This technique named Dynamic Glancing Angle Deposition (DGLAD) was found responsible for creating misorientation gradients along the grains. These features combined with the zigzag shape of grain boundaries contributed to enhancement in hardness and wear resistance, especially when larger oscillatory ranges were used. DGLAD is proved as a technique capable of positively influence microstructure, deposition rate and mechanical performance of the Cr-Al-N coatings.

Keywords: Cr-Al-N. Coatings. Magnetron Sputtering. HiPIMS. DCMS. DGLAD

LIST OF FIGURES

LIST OF TABLES

LIST OF ABREVIATIONS

TM – Transition Metal
CVD – Chemical Vapor Deposition
PVD – Physical Vapor Deposition
RF - Radio Frequency
DC – Direct Current
AC – Alternate Current
dcMS – Direct Current Magnetron Sputtering
HiPIMS – High Power Impulse Magnetron Sputtering
UBM – Unbalanced Magnetron
SZM – Structure Zone Model
DGLAD – Dynamic Glancing Angle
AISI – American Iron and Steel Institute
XRD – X-Ray Diffraction
GDOES – Glow Discharge Optical Emission Spectroscopy
SEM – Scanning Electron Microscopy
FEG – Field Emission Gun
EDS – Energy Dispersive Spectroscopy
FIB – Focused Ion Beam
TEM – Transmission Electron Microscopy
STEM – Scanning Electron Microscopy
AFM – Atom Force Microscopy
μ – Coefficient of friction
FCC – Face centered cube
GLAD – Glancing Angle Deposition
IPF – Inverse Pole Figure
SAGB – Small Angle Grain Boundary
BSE – Back-Scattered Electrons
Er – Reduced Elastic Modulus
GPa – Gigapascal
ASTM – American Society for Testing and Materials

TABLE OF CONTENT

1. INTRODUCTION

Energy generation and consumption have been some of the main quests in modern society within the last decades, since non-renewable resources have been used in a rate that will bring them to scarcity in the next century. Along with the consumption, the pollution generated using these resources is associated with climate change perspectives for the next decades.

One of the alternatives to mitigate these effects is to enhance efficient of energy consumption. A study estimates that up to 23% of the global energy generated is lost due to friction and wear (HOLMBERG; ERDEMIR, 2017). In this scenario, surface engineering plays a crucial role in designing components with improved tribological performance and enhance efficiency of fuel usage.

Among the several technologies for surface improvement, deposition of hard coatings found many applications due to its high versatility, mechanical performance, and corrosion resistance by uniting features of a metallic substrate with ceramic films (MATTOX, 2007). Physical Vapor Deposition (PVD) has been one of the main deposition routes applied industrially. It involves the evaporation of a source material, transport of this vapor to the substrate surface and further condensation of the film (BUNSHAH, 2001).

PVD techniques are classified accordingly to their vaporization methods. In sputtering, the vaporization is achieved by means of impinging the surface of a target made of the source material with projectiles (ions or electrons, for instance), causing the ejection of the target material (BUNSHAH, 2001; OHRING, 2013). Currently, some of the most important sputtering technologies use plasma of an inert gas as the source for projectiles (ions of the inert gas) as it provides higher deposition rates and allows for industrial processes with lower vacuum requirements (BUNSHAH, 2001). The sputtering process can be further improved using a magnetron positioned behind the target. This device encloses the plasma in the vicinities of the target surface, enhancing sputtering (LIN; WEI, 2018).

The target materials can suffer ionization as an effect of the sputtering process. Usually, these materials are metals that become a cation. If a negative bias polarization is delivered to the substrate surface the cations will be accelerated towards it, which enhances the energy of the arriving material, causing substrate heating and improving diffusion and densification of the growing film, affecting positively the mechanical

properties of the coating. This feature is explored by techniques that deliver high ionization of the sputtered material, such as High Power Impulse Magnetron Sputtering (HiPIMS). In this type of magnetron sputtering, short duration power peaks of high intensity are provided by a specific power supply to the sputtering system, favoring ionization (ANDERS, 2017).

Transition metal nitrides are among the most important coating materials in industry, being CrN and Cr-Al-N some of the most prominent choices for hard coatings, since they present high oxidation resistance in high temperatures when compared to other nitrides, along with appreciable hardness and wear performance (SUE; CHANG, 1995; SÁNCHEZ-LÓPEZ et al., 2005).

When producing coatings, different architectures for growth can be selected. For tribological applications the multilayers and, particularly, the superlattices are some of the most relevant by reason of achieving conditions of superhardness along with high toughness due to the systematical chemical modulation of thin layers (STUEBER et al., 2009). Recently, a novel architecture has been proposed where a multilayer-like structure is generated in monolayer coatings by the continuous oscillatory motion of the substrate surface during deposition. An improvement on hardness of CrN magnetron sputtered films has been suggested as an effect of this architecture (GUIMARAES et al., 2018).

The understanding of the phenomena behind the obtaining of such multilayer-like nanostructures and its potential impacts on the properties of the hard coatings for tribological applications are the subject of study of this project, along with specific aspects of the HiPIMS and dcMS deposition techniques and its influence on the coating's performance.

This thesis is structured in the following manner: First, a Scientific Background section, that is supposed to be sufficient for the correct contextualization of the reader for the further sections of the text. The Aims of the project are then presented in more details and Experimental Procedures regarding Experimental Planning, Coatings Production and Characterization are detailed. The Results and Discussions consist of three chapters, being the first two presented integrally as previously published in research periodicals. The last chapter presents results that have not been published yet but are fundamental for the achievement of the aims of this thesis. Next, general conclusions are enlisted and suggestion for future topics of research are introduced. The reproduction of all papers in this thesis, being those integral or in parts, are in

accordance with the copyright policies of the publishers Springer Nature and Materials MDPI, being one of the authors of the papers also the author of this thesis.

2. SCIENTIFIC BACKGROUND

2.1. SURFACE ENGINEERING

Surface engineering can be defined as the designing and improving of a determined set of properties in the superficial region of a material in comparison to its subsurface portion. These properties may be related to aesthetic demands, frictional, optical, electronic, magnetic, or thermal properties and corrosion, wear and abrasive resistance, along with others. The possibility of modification of these properties have guaranteed applications to surface engineering in a wide variety of fields, such as chemical and petrochemical, aerospace, electronics, automotive, power, machining tools, biomedical and textile industry, among others (MARTIN, 2005; HUTCHINGS; SHIPWAY, 2017).

The techniques for surface modification can be classified in three different categories (HUTCHINGS; SHIPWAY, 2017):

- Processes that do not change the chemical composition of the surface (e.g., micromachining, shot peening, surface melting).
- Processes that change the chemical composition of the surface but do not add a new layer on top of the substrate. This change can be caused by the formation of a new phase or a solid solution within the substrate (e.g., carburizing, nitriding, boriding).
- Processes that cause the growth of a new layer on top of the surface of the substrate (e.g., plasma coating, anodizing, thermal spraying).

A combination of two or more types of techniques is also usual in multi-step processes such as gas nitriding prior to coating deposition on a metallic substrate (MATTOX, 2007).

In the last decades, developments in electronics and process control, vacuum technology and plasma science have significantly improved the quality and productivity of coatings (i.e. the third category aforementioned), placing them as one of the main solutions for surface engineering problems and stretching even further their range of application (KELLY; ARNELL, 2000; MARTIN, 2005; HOLMBERG, 2009).

There are several techniques available for the manufacturing of coatings and thin films. The following section describes in detail some of them, with a special focus on vapor phase depositions and sputtering processes.

2.1.1. Deposition techniques

Coating technologies can be classified according to the state of the precursor materials that will be used to coat the substrate. It can be in solution state (e.g., sol-gel techniques), molten or semi-molten state (e.g., thermal spraying) or gaseous or vapor state (e.g., chemical vapor deposition) (CHATEAUMINOIS, 2000; HOLMBERG, 2009).

Vapor state processes have been the standard route for film deposition in the fabrication of several products such as machining tools and engine parts for a long time. There are two main techniques that use vapors as deposition materials: Chemical Vapor Deposition (CVD) and Physical Vapor Deposition (PVD). The first can be described as a process in which a thin film is formed on top of the substrate by a reaction between two or more gaseous precursors that occur in the reactor atmosphere and on the substrate (JONES, ANTHONY C., 2009). PVD, on the other hand, can be defined as a coating process where solid or liquid precursors are vaporized by a physical process and condensed on the surface of the substrate (MATTOX, 2007; OHRING, 2013).

When compared, both techniques can yield high quality coatings with important industrial role (RUPPI, 2005; KASMI, EL et al., 2016; PAIVA et al., 2017; ZHANG et al., 2018). However, there are technological differences that may determine the choice of one over another (BUNSHAH, 2001). PVD techniques usually require inert gases, such as Ar, Xe or N_2, while CVD depositions often require gas precursors that are environment and/or health harmful ($TiCl_4$, as an example) (HOLMBERG, 2009). Moreover, high working temperatures (750°C – 1150°C) in comparison with PVD processes (350°C – 600°C) are a significant drawback of CVD technology in terms of economic costs for industry (BUNSHAH, 2001; BAPTISTA et al., 2018). Also, materials sensitive to higher temperatures, such as polymers, cannot be coated via traditional CVD routes.

Further concerning energy input on fabrication of thin films, PVD have higher efficiency in power consumption than CVD. In a study, Gassner *et al* (GASSNER et al., 2016) have stated that more than 40% of the energy consumed in a CVD typical process belongs to the heating ramp from room temperature to working conditions, while in PVD depositions the most energy demanding stage is the coating step itself,

with roughly three quarters of the global energy consumption. These advantages justify the role of PVD as one of the main processes for coatings deposition nowadays.

The growth of a film by PVD can be segmented in three steps. First, the precursor material must somehow be vaporized, then it is transported through a vacuum, gas or plasma atmosphere, and finally condenses on the surface of the substrate on the form of a film through mechanisms of nucleation and growth. The vaporization step is fundamental for the final properties of the coating and can be achieved by different routes, being evaporation and sputtering the two most important types (MATTOX, 2007; HOLMBERG, 2009).

In evaporation, a source of heat is used to enhance energy of the precursor's atoms and vaporize them. Different types of heat sources, such as arc, induction, electron beam and resistances can be chosen to promote vaporization, depending on the needs of deposition rate and properties of the resulting films. Evaporation processes are also known as "Vacuum Evaporation" because they are usually carried out in conditions of high vacuum, promoting almost a collision-less transport of the vaporized material to the substrate surface (BUNSHAH, 2001; MATTOX, 2007).

In sputtering, the collision between a projectile and the surface of a solid or liquid precursor (hereafter called target) promotes its vaporization by ejection in different possible species (atoms, ions or molecules) depending on the magnitude of the collision and on the nature of the target. Typically, an inert partially ionized gas (plasma) is used as projectile (BUNSHAH, 2001; GREENE, 2017). For this reason, working pressures are some orders of magnitude higher than in evaporation processes. Sputtering depositions will be further described in the next sections as it is the type of vaporization used in this project. Figure 1 lists the main PVD techniques currently available.

Figure 1 - Classification of current PVD techniques. Names in bold are the technologies of most interest for this study.

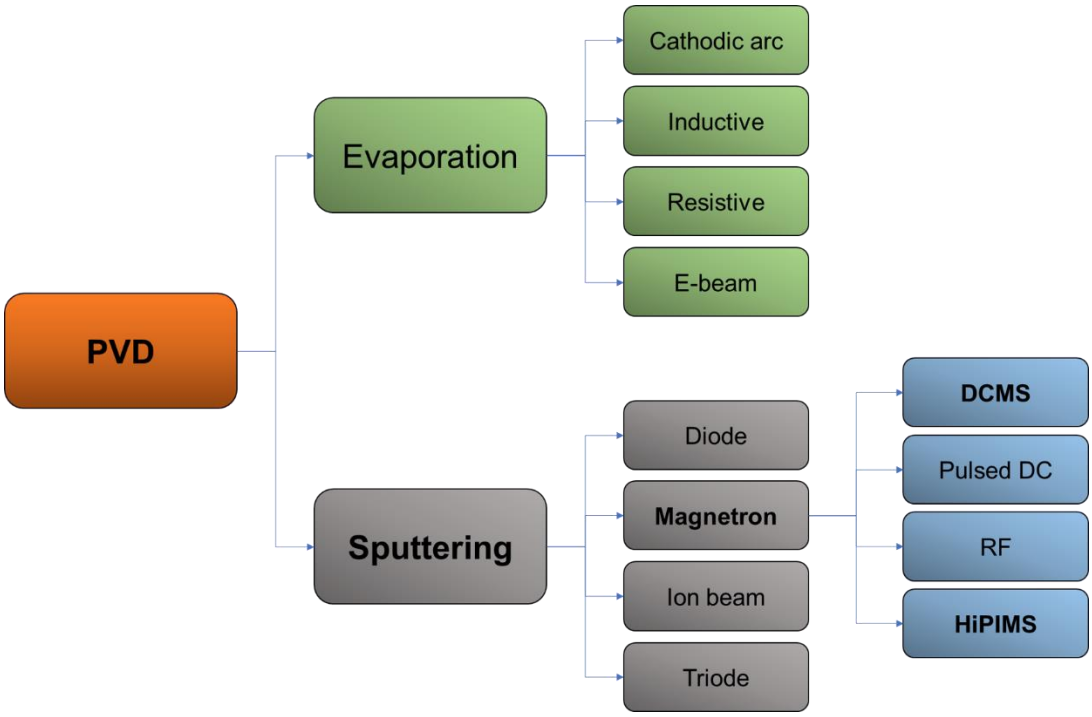

Source: The author.

2.1.1.1. SPUTTERING

As above-mentioned, the driving force behind the sputtering depositions is the momentum transfer by kinetic collisions between the projectile species and the target surface. One can determine a “sputter yield” as a mean of quantification of the sputtering process. Sputter yield consists of the number of atoms ejected from the target per incident ion. It is of great interest in terms of productivity, since it strongly affects deposition rate of the coatings and is influenced by the energy of the impinging ions, type of target material, crystal structure of the surface of the target and incident angle of the ions (WASA et al., 1992). Ion bombardment involves other phenomena than just ejection of species, such as cascade collisions, secondary electrons emission and thermal heating. Therefore, computational tools (e.g., Monte Carlo simulations, molecular dynamics simulations) are often used to describe these processes (WASA et al., 1992; ONO et al., 2008).

The projectiles in the sputtering process are often ions that are accelerated against the target charged with a negative potential (cathode). These ions can be provided by an ion gun (in Ion Beam depositions) or by a plasma (MATTOX, 2007).

A plasma can be described as gas in high temperature that is partially ionized by the presence of an electric field. Although the fluid is composed of charged and neutral particles, its global charge is quasineutral (CHEN, 2016). One of the main differences between a plasma and a gas is the presence of a collective behavior, i.e. the movement of charged particles inside a plasma generates concentrations of positive and negative particles, creating electromagnetic fields and currents, which may affect movement of other particles in distance (CHEN, 2016). Usually, inert gases are chosen to form plasma for sputtering, being Ar the most common due to its relative high mass, that can improve sputter yield, and affordable cost.

The simplest experimental assembly that uses plasma for sputtering is that of the planar diode (BUNSHAH, 2001). Figure 2 is a schematic representation of a conventional planar diode.

Figure 2 - A planar diode sputtering process representation.

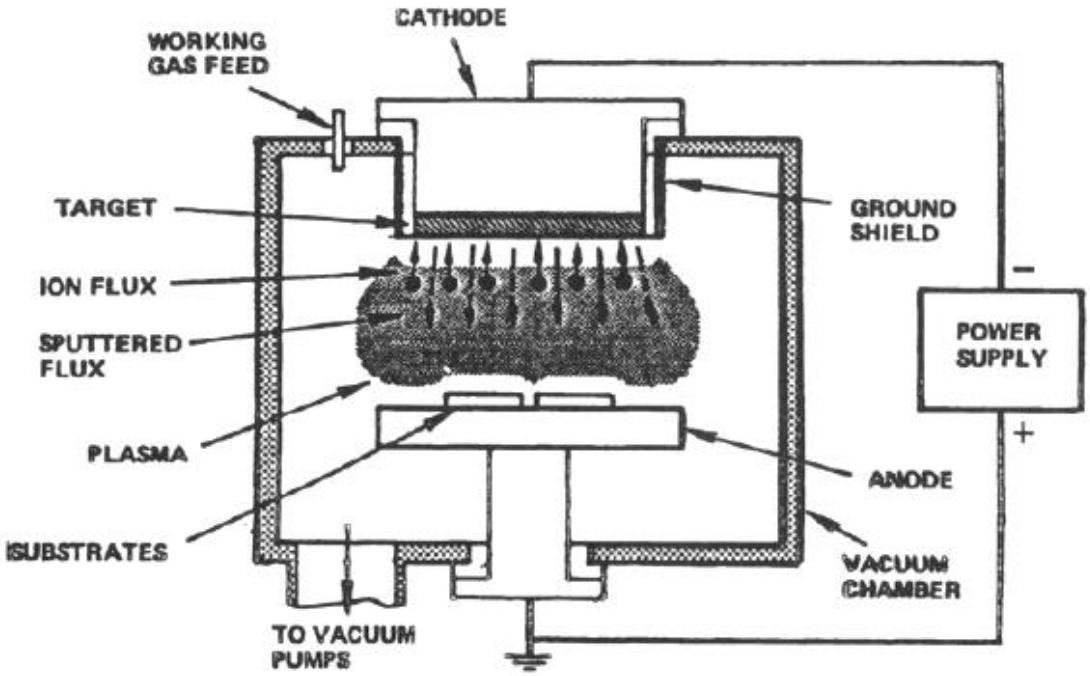

Source: (BUNSHAH, 2001).

Although the planar diode technique allows for the growth of uniform coatings, the low deposition rate, substrate heating and low ionization are big drawbacks in practical applications, leaving it restrict to few uses in modern sputtering technology (BUNSHAH, 2001; BRÄUER, 2014).

One of the solutions to improve productivity and quality of sputtering depositions is the introduction of a magnetic field in the proximities of the cathode to intensify the ionization of the gas. This creates a region of high-density plasma closed to the target surface, that in turns promotes sputtering efficiency (KELLY; ARNELL, 2000; MATTOX, 2007; HOLMBERG, 2009). This type of deposition is called magnetron sputtering referring to the presence of the magnetron, a device formed by the assembly of several permanent magnets and responsible for the generation of the magnetic field. Figure 3 presents the schematics of a magnetron sputtering process.

Figure 3 - Schematic draw of a magnetron sputtering process.

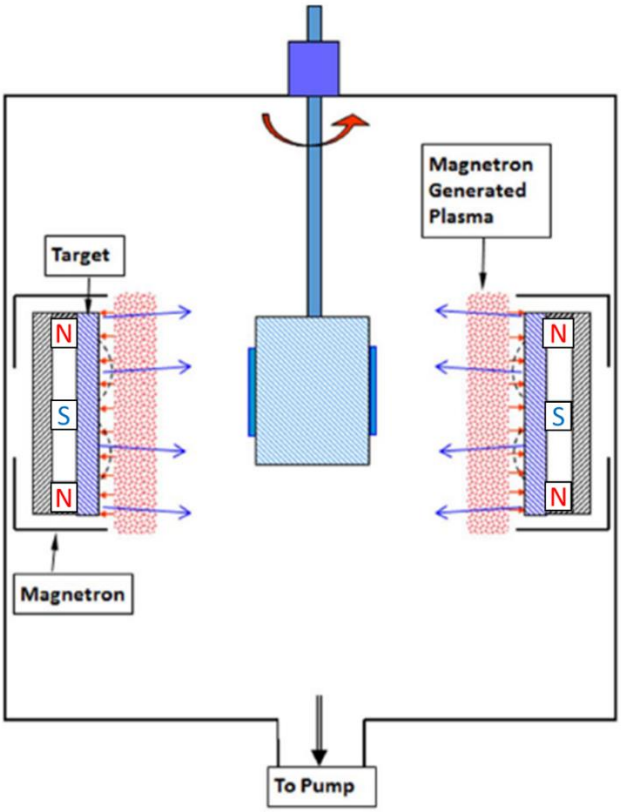

Source: Adapted from (LIN; WEI, 2018).

The inhomogeneous magnetic field generated by the magnetron imprisons the secondary electrons naturally emitted in the sputtering process in a helicoidal ring

trajectory along the target surface, according to the Lorentz force. This closed-circuit path enhances the probabilities of collisions between the electrons and gas atoms, causing the ionization of the later, contributing to the densification of the plasma closed to the target surface. The sputtering rate along the electrons path is 10 to 20 times larger than in other regions. This causes the erosion of the target in the so called “racetrack” shape (WASA et al., 1992; BRÄUER, 2014). Figure 4 shows the conventional helicoidal path of the electrons and the eroded surface of the target. The improvement in deposition rate caused by the adding of the magnetron device allows sputtering in conditions of lower pressure when compared to the planar diode sputtering processes, which causes less collision and loss of energy in the path of the sputtered material. (KELLY; ARNELL, 2000; BRÄUER, 2014).

Figure 4 – Path of electrons along the target surface of a planar magnetron.

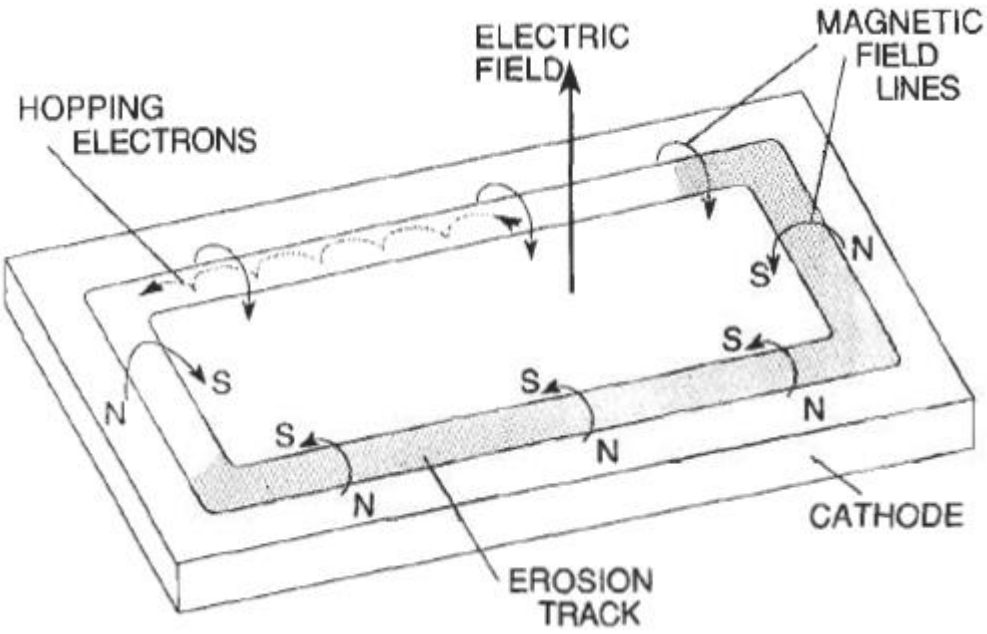

Source: (OHRING, 2013).

A major advance in developing of magnetron sputtering was presented in 1986 by Savvides and Window with the introduction of the concept of Unbalanced Magnetron Sputtering (UBM) (SAVVIDES; WINDOW, 1986; WINDOW; SAVVIDES, 1986). While in conventional magnetron sputtering the set of permanent magnets is designed to keep the magnetic fields, and therefore the plasma, closed to the cathode surface, in UBM there is an assembly of magnets such that not all field lines generated

by one pole pass thought the other, extending the magnetic field beyond the cathode surface to the substrate. A representation of both, balanced and unbalanced magnetrons is provided in Figure 5. The field lines can be either generated by the central magnets and partially escape the outer poles or can be generated by the outer magnets and partially escape the central pole (WINDOW; SAVVIDES, 1986; HOLMBERG, KENNETH, 2009).

Figure 5 - Representation of balanced and unbalanced magnetron sputtering. The extended plasma region is noticeable in the UBM.

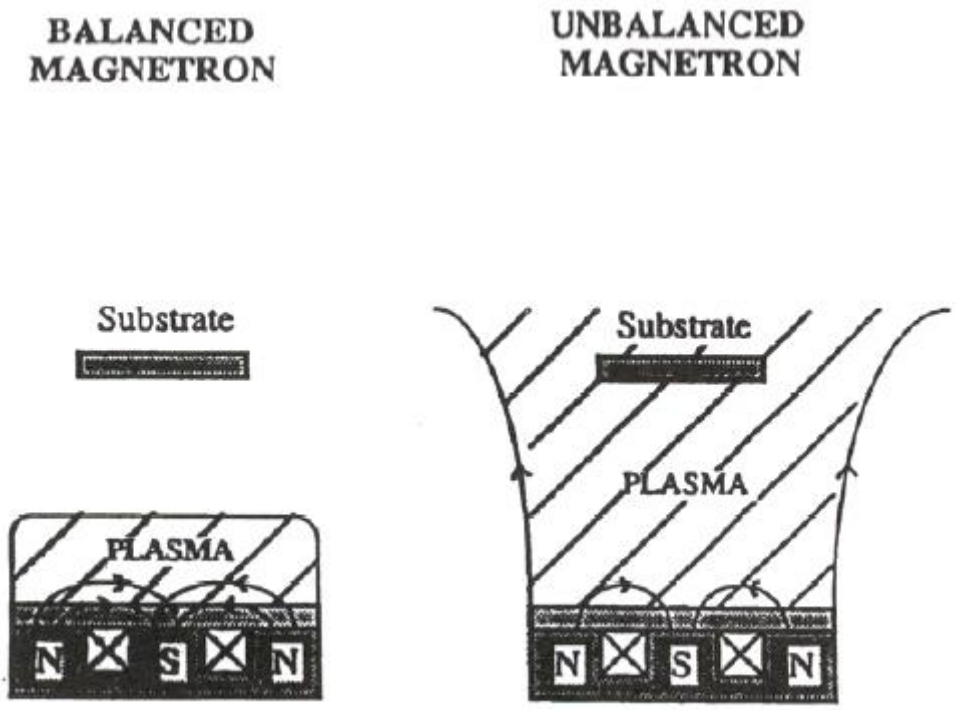

Source: (BUNSHAH, 2001).

In applications where surface damage of the coatings cannot be tolerated, e.g. magnetic devices and optical films, balanced magnetron is often chosen. However, for hard coatings, where well-adhered and dense films are needed, the ion bombardment of the growing film generated by the extended plasma has been proved to be beneficial, since it enhances mobility of adatoms, causes re-sputtering and promotes nucleation and compressive residual stress development. In those cases (coating of cutting tools, for instance), UBM is usually chosen (BUNSHAH, 2001; HOLMBERG, KENNETH, 2009).

2.1.1.2. REACTIVE SPUTTERING

A reactive gas can also be injected in the reactor along with the working gas if the intention is to form a compound film. The reactive gas may combine with the sputtered species during film growth in what is called reactive sputtering. This process allows for the production of films of nitrides, oxides, carbides, carbonitrides, etc, by the introduction of oxygen, nitrogen, and methane in the sputtering chamber, along with the working gas (Ar, usually) (BERG; NYBERG, 2005). An industrially important example of reactive sputtering is the coating of cutting tools using metallic high purity Ti targets and N_2 as reactive gases to form TiN films.

However, the formation of the compound layer is seldom confined to the substrate surface only and usually happens all over the reaction chamber, even on the target itself. This gives rise to the growth of a compound film, usually non-conductive, on the cathode surface and a significant drop in deposition rate is observed, in what is called Target Poisoning (BERG et al., 2008). If the growth of this insulator layer does not cover the whole target surface, the regions free of compound film will suffer from power concentration of several W/cm^2 leading to ejection of macroparticles and even local melting. On the other hand, if the surface of the cathode is completely coated with non-conductive material, the plasma cannot be sustained, since no current passes through the cathode and the process stops (this phenomenon is named Disappearing Anode (BERG et al., 2008)). In face of these major issues of reactive sputtering the use of pulsed discharges in reactive depositions is recommended since it reduces arcing. Also, target cleaning between batches is also necessary to remove the compound layer.

2.1.1.3. DCMS

Direct Current Magnetron Sputtering is a type of deposition technique in which a non-variable tension is applied between a cathode (target) and anode (usually the walls of the chamber) and a direct current is provided by a power supply. It finds applications in several tribological solutions due to its simplicity, with few parameters to control, and yet appreciable quality of the resulting films (CHAVDA et al., 2016).

Working pressures in the range of 1-10 mtorr and voltages of 300-700 V are often used in DCMS (OHRING, 2013). A negative bias potential can be applied to the substrate to accelerate positive ions sputtered from the cathode and enhance film bombardment.

The use of direct current is known to promote few ionizations during sputtering. This directly influences the coatings properties, such as hardness and adhesion, since neutrals cannot be accelerated to bombard the substrate and the growing film (GRECZYNSKI, GRZEGORZ et al., 2010; SCHMIDT et al., 2016; GUIMARAES et al., 2018). Another limitation of the DC process is the deposition with non-conductive compound targets since the direct current can create retained charges on the surface of poorly conductive targets. In order to overcome these issues, techniques such as alternate current depositions (AC), pulsed-DCMS and HIPIMS were developed (KELLY; ARNELL, 2000).

2.1.1.4. HIPIMS

In 1999 Kouznetzov and colleagues introduced a pulsed deposition technique with very high target power densities (KOUZNETSOV et al., 1999). A new development in power supplies allowed for power densities of 2800 W/cm^2 (in comparison, DCMS used power densities of up to 300 W/cm^2 back in the day). This type of deposition was later named as High Power Impulse Magnetron Sputtering (HIPIMS or HPPMS).

The high power densities achieved in HIPIMS promote an expressive degree of ionization in the sputtered materials (up to 90%) which can enhance deposition energy and produce denser and harder coatings (MATTOX, 2007; HECIMOVIC; GUDMUNDSSON, 2017) (see more on Section 2.2). Since the high intensity power peaks are applied in short durations and the mean power over time is similar to those of DC processes, there is no risk of cathode overheating and damaging, which is a major concern when power is enhanced in DCMS.

A HIPIMS pulse can be sub-divided into two portions: t_{on}, when power is being effectively applied and t_{off}, when no actual power is delivered. A typical HIPIMS pulse with power, current and potential discharge is portrayed in Figure 6.

Figure 6 Conventional triangular shaped HiPIMS pulse.

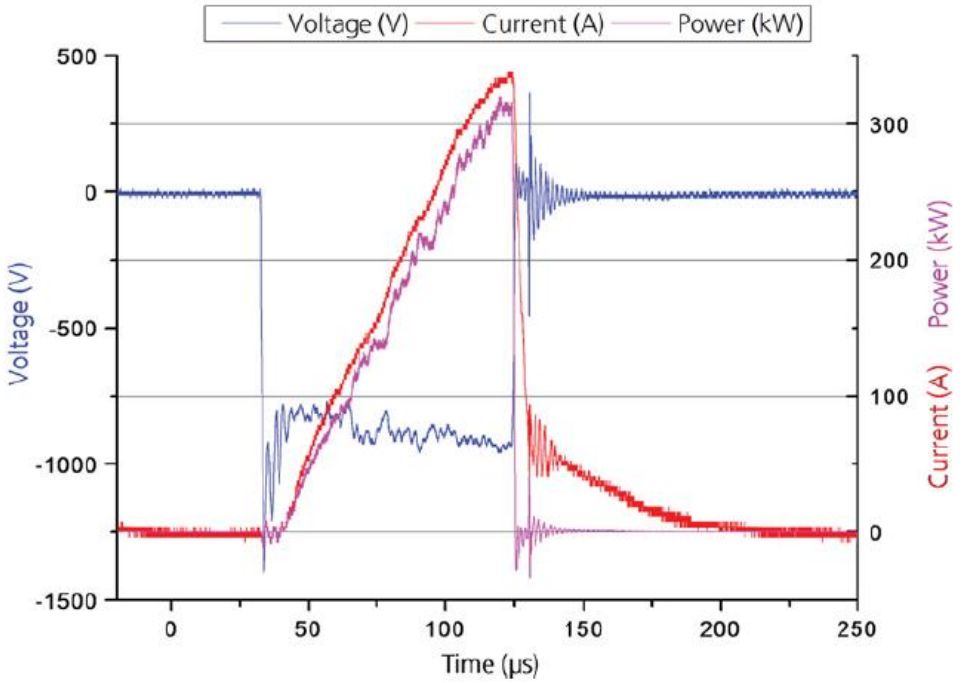

Source: (BRÄUER, 2014).

From the pulse curve, one can observe that a discharge of several hundred Volts and Amperes is followed by a t_{off} period of no power. The duty cycle is the fraction of the pulse dedicated to deliver power and can be calculated as in Equation 1:

$$duty\ cicle = \frac{t_{on}}{(t_{on}+t_{off})} \quad (1)$$

Usually, duty cycles up to 10% are applied in HIPIMS depositions. Another important process variable is pulse frequency, which can be described as the inverse of the pulse period, or as seen in Equation 2:

$$f = \frac{1}{(t_{on}+t_{off})} \quad (2)$$

In conventional HIPIMS depositions, frequency varies between hundreds to few thousand Hz. Due to the large number of process variables (e.g. duty cycle, pulse frequency, pulse shape), HIPIMS requires more study for its implementation than direct current processes.

The most important disadvantage of the HIPIMS technique is its lower deposition rate in comparison to DC and even other pulsed magnetron depositions (BRÄUER, 2014; ANDERS, 2017). One of the main reasons for that is the small duty cycle chosen to provide very intense peaks that have the side effect of minimize the time that the material is sputtered and that the coating can grow (BRÄUER, 2014). In

addition to that, the high ionization degree causes a high amount of the positive ions of the sputtered material to be back attracted to the negatively charged cathode, diminishing the material flux to the substrate (ANDERS, 2010a; BOBZIN, K. et al., 2017). Also, the increase of bombardment of the growing film, which in turns is extremely positive to properties of the films, as aforementioned, causes densification of the coating and even self-sputtering, that can contribute to lower apparent deposition rate (ANDERS, 2010a).

Along with the complexity of the multiple variables involved in the HiPIMS technology, the lower process efficiency is one of the responsible for resistance in wider implementation of HIPIMS in industrial process, although it is already used for several application that requires well adhered, dense and hard coatings (ANDERS, 2010a; BAPTISTA et al., 2018).

2.1.2. Structure Zone Models and influences of deposition parameters.

The several deposition techniques presented before enclosing each a large number of process variables that influence directly on the nucleation and growth mechanisms, having a huge impact in morphology and properties of the coatings. Therefore, it is paramount to comprehend the role of each deposition parameter in order to tune it to produce the desirable films.

An initial approach to simplify the exhaustive list of parameters involved in a PVD deposition in few variables and understand their part in coating's production was taken by Movchan and Demichishin (MOVCHAN; DEMICHISHIN, 1969). Their work brought for the first time the concept of a Structure Zone Model (SZM), a systematic categorization of the growth behavior of coatings as a function of the homologous temperature T_h (Equation (3)) based on experimental observation of cross section of films.

$$T_{h=}\frac{T_s}{T_m} \quad (3)$$

Where T_s is the substrate temperature and T_m is the melting point of the substrate material.

These models are a simplification that act as a guideline to understand the dynamics of film growth (THORNTON, 1988). The model introduced by Movchan and Demichishin can be seen in Figure 7.

Figure 7 - First Structure Zone Model, as proposed by Movchan and Demichishin.

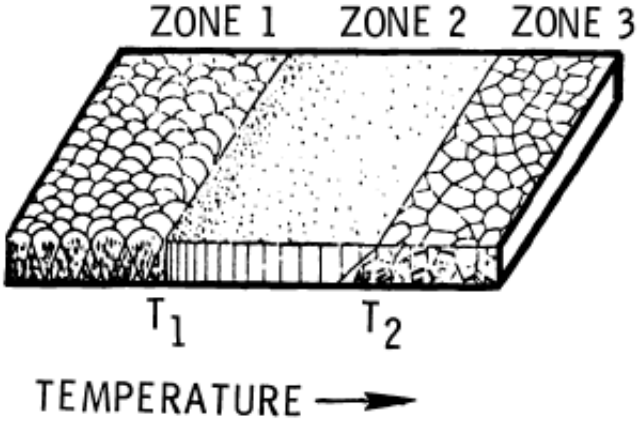

Source: (MOVCHAN; DEMICHISHIN, 1969).

From the model proposed in 1969, 3 different zones can be identified. Zone 1 corresponds to a process of low homologous temperature ($T_h < 0.3$), where adsorbed atoms at the surface of the substrate do not have enough energy to migrate to other regions and keep their arrival position. This creates a film with fibrous growth, voids, pores and defects between grains and domed shaped surface (MOVCHAN; DEMICHISHIN, 1969; ANDERS, 2010b).

In Zone 2, the homologous temperature is higher, and the morphology achieved is a distribution of fine columnar grains with few voids between columns. This behavior is present in conditions of $0.3<T_h<0.5$, where the adsorbed atoms have energy enough to diffuse into regions to minimize surface or lattice strain energy. The grain size grows with increase of T_h and the top surface has a faceted morphology (MOVCHAN; DEMICHISHIN, 1969; THORNTON, 1988).

Zone 3 is known to present a very dense morphology, with equiaxial grains and atoms having no memory of their initial position in the condensing step. In this case, homologous temperature is so high ($T_h>0.5$) that bulk diffusion is more relevant than surface diffusion and recrystallization will occur (MOVCHAN; DEMICHISHIN, 1969; THORNTON, 1988).

An intermediate Zone between Zone 1 and Zone 2 ($0.2<T_h<0.4$), known as Transition Zone, or Zone T, was proposed by Barna and Adamik (BARNA, P. B.; ADAMIK, 1998). The Zone T presents grains in conical shapes due to competitive

growth caused by expressive adatom mobility but low grain boundary diffusion (BARNA, P. B.; ADAMIK, 1998; ANDERS, 2010b). Figure 8 is a schematization of this SZM.

Figure 8 - SZM as proposed by Barna and Adamik.

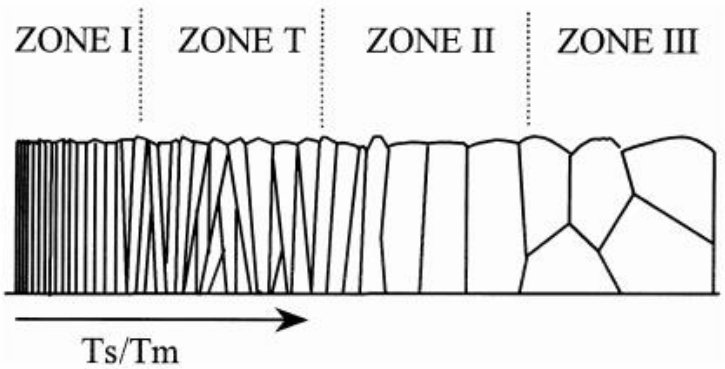

Source: (BARNA, P. B.; ADAMIK, 1998).

As previously stated, the energy of the arriving particles is a determinant factor on the mobility and diffusion of the adsorbed atoms during the film growth process and is highly dependent on pressure, since the higher the pressure is, the smaller the average distance between two successive collisions of a traveling particle within a gas (i.e., the mean free path). These collisions are responsible for causing loss of energy from the sputtering process to the arrival of the particles on the substrate surface and should be taken in account in the prediction of the film morphology (ANDERS, 2010b). In 1974, Thornton proposed a new SZM with an additional axis corresponding to pressure (THORNTON, 1974).

In 2010, Anders introduced a more universal SZM by describing the morphology zones in terms of intrinsic growth parameters, instead of process related ones (such as temperature and pressure). His model was produced by taking in account one axis related to a generic temperature T*, that considers the homologous temperature T_h and the heating effect generated by the energy of the arriving particles, and an axis related to the Kinect energy of the particles E*. This last axis considers the pressure effect, but also the contribution of ion acceleration, when present. The third axis was associated with the film net thickness in order to clear effects of densification and re-sputtering (ANDERS, 2010b). The resulting SZM is presented in Figure 9.

Figure 9- General SZM as proposed by Anders.

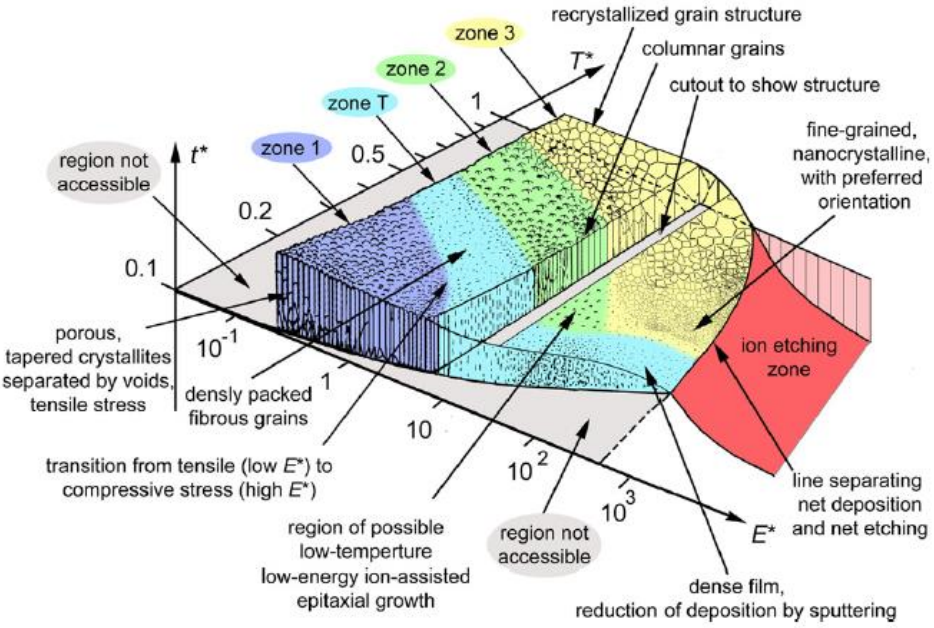

Source: (ANDERS, 2010b).

The model from Figure 9 describes a densification of the film with evolution from porous and fibrous crystallites to fine nanocrystallites as E* and mainly T* increases, which is also accompanied by an expressive thickness reduction until the point where ion etching (negative thickness) is achieved. Denser and finer films will almost always present superior tribological and mechanical properties. Therefore, tuning E* is of foremost importance to achieve high performance on coatings (ANDERS, 2010b).

Applying a negative tension bias to the substrate can enhance E* by accelerating the positive ions from the target formed in the sputtering process towards the substrate surface. Several studies correlate increase in negative substrate bias with grain refinement, compressive stress evolution and mechanical properties improvement (VAZ et al., 2001; TUNG et al., 2009; MA et al., 2017; GUIMARAES et al., 2018).

Another technical solution to enhance E* is to increase the number of ions in the promoted in the sputtering. As stated in section 2.1.1.1 the HiPIMS process is known to generate higher ion/neutral ratios then other magnetrons sputtering techniques due to the intense power peaks generated by the power supply. If the average power is set to be constant, pulses with shorter duration will deliver higher peak power values, favoring ionization of the sputtered material. This can be achieved by lower pulse frequencies and shorter duty cycles (Equations 1 and 2). Literature

reports enhancements in mechanical properties and compressive residual stresses followed by reduction in deposition rate when shorter pulse duration is used, as described in Figure 9 with increase of E* (WEST et al., 2009; HSIAO et al., 2013; BOBZIN, K. et al., 2017).

2.2. NITRIDE COATINGS

Ceramic films have been widely applied as coating for metallic substrates in conjugated systems, in order to improve their superficial tribological, optical, electrical, thermal and anticorrosive properties. In wear and tribological applications, transition metal nitrides are among the most important choices due to their high hardness and chemical stability. Examples of such coatings are TiN, NbN, CrN, TaN, VN.

2.2.1. CrN

Chromium nitride coatings have been presented as a substitute with adequate hardness and wear resistance for TiN in applications that demand high chemical stability at high temperatures (up to 650°C) (SUE; CHANG, 1995). CrN has a cubic NaCl B1 type crystal cell with N occupying the octahedral interstices and with a lattice parameter of 0.4148 nm (EDDINE et al., 1977), as can be seen in Figure 10.

Figure 10 – Crystal structure of CrN.

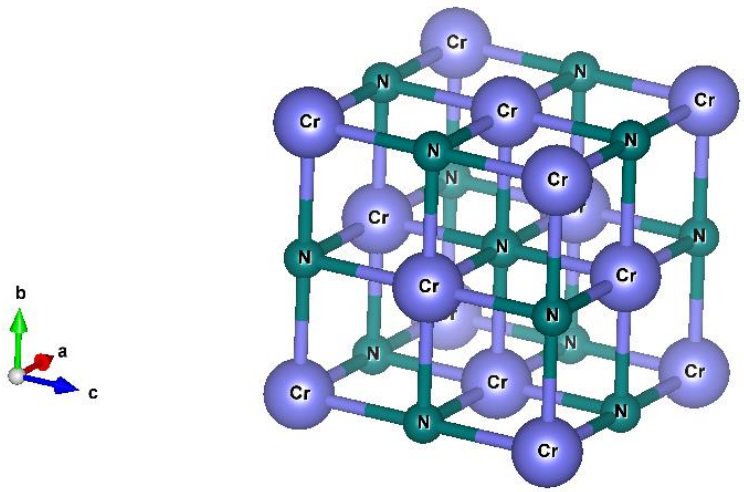

Source: The author.

If chromium nitride coatings are deposited in conditions of under-stoichiometric nitrogen a different phase of hexagonal crystalline structure may be formed (Cr_2N, with lattice parameters *a* and *c* of, 0.481103 and 0.447738 nm respectively) (CABANA et al., 2004). This structure is known for having distinguish tribological and chemical properties than CrN (MÜNZ et al., 2008).

Another advantage of CrN when compared to other transition metal nitrides is its lower level of residual stresses, which permits growth of thicker films with improved adhesion to the substrate (GÅHLIN et al., 1995; COLOMBO et al., 2013).

Wear protection in dies for forging process (NAVINŠEK et al., 1997), improvement in cutting tools (KONDO et al., 2004) and protection against seawater environment (LI et al., 2019) are examples of applications of CrN coatings.

CrN coatings were also reported recently as a material for construction of electrodes for supercapacitors (ARIF et al., 2018).

2.2.2. Cr-Al-N

The addition of Al to the CrN structure, forming a ternary nitride, can improve even further the corrosion and oxidation resistance of CrN, along with its hardness and wear performance (PULUGURTHA; BHAT, 2006; BOBZIN et al., 2007; GUIMARÃES et al., 2018). If Al is added to CrN in a proportion of up to 60 % at, there is no structure change from that presented in Figure 10, since the Al atoms partially occupy the positions of Cr in a substitutional solid solution. If the Al content is increased past 60 % at. up to 70 % at. there is a precipitation of hexagonal AlN as a second phase in fine disperse precipitates. Beyond 70% at. of Al there is only AlN and Cr starts to act as a substitutional element (KIMURA et al., 2003).

The increase in hardness and on wear resistance followed by the Al addition until 60 % at. is attributed to grain refinement of the CrN structure. Also, there is a mismatch in atomic radius between Cr and Al which causes deformations in the crystal lattice when the solid solution is formed. This can be confirmed by the measuring of residual stresses growth with increasing in Al content. When Al content reaches the point of structure change there is a decrease in hardness and wear resistance due to the formation of the much softer AlN (REITER et al., 2005). Figures 11 and 12 presents the dependence of hardness and residual stresses on Al content, respectively.

Figure 11 - Universal hardness (HU) and wear rate as a function of atomic Al content for Cr-Al-N coatings.

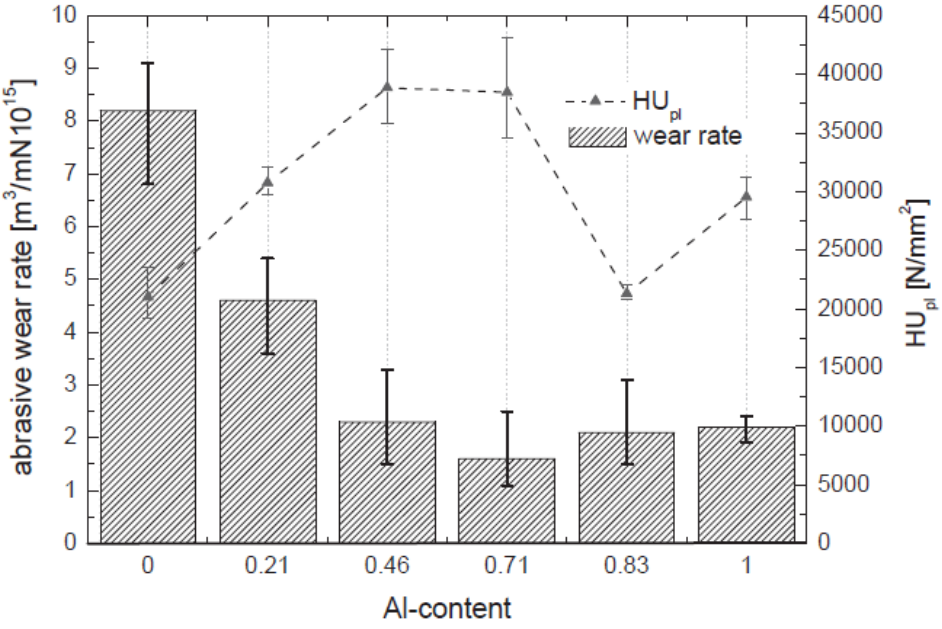

Source: (REITER et al., 2005).

Figure 12 – Compressive residual stress as a function of Al content in Cr-Al-N coatings.

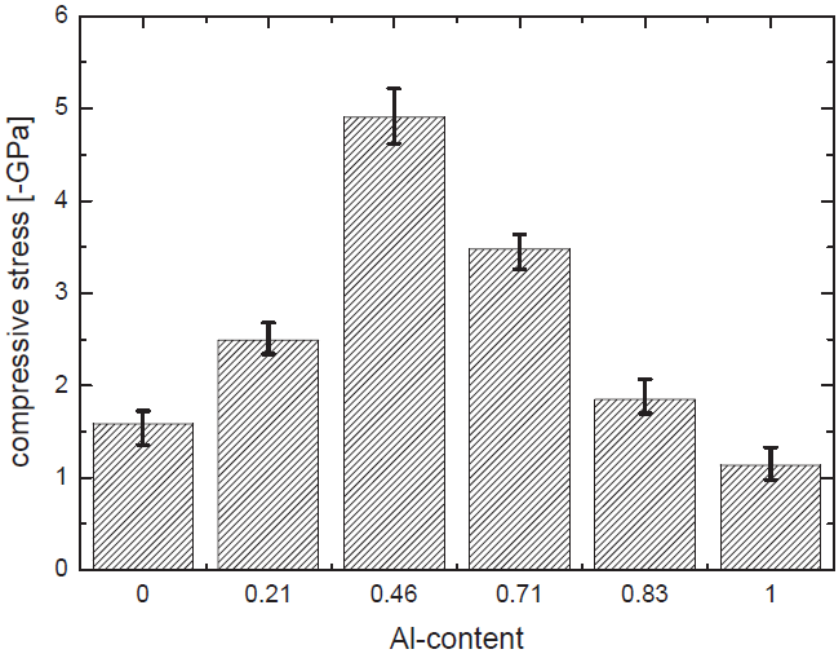

Source: (REITER et al., 2005).

The improved oxidation resistance of Cr-Al-N coatings at high temperatures can be explained by the formation of a nanocomposite structure, with regions richer in Al closed to grain boundaries. Those regions are oxidized preferentially, forming Al_2O_3 and other Cr-containing oxides, preventing oxygen to diffuse to the interior of the CrN grains with lower Al content and also obstructing grain growth (SÁNCHEZ-LÓPEZ et al., 2005; ROJAS et al., 2019).

These improvements in mechanical properties and chemical stability position Cr-Al-N ternary coatings as a candidate to expand the range of applications of CrN (KIM et al., 2012; LI et al., 2012; SÁNCHEZ-LÓPEZ et al., 2014).

2.2.3. Design of hard coatings

There is high versatility in the architecture and designs that can be achieved for hard coatings grown by PVD. Examples are single components, duplex, gradient coatings, composites and multilayers (HOLMBERG, 2009).

Multilayer architectures can be produced in a physical process by rotating the substrate surface in front of targets of different chemical compositions in order to form composition-modulated layers. This feature has been extensively researched in the last decades due to the possibility of preparing hard coatings with improved toughness and chemical resistance. If a multilayer coating is composed of layers of materials with same crystalline structures (two B1 structured nitrides, for example) and have a periodicity of few nanometers with expressive hardness improvement, they receive the designation of superlattices (HULTMAN, 2007).

Several nitride multilayer systems in these conditions have been reported as presenting conditions of superhardness (i.e., hardness > 40 GPa). The first achievement was described by Helmersson in 1987, with a monocrystalline TiN/VN coating presenting hardness close to 55 GPa for a superlattice with 5.2 nm of bilayer period (see Figure 13) (HELMERSSON et al., 1987). An investigation by Zeng in 1999 produced a coating with hardness of 48 GPa consisting of a TiN/NbN superlattice with bilayer period (λ) of 7.3 nm (ZENG, 1999). In 2009, Kim and colleagues have shown superlattices of CrN/CrAlN with hardness ranging from 37 to 46 GPa, low coefficient of friction (COF) and superior wear resistance for λ of 5.5 nm (KIM et al., 2009).

Figure 13 - Hardness dependency on bilayer period (λ) for a TiN/VN superlattice.

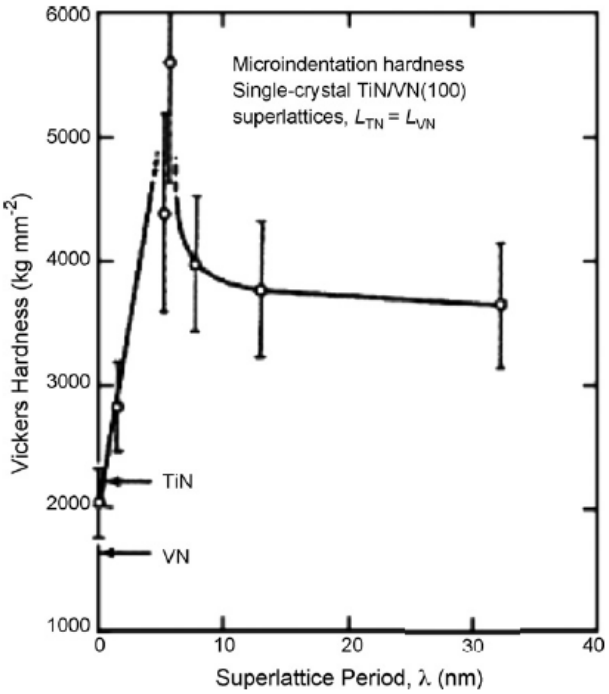

Source: (HELMERSSON et al., 1987).

The remarkable mechanical behavior improvement achieved by the superlattice structure in λ ranging from 5-10 nm are still subject of research. However, some mechanisms are accepted to explain this phenomenon. Hardness is an indirect measure of resistance to plastic deformation that is caused mainly by dislocation glide in crystalline solids, which is dependent on the shear modulus (G) and on preferential slipping systems of the material that is being deformed (HULTMAN, 2007). If a modulation of two material with distinct G is formed there will be obstructions when a dislocation glides from the material with inferior G to the one with superior G, since the deformation field generated on the vicinities of the line defect will find a stronger energy barrier to deform the lattice of the harder material (BARNETT; MADAN, 1998).

Sharp interfaces between layers also act as important dislocation obstacles and help explaining the superhard effect. However, in practical means, several times dissolution and smoother interfaces may be obtained during manufacturing of the coatings, creating interfaces with a finite extend (BARNETT; MADAN, 1998).

The modulation period has been proved to play a significant role in the formation of superlattices. If λ is too small (i.e., < than 2 nm) the layer thickness starts to get closer to the practical finite interface thickness and the effect of differences in G loses

importance, since dissolution causes layers to have similar G in the interface vicinity. On the other hand, if λ is too large (tenths of nm) the density of interfaces is too small and the dislocation glide within the layers becomes the most important mechanism of deformation (BARNETT; MADAN, 1998). This explains the behavior seen in Figure 13, where there is an optimal range of λ for superhardness effects between 5 and 10 nm, roughly.

Other mechanisms can also contribute to hardening in lesser extend such as punctual and linear defects and small grain boundaries as they also act as dislocation gliding barriers (HULTMAN, 2007).

2.2.4. Engineering of nanostructured coatings

New strategies for controlling properties of coatings based on engineering in the nanoscale by shaping the growth of films have been presented in the last decades. One of the most noticeable and commercially relevant is the Ballistic Deposition or Glancing Angle Deposition (GLAD). In this technique, the substrate is mounted in a geometry forming an angle different from 90° between its surface and the surface of the precursor target, as is standard for conventional sputtering. This angle is oblique and referred to as zenithal angle α. The deposition of materials in the off-normal geometry often produces coatings with columnar grains tilted in a β angle (where $\beta<\alpha$). Figure 14 is a representation of a coating grown under these conditions (LEONTYEV et al., 2008; BARRANCO; BORRAS; GONZALEZ-ELIPE, AGUSTIN R; et al., 2016).

Figure 14 – Scheme of a coating produced using GLAD.

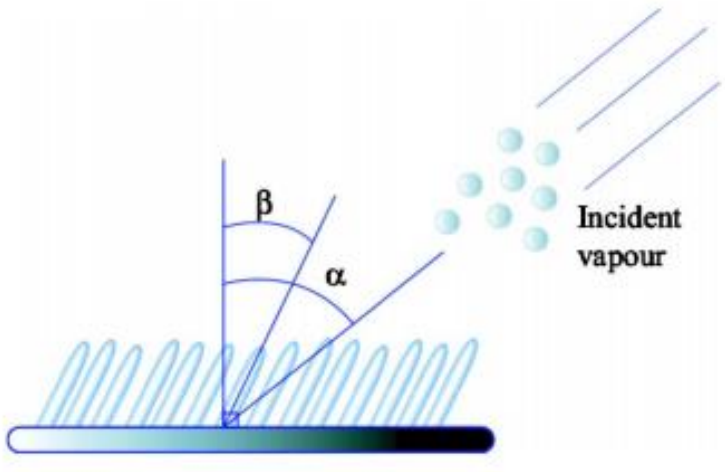

Source: Adapted from (LEONTYEV et al., 2008).

A particular feature of this type of deposition is the effect of shadowing. Since most deposition techniques like sputtering are line-of-sight dependent, the production of tilted structures promotes formation of pores and voids between grains. Usually, GLAD depositions are carried out in conditions of limited thermally activated mobility (i.e. low temperature or deposition energy), which reduces adatom mobility and preserves the tilted and porous nanostructure (BARRANCO; BORRAS; GONZALEZ-ELIPE, AGUSTIN R.; et al., 2016).

Different shapes of columnar grains can be obtained by associating the oblique deposition with a set of substrate motions. For instance, rotation of the substrate in the azimuthal axis or alternation between two different glancing angles can cause the formation of zigzag or helicoidal shaped columns as can be seen in Figure 15.

Figure 15 - Example of column shape design on the production of coatings. TiO_2 films were presented under a) stationary GLAD deposition b) alternation of glancing angle c) normal deposition.

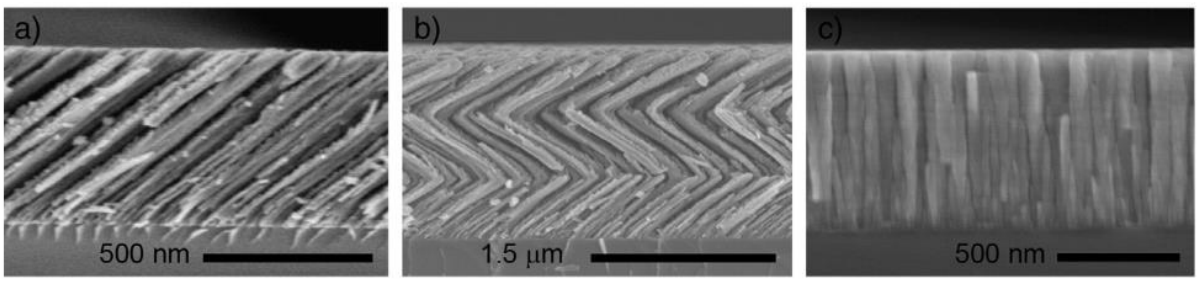

Source: (JIMÉNEZ-PIQUÉ et al., 2014).

Literature describes the films produced by GLAD as having interesting features such as high surface area, which is desired for applications such as chemical catalysis or coating of biological implants (ROBBIE; BRETT, 1997) and expressive anisotropy, that can be used to produce optical filters for angle and polarization (MANSOUR et al., 2010). Regarding mechanical properties, films with zig-zag shaped grains were described as having the behavior of a series of nano springs, being capable of bearing considerable loads without delamination or cracks (LINTYMER et al., 2006; JIMÉNEZ-PIQUÉ et al., 2014).

New advances in characterization techniques have allowed understanding of in-grains mechanisms present in sculptured films. For instance, nano diffraction measurements using focused synchrotron radiation indicated that the production of coatings with tilted grains by GLAD is associated with variations in residual stresses, texture and defects (KECKES et al., 2018). Figure 16 exemplifies the deposition of a TiN-SiO_x film in GLAD co-sputtering geometry with multilayers formed by variations in the α angle (-50° and 50°) and its impact on residual stresses.

Figure 16 - Example of the effect of GLAD deposition on residual stresses along the grains of the coating.

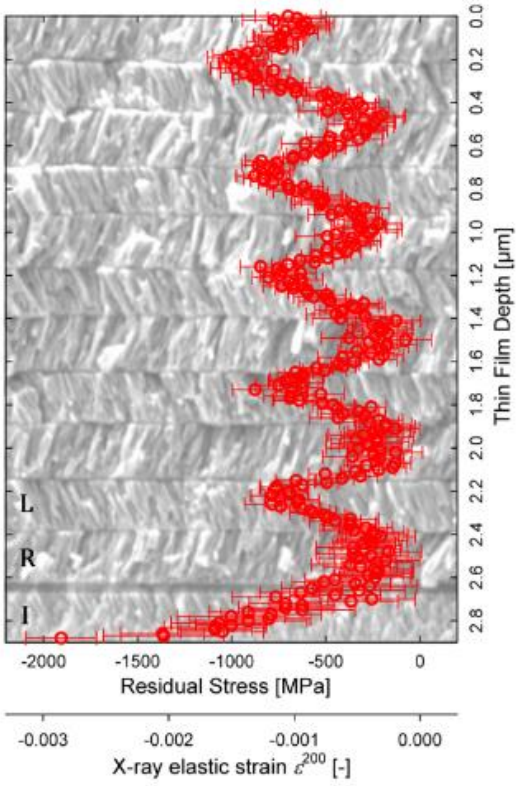

Source: (KECKES et al., 2018).

When compared to straight columnar grain coatings, films produced with tilted zig-zag sublayers present up to 200% enhancement in fracture toughness, which is due mainly to crack deflection at the sculpted grain boundaries (DANIEL et al., 2020).

Recently, a new concept for architecture of hard coatings taking in advantage the simplicity of single layer films with the potential to improve mechanical properties of multilayers and GLAD have been proposed (GUIMARAES et al., 2018; JIMENEZ et al., 2019). By continuously controlling and altering the incidence angle of the sputtered flux via substrate oscillatory motion a multilayer-like structure is built consisting of rows of a single material with small differences in growth directions. This results in changes in texture and hardness when compared to a stationary conventional monolayer but suffers less from shadowing effects of stationary GLAD architecture, resulting in less porous films. The understanding on the mechanisms of formation of those multilayer-like structures and its potential applications need further investigated and will be addressed in this study.

3. AIMS

The main aim of this project is to contribute to the understanding of how specific PVD deposition parameters can determine its selected microstructure and mechanical properties, with special interest in the tribological performance/response of coatings of the $Cr_{1-x}Al_xN$ system and how multilayer-like nanostructures can be designed to deliver coatings with improved mechanical properties.

This general aim was achieved by completing the following specific objectives:

- Fabrication of mono- and multilayer-like coatings of the $Cr_{1-x}Al_xN$ system with tailored microstructure on stainless steel substrates.
- Characterization of compositional profiles, morphology, phase formation, residual stresses, and crystallographic texture of the fabricated dcMS and HiPIMS films by spectroscopic, electron microscopy and diffraction techniques.
- Characterization of mechanical and tribological performance by instrumented nanohardness measurements and wear tests.
- Correlation of mechanical and tribological properties with distinctive features of the films fabricated under stationary and oscillatory conditions.

4. METHODOLOGY

4.1. EXPERIMENTAL PLANNING

The experimental planning of this study was designed to consist of three different steps. The first step was formed by the production and initial characterization of the coatings. The main criteria for choosing the optimized conditions were a combination of hardness and elastic modulus, since it may give an insight on the coating's tribological performance (LEYLAND; MATTHEWS, 2000). Also, deposition rate was considered since it is the most important economical aspect for the implementation of the coating in industrial environment. This first step required a recursive approach.

Second step consisted in the advanced characterization of the coatings using state of the art techniques of atomic force and electron microscopy and spectroscopy analysis to understand the effects of the deposition parameters in the atomic level and to properly link it with the enhancements in mechanical performance measured in step 1.

Finally, step 3 refers to tribological characterization of the optimized coatings selected in steps 1 and 2, making use of wear tests at room temperature to investigate the film's performances.

A schematic of the workflow of the three experimental steps is shown in Figure 17.

Figure 17 - Schematic of the experimental workflow for this project.

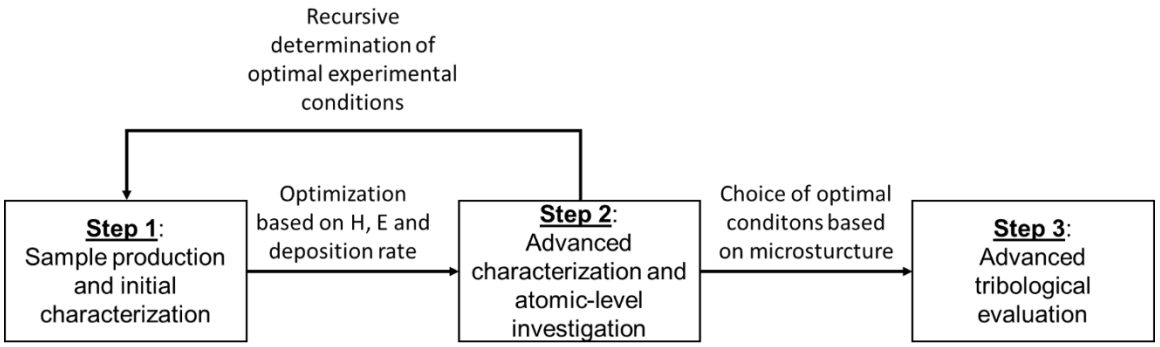

Source: The author.

The deposition parameters that were investigated in this project are divided in the following manner:

- HiPIMS and dcMS technology and its influence on coating's performance. HiPIMS pulse frequency [200, 300, 400, 500] Hz;
- Role of Al content [0, 50 and 70 at %] of the precursor target in the reactive sputtering of the nanostructured coatings;
- Production of multilayer-like nanostructures: Period of oscillation [0, 12, 30, 120] s; range of oscillation [0, 5, 10, 15, 20] degrees.

4.2. COATINGS DEPOSITION

4.2.1. Substrate preparation

The substrate chosen for the samples were 30 x 10 mm discs of AISI 304 stainless steel due to its versatility in a wide range of engineering applications, such as, engine parts, food and chemical containers, heat exchangers, etc. The chemical composition of the substrate is presented in Table 1.

Table 1 - Chemical composition of the steel used as substrate.

	Si	**Mn**	**Cr**	**Ni**	**P**	**S**	**Others**	**Fe**
Percentual (wt%)	0.75	2.0	19.0	9.0	0.045	0.03	0.1	balance

Source: The author.

The discs had their surface ground using SiC sandpaper with progressively smaller grain size (meshes n° 120, 240, 320, 600, 1200, 2500) and polished using monocrystalline diamond suspensions (6, 3, 1 µm of particle size) and colloidal silica (0.05 µm) to provide a smooth and parallel surface for deposition of the coatings. The mean arithmetic roughness (Ra) achieved for the substrate surface prior to deposition was 3 nm. After polishing, the disks were cleaned in an ultrasonic bath for 5 minutes with acetone and blown dried.

4.2.2. Sputtering

The depositions were carried out in a HiPIMS 250 PVD chamber (Plasma LIITS, Brazil). The sputtering chamber is a high vacuum reactor equipped with two resistive heaters and four water cooled planar magnetrons that allow for the use of four different targets (dimensions of 220 mm x 110 mm), each that can be connected to a different power supply. The targets have their surface protected by shutters that can be opened during the deposition steps. The sample holders are built upon a planetary type carousel that not only performs the conventional translational and rotational movement but can also let the sample oscillate in front of the target within a desired angular amplitude in a determined period. The samples sit at 65 mm apart from the targets. A schematic draw of the chamber along with a picture of the PVD plant are presented in Figure 18.

Figure 18 - HiPIMS 250 sputtering chamber at EESC USP (left) and a schematic view of the interior of the PVD plant (right).

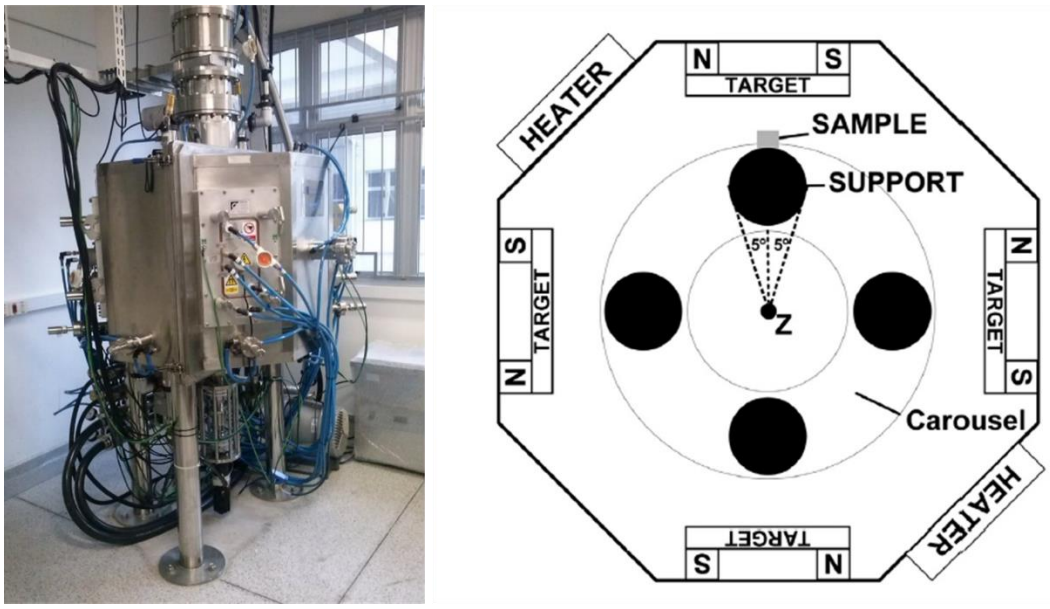

Source: The author (left) and (GUIMARAES et al., 2018) (right).

A TruPlasma Highpulse 4004 (TRUMPF Huetinger, Germany) HiPIMS power supply and a Pinnacle MDX (Adanced Energy, USA) DC power supply were used in the manufacturing of the $Cr_{(1-x)}Al_xN$ coatings. During the sputtering, a negative bias voltage was applied to the substrates in order to enhance the energy of deposition using a Plasma 15 DC power supply (Plasma-LIITS, Brazil).

The deposition steps were as follow:

- Ion etching of the substrate's surface with Cr^+ ions from a Cr target with 99.5% of purity for 1 hour, using HiPIMS discharge of 600 W of average power and bias voltage of -1000 V. The reason for this step is to clear the substrate's surface from organic residues and to cause implantation of Cr beneath the steel surface.
- Deposition of Cr metallic base layer using the same experimental configurations of the deposition of the ceramic coating to improve adhesion between the steel substrate and the nitride film. The thickness of the base layer was set to be around 10% of the thickness of the $Cr_{(1-x)}Al_xN$ coating.
- Deposition of the $Cr_{(1-x)}Al_xN$ coating with varying process parameters.

5. On Manufacturing Multilayer-Like Nanostructures Using Misorientation Gradients in PVD Films

Pedro Renato Tavares Avila, Erenilton Pereira da Silva, Alisson Mendes Rodrigues, Katherine Aristizabal, Fabiola Pineda, Rodrigo Santiago Coelho, Jose Luís Garcia, Flavio Soldera, Magdalena Walczak, and Haroldo Cavalcanti Pinto

This chapter was published in *Scientific Reports* **2019**, 9, 15898.

5.1. ABSTRACT

Due to their applicability for manufacturing dense, hard and stable coatings, Physical Vapor Deposition (PVD) techniques, such as High Power Impulse Magnetron Sputtering (HiPIMS), are currently used to deposit transition metal nitrides for tribological applications. Cr-Al-N is one of the most promising ceramic coating systems owing to its remarkable mechanical and tribological properties along with excellent corrosion resistance and high-temperature stability. This work explores the possibility of further improving Cr-Al-N coatings by modulation of its microstructure. Multilayer-like $Cr_{1-x}Al_xN$ single films were manufactured using the angular oscillation of the substrate surface during HiPIMS. The sputtering process was accomplished using pulse frequencies ranging from 200 to 500 Hz and the resulting films were evaluated with respect to their hardness, Young's modulus, residual stresses, deposition rate, crystallite size, crystallographic texture, coating morphology, chemical composition, and surface roughness. The multilayer-like structure, with periodicities ranging from 250 to 550 nm, were found associated with misorientation gradients and small-angle grain boundaries along the columnar grains, rather than mesoscopic chemical modulation of the microstructure. This minute modification of microstructure along with associated compressive residual stresses are concluded to explain the increased hardness ranging from 25 to 30 GPa, which is at least 20% over that expected for a film of the same chemical composition grown by a conventional PVD processing route

.

5.2. INTRODUCTION

Surfaces of engineering workpieces are often modified by thermal and thermochemical means to improve the tribological and corrosion properties. Surface treatments involve the application of specific thermochemical cycles to a material to obtain desired mechanical and chemical properties (JONES; SCOTT, 1983; HOLMBERG, KENNETH, 2009). In addition, the deposition of films with specific properties has proved advantageous as a further step towards optimum engineering surfaces (JONES; SCOTT, 1983).

The most employed methods of thin film deposition for the modification of engineering surface properties are chemical vapor deposition (CVD), chemical vapor

deposition assisted by plasma (PE-CVD) and physical vapor deposition (PVD). The latter category is very broad, and the High Power Impulse Magnetron Sputtering (HiPIMS) technology represents one of the most recent advances in terms of physical film deposition.

Ceramic coatings are used to protect manufactured parts from thermal and/or corrosive degradation, confer wear resistance by enhancing surface hardness and may diminish friction-associated losses while maintaining toughness and ductility of the core material. Hence, typical applications of hard ceramic coatings are inner surfaces of combustion engines, working surfaces of cutting tools and forming dies, among others (ASTHANA et al., 2006). Transition Metal (TM) nitride films are valuable materials owing to their attractive set of properties, such as thermal conductivity, wear, and chemical resistance, as well as their appearance and esthetic appeal to the customers (SÁNCHEZ-LÓPEZ et al., 2005; SALAMAT et al., 2013; BALOGUN et al., 2017). Among the TM nitrides, CrN exhibits great potential as a film for tribological applications due to its remarkable hardness, wear and corrosion resistance as well as refractory properties, e.g (SHAN et al., 2015). Rock salt fcc-structured CrN coatings are used in automotive combustion engines, e.g. (ZHOU et al., 2008; BELIARDOUH et al., 2015). The addition of Al to the CrN lattice, building up a substitutional solid solution with Cr and having the general stoichiometry of $Cr_{1-x}Al_xN$, can improve the mechanical properties, thermal stability, and wear behavior of CrN-based films (KIM; LEE, 2006; LIN et al., 2010; WANG et al., 2012).

Coatings can be engineered to produce superior properties by tailoring deposition techniques and parameters. The development of multilayered films has been shown effective for improving the mechanical properties, such as hardness, toughness and elastic modulus. Several multilayer architectures with compositional alternation between sub-layers were reported to improve hardness and physical properties of electrical conductivity and diffusional barrier (YASHAR; SPROUL, 1999; PETFORD-LONG; CHIARAMONTI, 2008; WEN et al., 2011). The improvements in mechanical properties of hardness, toughness and stiffness, were found associated with the formation of superlattice structures and with a higher density of layer boundaries that obstruct plastic deformation throughout the coating by acting as a barrier for dislocation gliding (STUEBER et al., 2009).

Buiiliding on the above premises, this work proposes an alternative approach for modyfing mechanical properties through modulation of misoritentation perpendicular

to the engnineered surface. The misorientation gradients are introduced into the $Cr_{1-x}Al_xN$ film architecture by implementing the angular oscillation of the substrate surfaces in front of the Cr50Al50 (at%) targets during HiPIMS. The impact of HiPIMS pulse frequencies ranging from 200 to 500 Hz is evaluated for the same $Cr_{1-x}Al_xN$ film stoichiometry with a crystalline phase indexed as fcc- $Cr_{1-x}Al_xN$.

We believe that the excellent mechanical performance of our multilayer-like nanostructured fcc- $Cr_{1-x}Al_xN$ single films along with the feasibility and scalability towards industrial, will contribute to develop optimized technologies for the upcoming demands of protective layers for high-performance combustion engines with respect to lowest pollutant emissions.

5.3. RESULTS AND DISCUSSION

5.3.1. Coatings morphology

SEM images were acquired from the fracture cross-section and top surface of the $Cr_{1-x}Al_xN$ films manufactured by HiPIMS (Figure 19). At the SEM images of coating fracture cross-section (Figure 19 a-d), it was possible to observe that the films presented a dense and compact structure with columnar grains, which is the typical morphology from zone T in a structure zone model (BARNA, P B; ADAMIK, 1998). FEG-SEM images obtained from the top surface (Figure 19 e-h) confirm the formation of dense films without pores. In addition, morphological cauliflower-like inclusions, common in sputtering processes, are present and randomly distributed on top of the $Cr_{1-x}Al_xN$ films.

Figure 19 - Morphology of the cross-sections and top surface observed in FEG-SEM for $Cr_{1-x}Al_xN$ single films deposited by HiPIMS using the indicated pulse frequencies.

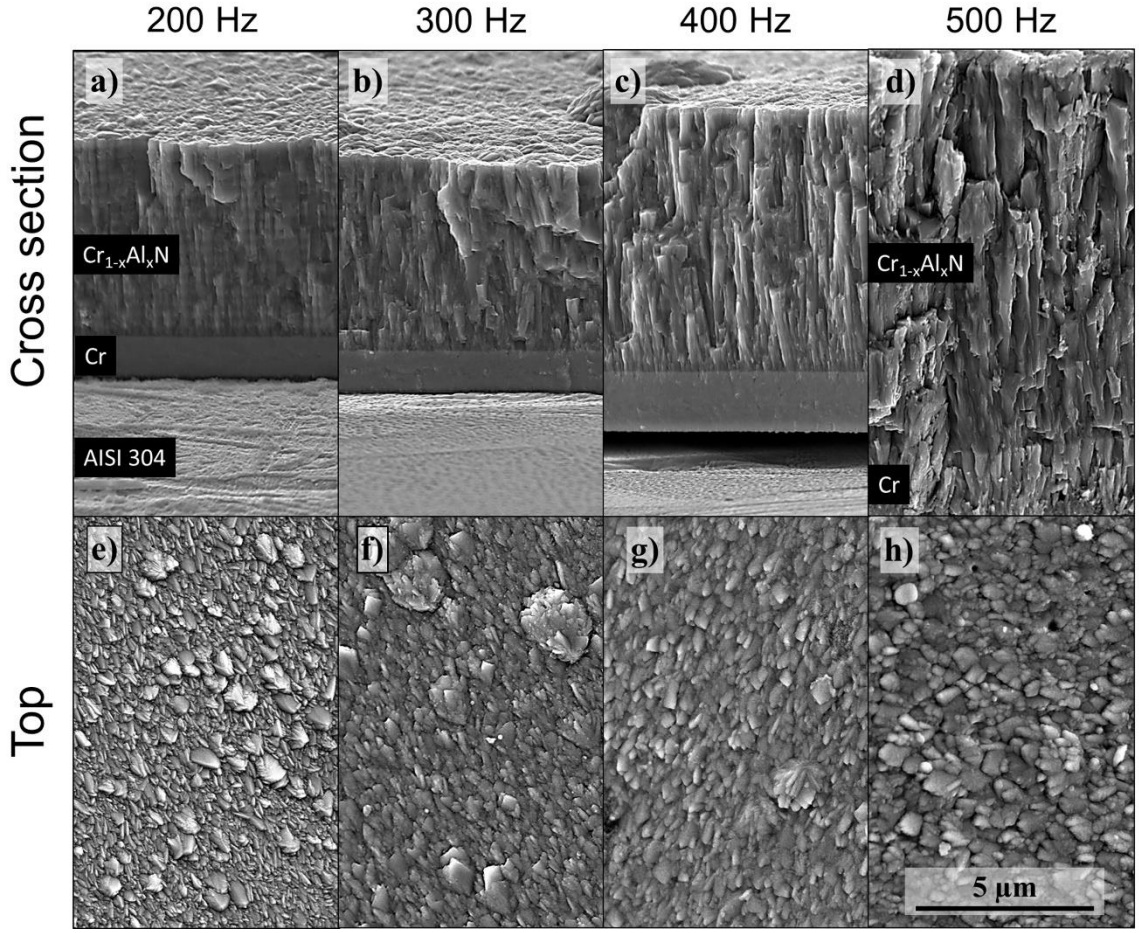

Source: The author.

As displayed in Figure 20, the thickness of the coatings deposited at 500 Hz roughly double that of 200 Hz indicating that the deposition rate increases when pulse frequency is incremented. (Figure 21). The dependence of deposition rate and pulse frequency is consistent with previous studies (GRECZYNSKI, G. et al., 2010; BOBZIN, K et al., 2017; HAYE et al., 2018). Bobzin et al. (BOBZIN, K et al., 2017) measured an increase in metal ionization for shorter frequencies due to higher power peaks. This enhances the self-sputtering mechanism, in which ionized particles are back attracted to the target instead of contributing to the film growth, thus reducing the ion flux to the substrate. Along with that, ionized particles are accelerated when substrate bias is present. Since this was the case for all $Cr_{1-x}Al_xN$ films deposited in this work, a higher degree of ionization at lower frequencies produces a higher number of accelerated particles arriving at the substrate. Since the energy of bombardment on the growing

film is greater in this case, it causes re-sputtering of material already condensed on the substrate surface, and hence reduces the deposition rate [(NEDFORS et al., 2016)].

Figure 20 - Cross-sectional FEG-SEM fracture images of $Cr_{1-x}Al_xN$ film deposited by HiPIMS at 200 Hz (a) and 500 Hz (b). The multilayer-like architecture is present in both images.

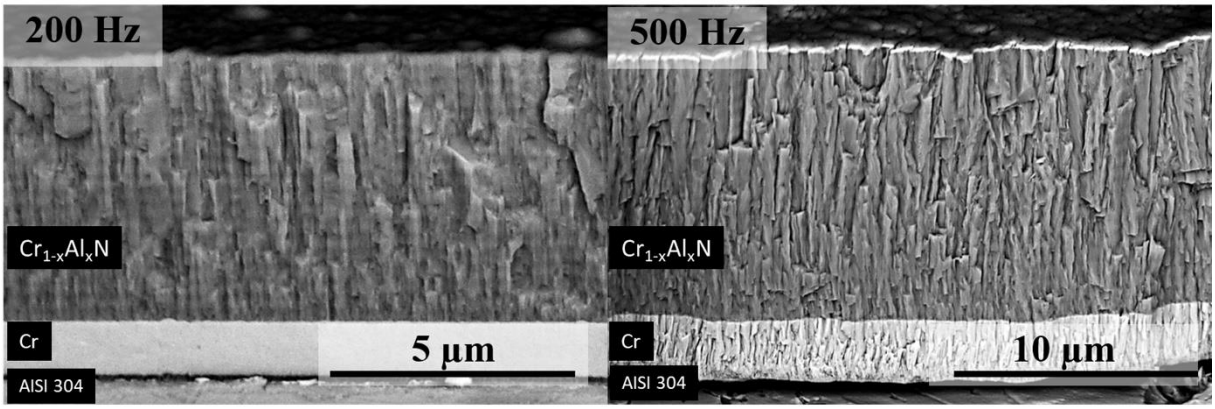

Source: The author.

The multilayer-like architecture was observed throughout the cross-sectional view of the $Cr_{1-x}Al_xN$ single films in which horizontal stripes of higher and lower brightness, causing a wavy profile along the columnar grain boundaries, are apparent, most notably in Figure 20a. The zig-zag morphology of grain growth can be related to the oscillatory motion of the steel discs in front of the Cr50Al50 (at.%) target during deposition. The multilayer-like architecture obtained by substrate oscillation bear some resemblance with helicoidal structures produced by Glancing Angle Deposition (GLAD)[(ROBBIE; BRETT, 2014; BARRANCO; BORRAS; GONZALEZ-ELIPE, AGUSTIN R; et al., 2016), however, due to the high angles of deposition usually involved in the later, and to the unavoidable shadowing effect, GLAD coatings tend to be less dense and compact. During oscillation of the substrate surface, the low angular amplitude and constant angular motion avoid shadowing effects, and the coatings present a compact structure, similar to depositions at a normal incidence angle.

Figure 21 summarizes information regarding deposition rate, calculated and measured multilayer-like periodicities as well as mean surface roughness achieved for each pulse frequency and considering the oscillatory motion with 120 s period. The theoretical periodicity values were predicted using Equation 1, with t being the multilayer-like periodicity, r the deposition rate (shown in Figure 21) and p the period

of oscillatory motion. The measured and calculated periodicities are in good agreement and support the assumption of zig-zag orientation of growth due to the oscillatory motion of the substrate surface in front of the target during deposition.

$$\mathbf{t} = \mathbf{r} * \mathbf{p} \qquad \text{Eq. (1)}$$

Figure 21 - a) Pulse frequency dependence of the deposition rate for $Cr_{1-x}Al_xN$ films, b) 3D AFM surface maps from the $Cr_{1-x}Al_xN$ films deposited at 200Hz, 300Hz, 400Hz and 500Hz.

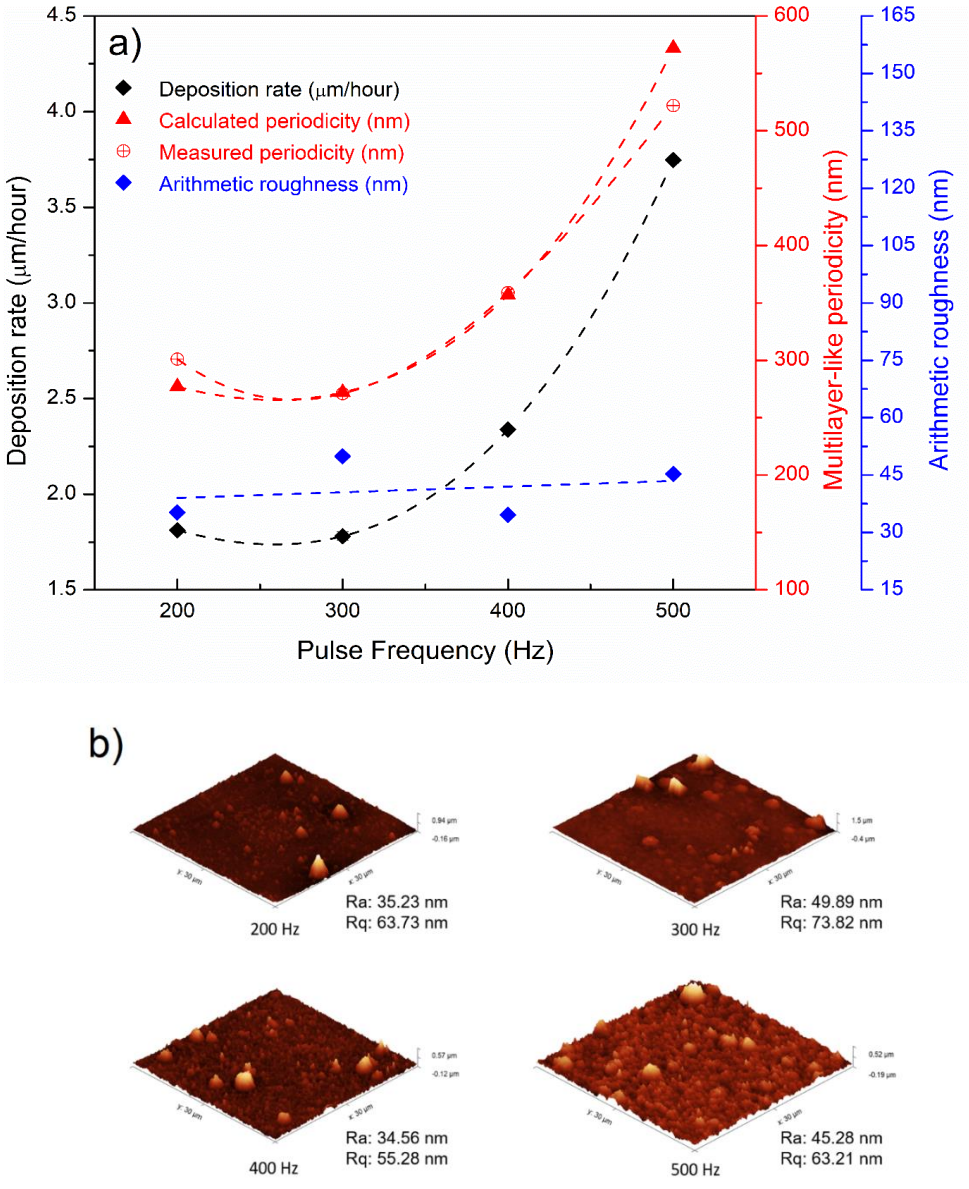

Source: The author.

The dependence of the mean arithmetic surface roughness (Ra) on the pulse frequency was determined from 3D AFM analyses (Figure 21 b). As displayed in Figure

21 a, all $Cr_{1-x}Al_xN$ films exhibited low Ra values. In addition, no systematic change in surface finishing can be attributed to the variation in pulse frequency.

5.3.2. Chemical composition

The chemical composition of all $Cr_{1-x}Al_xN$ films was determined using GDOES. All coatings presented a similar chemical composition profile, and no dependency on pulse frequency was verified. The GDOES analyses illustrated in Figure 22 were carried out for the $Cr_{1-x}Al_xN$ single films deposited at 300Hz and 400 Hz. The chemical composition of the coating is not stoichiometric and the Cr/Al ratio (20/5 at.%) does not coincide with that of the target used in deposition (50/50 at.%). Moreover, there are elevated levels of nitrogen, which can be explained by the N_2 and Ar gases used during deposition (flow rate of 50 sccm and 40 sccm, respectively). The transitions from the $Cr_{1-x}Al_xN$ film to the Cr base layer and then to the AISI 304L steel substrate are visible. No effects of the multilayer-like structure are present in the chemical depth profile, thus indicating that there are no relevant chemical changes throughout the multilayer-like architecture.

Figure 22 - GDOES depth profile of chemical composition throughout the multilayer-like $Cr_{1-x}Al_xN$ single film and the Cr base layer deposited onto AISI 304L steel substrate by HiPIMS at 300Hz and 400 Hz. Transitions from $Cr_{1-x}Al_xN$ film to the Cr base layer.

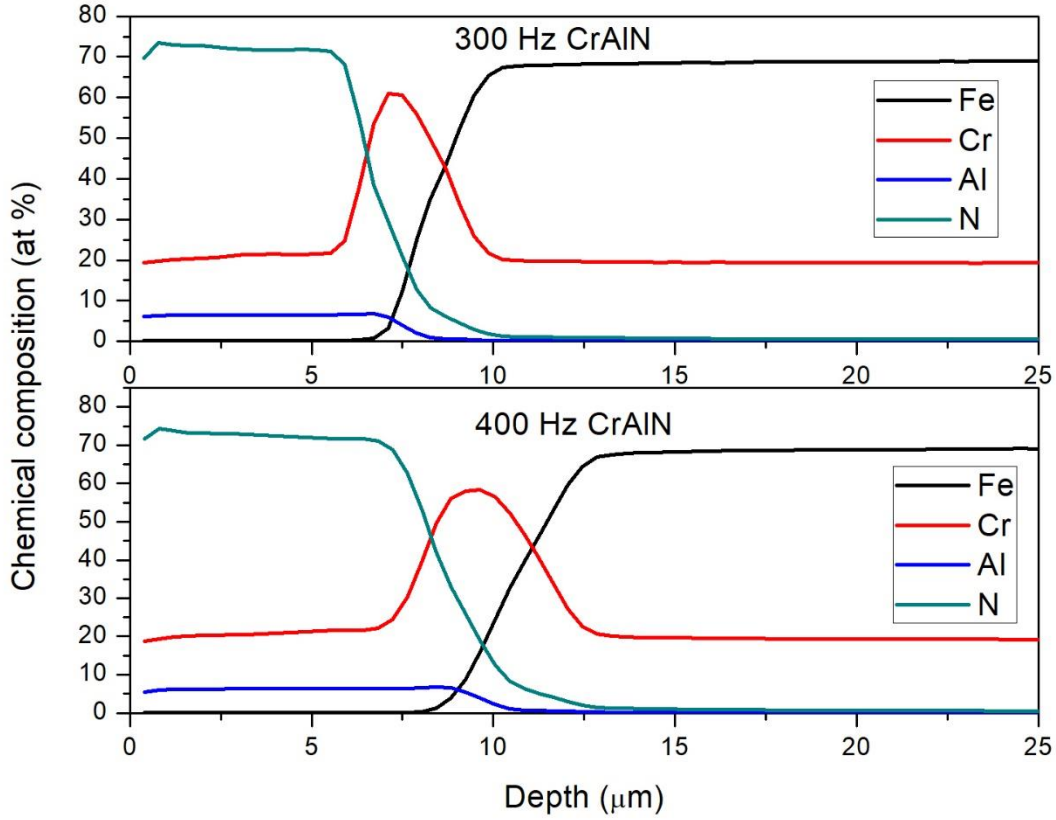

Source: The author.

5.3.3. Microstructure evaluation

XRD phase analyses were performed using θ-2θ diffractograms to characterize the $Cr_{1-x}Al_xN$ films deposited at different pulse frequencies (200 Hz, 300 Hz, 400 Hz, and 500 Hz), see Figure 23.

Besides the peaks relative to the metallic Cr base layer, all peaks were identified as belonging to fcc- $Cr_{1-x}Al_xN$. This demonstrates that no hcp-AlN was built up and the entire Al-content was maintained in the solid solution of the fcc- $Cr_{1-x}Al_xN$ phase. Moreover, no hcp-Cr_2N phase was encountered due to the elevated N_2/Ar ratio used during HiPIMS.

Figure 23 (a) θ -2θ x-ray diffractograms from multilayer-like $Cr_{1-x}Al_xN$ single films deposited by HiPIMS at different pulse frequencies (200 Hz, 300 Hz, 400 Hz, and 500 Hz); (b) Crystallite size dependence on the HiPIMS pulse frequency for $Cr_{1-x}Al_xN$ multilayer-like single films (200 Hz, 300 Hz, 400 Hz, and 500 Hz).

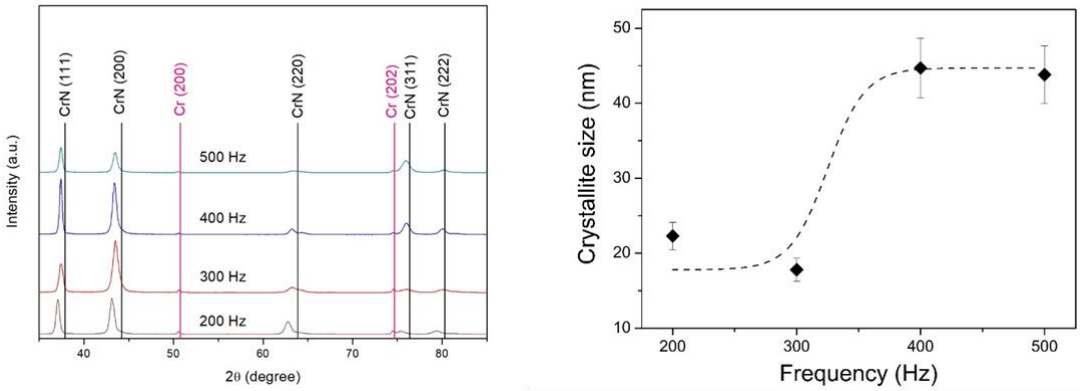

Source: The author.

All peaks present a shift to lower 2θ angles, if compared to the reference fcc-CrN lines, with lower shifts occurring for higher frequencies. Besides a reduction of lattice parameter as a result of Al-addition, it indicates that in the surface normal direction (ND), i.e. the direction of film growth, the lattice spacings are increased. This is likely due to a Poisson-conditioned transversal expansion caused by the existence of elevated in-plane compressive residual stresses, which are typically generated by ion bombardment of coatings during PVD processes.

All multilayer-like $Cr_{1-x}Al_xN$ single films exhibited strong (111)/(200) fiber texture components, both typical in the growth of CrN films (ABADIAS, 2008), as they have higher atomic packing density and, therefore, lower surface energy in B1 NaCl structure (LIN et al., 2008). However, the strain energy also matters and can be minimized during film condensation by diffusion of arriving material to lower density planes (WANG et al., 2012). When pulse frequency decreases, the power peaks increase to maintain the average power density, and the degree of ionization is also enhanced. As a result of this process, more energy is provided to the growing film by momentum transfer during collisions, thus enhancing the mobility of adatoms in the surface by substrate heating. Owing to the higher mobility and kinetic energy of atoms, diffusion may take place to minimize strain energy by the growth of less dense planes that can allocate sputtered atoms with lower lattice distortion. This effect can be observed in Figure 23, as peak intensity corresponding to (220) plane increases and to (311) decreases when the pulse frequency is reduced from 500 Hz to 200 Hz. Still,

no substantial texture evolution can be observed, as it was reported before (BOBZIN, K et al., 2017; GUIMARAES et al., 2018; HAYE et al., 2018).

The evolution of crystallite size with the HiPIMS pulse frequency is displayed in Figure 23. It can be noticed that there is an influence of frequency on crystallite size. The increase of crystallite size with frequency was also observed by [(NEDFORS et al., 2016)]. This was associated with the less energetic bombardment of the growing film due to the lower ratio of ion to neutral atom during sputtering in conditions of high pulse frequency. Hence, a smaller number of grain boundaries will be formed and, thus, there will be larger crystallites. In contrast to the microstructure coarsening, the lower power peaks generated by high pulse frequencies lead to fewer lattice imperfections and lattice distortion during the crystallite growth.

5.3.4. TEM evaluation of multilayer-like structures in $Cr_{1-x}Al_xN$ films

To further understand the formation and nature of the multilayer-like architecture observed in the FEG-SEM images (Figure 20), TEM analyses were conducted. Figure 24 reports an Inverse Pole Figure (IPF) map with respect to the direction of film growth obtained via precession electron diffraction of the TEM lamella from the multilayer-like $Cr_{1-x}Al_xN$ single film deposited by HiPIMS at 200 Hz. Blue and purple grains corresponding to planes with orientation between (001) and (111) are in larger fraction, in accordance with the strongest fiber textures observed in the XRD analyses (Figure 23). The presence of in-grain misorientation is visible in the IPF map as color gradients within the columnar grains.

The dark field TEM image of the $Cr_{1-x}Al_xN$ film deposited at 200 Hz (Figure 24 b) reveals that the columnar grains exhibit a zig-zag morphology of grain growth (red arrows), which are consistent with the multilayer-like periodicities measured using FEG-SEM and calculated based on Eq. (1) and (Figure 21). However, in Figure 24, image analyses indicate that the period of those zig-zag structures is roughly 275 nm (distance between two red arrows). This is in good agreement with the results of calculated periodicities in Figure 21 and confirms the correlation between the angular oscillation of substrate surfaces and the zig-zag morphology of grain growth. One can notice that there are no abrupt change or interface between the sub-layers, as in conventional multi-layers, but rather a smooth change in the direction of grain growth, which resembles the formation of small-angle grain boundaries (SAGB) within the columnar grains. This is expected due to the continuous motion of the substrate

surface along 10° of oscillation amplitude. In addition, the grain boundaries, as a result of the zig-zag morphology of grain growth, evolve a corrugated arrangement, as it can be also visualized in Figure 24 b.

Figure 24 - High resolution characterization of the multilayer-like $Cr_{1-x}Al_xN$ single film deposited by HiPIMS at 200 Hz: (a) IPF map of multilayer-like $Cr_{1-x}Al_xN$ single film deposited by HiPIMS at 200 Hz obtained by precession electron diffraction; (b) dark field TEM image, where red arrows indicate the zig-zag morphology of grain growth responsible for the multilayer-like structure observed in previous FEG-SEM images; and (c) color key for the stereographic standard triangle of cubic structures.

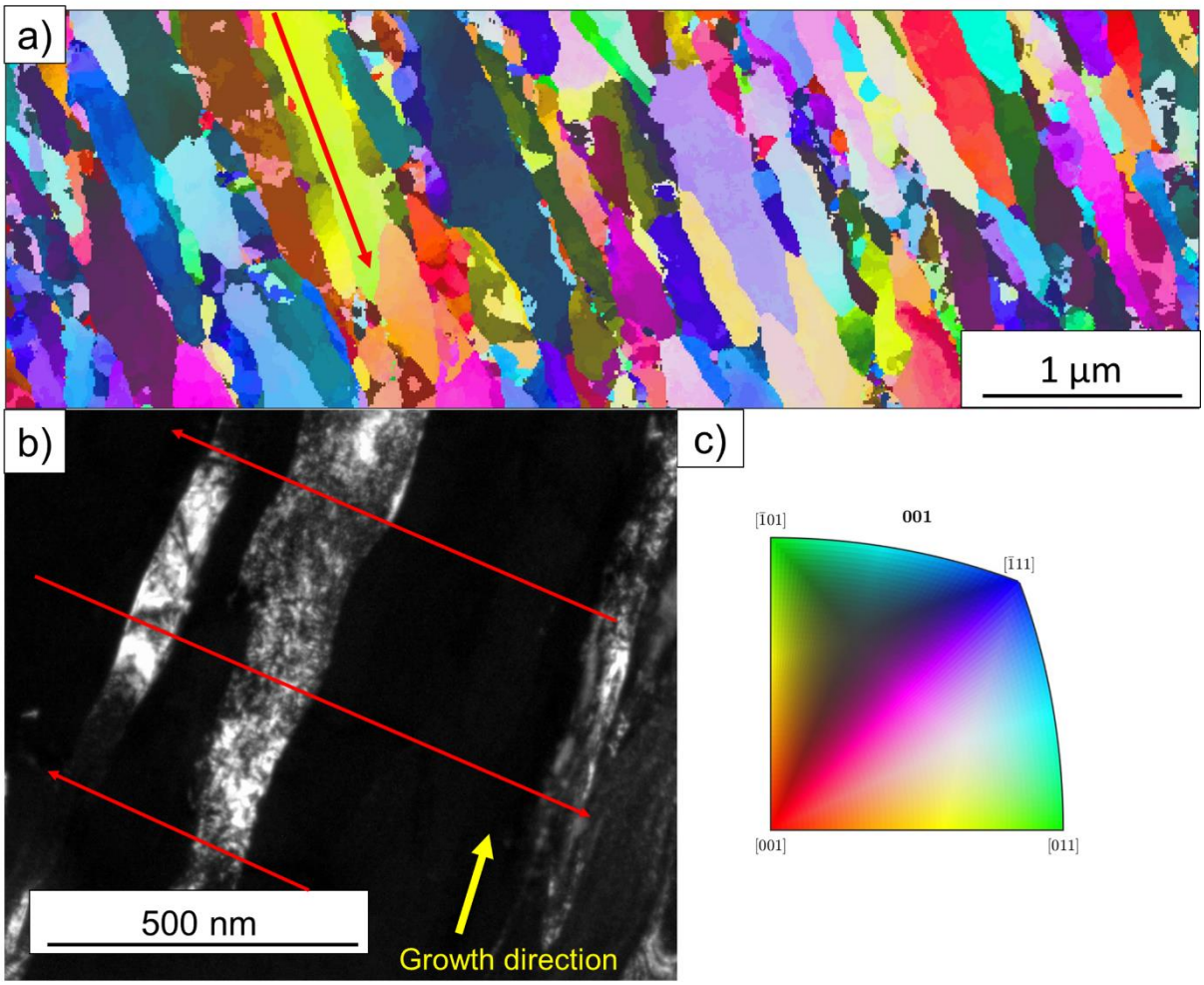

Source: The author.

To quantify the misorientation gradient inside the columnar grains, a misorientation plot is displayed in Figure 25 a. These measurements were performed along a single columnar grain in the direction of film growth, as detailed by the red arrow in Figure 25 a. It can be observed that there is a gradient of misorientation along the columnar grains of a few degrees. It is also noticeable that the angular shift

decreases in periodic steps. These steps are of the same order of magnitude as the multilayer-like periodicities induced by the zig-zag structures measured in Figure 24 b and coincide with the measured and calculated periodicity for 200 Hz pulse frequency, i.e. approximately 275 nm. This indicates that the multilayer-like architecture observed by FEG-SEM and TEM analyses are formed by shifts of a few degrees in the direction of grain growth, which is caused by differences in incidence angle of the sputtered ions, since the target is always stationary, and the substrate surface is oscillating with a period of -5°/+5°. This creates a misorientation gradient which generates, however, SAGB and is not enough to interrupt the columnar growth or cause the nucleation of new grains, as can be seen on the Figure 25 b.

Figure 25 - (a) Misorientation versus distance plot corresponding to the red arrow in Figure 24 a. It shows in detail the misorientation gradient of a few degrees and its periodic decrease related to the multilayer-like architecture. (b) Schematic representation of the microstructure defining a multilayer-like single film.

(a)

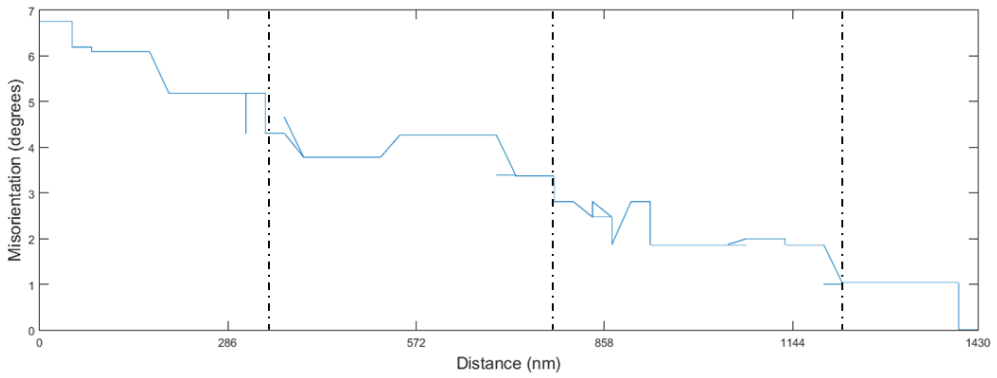

(b)

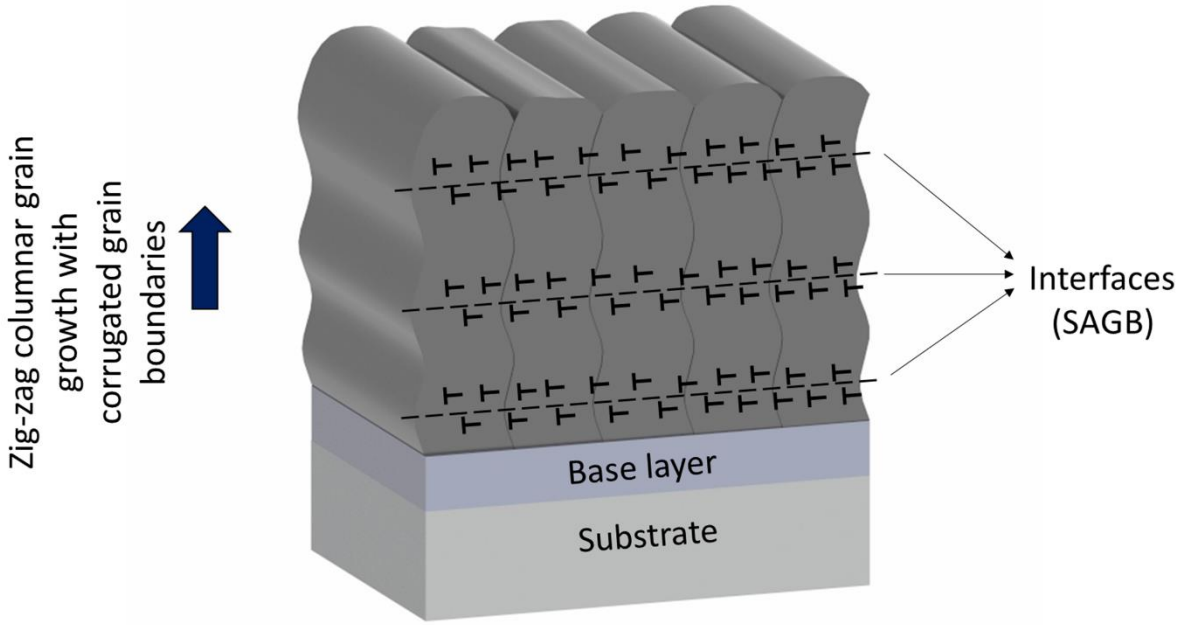

Source: The author.

5.3.5. Mechanical properties

Figure 26 shows the influence of pulse frequency on the mechanical properties of multilayer-like $Cr_{1-x}Al_xN$ single films, such as residual stresses, hardness, and elastic modulus. All $Cr_{1-x}Al_xN$ films exhibited compressive residual stresses. The compressive stresses diminish as pulse frequency rises from 200 to 300 Hz. This behavior has been reported by other authors (BOBZIN, K et al., 2017) and can also be explained by the change in ionization degree with the HiPIMS pulse frequency. As the bombardment energy decreases at higher frequencies, the in-plane film strain will decrease owing to the reduction of lattice displacements, gas implantation within the film, induction of substitutional or interstitial defects and other growth defects that contribute to intrinsic residual stresses in PVD coatings. This corroborates the lower compressive stress levels for the films deposited at higher frequencies [(ABADIAS, 2008)].

These results are also in good agreement with the diffraction line shifts to lower 2θ angles and the lower 2θ shifts observed for higher frequencies, which are clearly visible in the θ-2θ diffractograms measured in the surface ND, i.e. the direction of film

growth (Figure 24 a). This is associated with Poisson-related expansion in the surface ND as a result of compressive in-plane residual stresses.

Since $Cr_{1-x}Al_xN$ films deposited at lower frequencies presented higher compressive stress levels and higher mobility of atoms due to more elevated power peaks applied to the sputtering targets, diffusion may take place to minimize strain energy by the growth of less dense lattice planes that can allocate dislodged atoms with lower lattice distortion. This can explain the occurrence of (220) and (311) fiber texture components in Figure 24 a, as the HiPIMS pulse frequency is diminished from 500 to 200 Hz.

Figure 26 - Correlation between pulse frequency used for deposition of multilayer-like $Cr_{1-x}Al_xN$ single films and the resulting in-plane residual stresses, hardness, and elastic modulus.

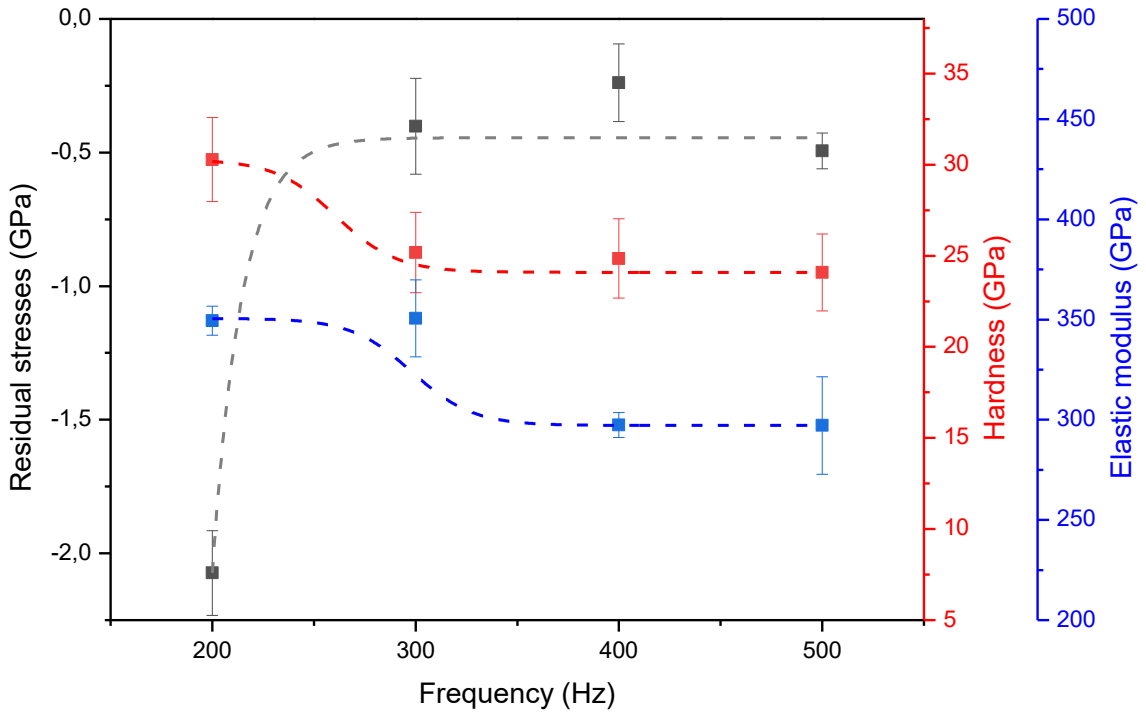

Source: The author.

Although previous works (BOBZIN, K et al., 2017) reported a trend of increasing coating hardness with increasing pulse frequency or no influence of frequency on hardness, even though compressive residual stresses decrease (HAYE et al., 2018), this was not the case in this study as hardness along with the compressive residual stresses exhibited a trend to decrease for increasing frequencies (Figure 26). One of the reasons suggested to explain this behavior is the lack of expressive texture

changes for different frequencies, as observed previously (NEDFORS et al., 2016). Moreover, there can be a significant effect of the multilayer-like structures described previously. Since they are formed by misorientation gradients, and consequently by SAGB inside the columnar grains, the multilayer-like architecture contributes to the formation of additional intrinsic residual stresses and interferes with dislocation gliding and plastic deformation during indentation. Hence, as the sub-layers become thicker for higher frequencies, i.e. higher deposition rates (Figure 26), the effect of misorientation gradients may become less important, and their impact on hardness and compressive stresses are less evident.

5.4. CONCLUSIONS

Dense and compact $Cr_{1-x}Al_xN$ films were obtained with multilayer-like structure defined by minute microstructure modulation perpendicular to the surface. The films are characterized by hardness at least 20% higher over conventional film structure, which was shown tunable between 25 and 30 GPa for the periodicities ranging from 250 to 550 nm, respectively. This enhancement in mechanical properties is associated with elevated compressive residual stresses and an increased number of obstacles to dislocation gliding as shown for the low HiPIMS pulse frequencies. The reduction in pulse frequency produces more energetic film deposition, thus diminishing deposition rate and crystallite size. The latter contributes to increase coating hardness. No influence of pulse frequency was observed on the surface finishing of the films. The multilayer-like architecture was manufactured by angular oscillation of the substrate surface in front of the sputtering target without any effect on the overall chemical composition. Hence, the misorientation gradients and small-angle grain boundaries along the columnar grains are concluded to be determinant for the increased hardness. This microstructural improvement of mechanical properties is relatively simple to implement, thus offering a promising concept for novel coatings to be developed for potential use in friction and wear applications.

5.5. EXPERIMENTAL DETAILS

5.5.1. Coating Deposition

AISI 304 steel discs with 30 mm diameter and 10 mm thickness were ground with SiC paper down to #2500 and polished with diamond suspensions of 6, 3 and 1 µm and colloidal silica for a mirror finish. After polished, the discs were cleaned in acetone ultrasonic bath for five minutes and blow dried. The discs were attached to a sample holder inside a HiPIMS-250 (Plasma-LIITS, Brazil) PVD chamber, 65 mm apart from the target surface. The sample holder was fixed to a carousel which, besides a planetary movement, could be programmed to oscillate in front of the targets with a desired amplitude and period (see Fig. 5.9) (GUIMARAES et al., 2018). All substrates were let to oscillate with an amplitude of -5°/+5°, with the 0° position corresponding to the sample surface parallel to the target surface. The entire cycle from 0 to -5º to +5º and back to 0º took 120 s. Prior to deposition, the substrate surfaces were ion etched by Cr^+ ions for 1 hour, using an Ar plasma at 400 °C and a substrate bias of -60 V.

Figure 27 - Schematic view of the HiPIMS-250 PVD chamber during deposition of multilayer-like $Cr_{1-x}Al_xN$ single films.

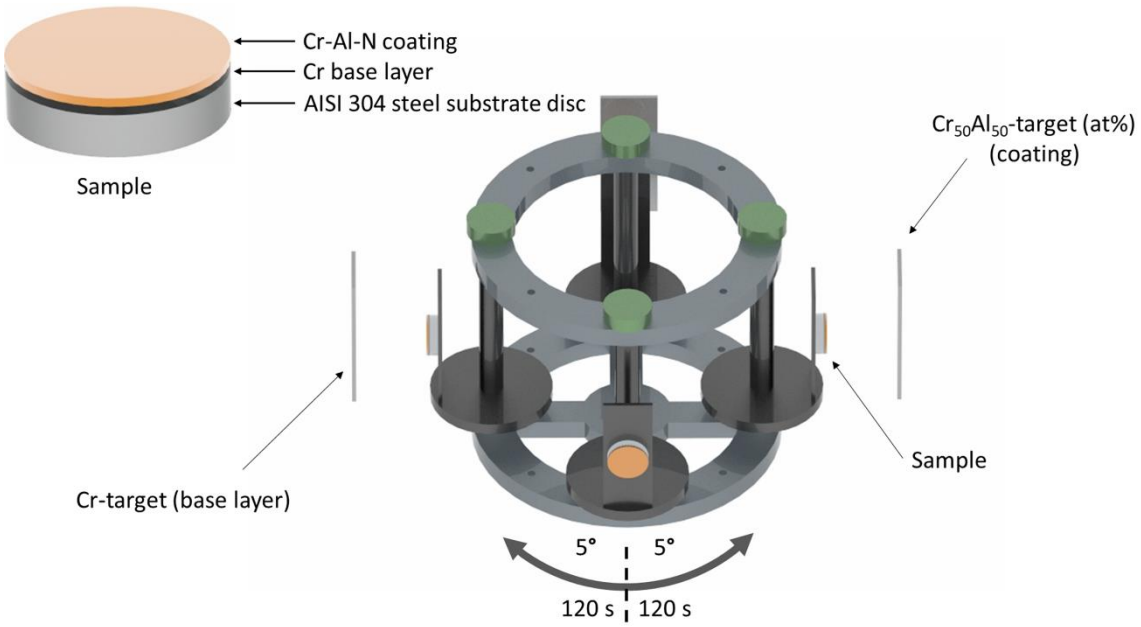

Source: The author.

After the ion etching step, a Cr base layer was deposited using a Cr target of 220 x 110 mm2 during 18 minutes with a working pressure of 2 mtorr, Ar flow of 40

sccm and temperature of 400°C. The substrate DC bias was set to -60 V, which remained the same during the $Cr_{1-x}Al_xN$ deposition for all samples. Last, under N_2/Ar atmosphere (flow of 50 and 40 sccm, respectively, and 2 mtorr working pressure) the $Cr_{1-x}Al_xN$ layers were deposited using a CrAl (50/50 at%) target of 220 x 110 mm2 for 3 hours.

All the above etching and deposition steps used a True Plasma High pulse 4004 (TRUMPF Hüttinger, Germany) power supply operating at 900 W average power. The on-time was set to 200 µs for all experiments. Four different HiPIMS pulse frequencies were investigated: 200, 300, 400, and 500 Hz.

5.5.2. Coating Characterization

X-ray diffraction (XRD) was applied to phase analyses in the Θ-2Θ mode using a Rotaflex Ru200B (Rigaku, Japan) diffractometer equipped with rotative anode and monochromatized Cu Kα radiation (1.5418 Å). Crystallite size was determined using the Scherrer equation (LANGFORD; WILSON, 1978), and Si standard powder sample was used to determine instrumental broadening.

The chemical composition of the $Cr_{1-x}Al_xN$ films was determined by glow discharge optical emission spectroscopy (GDOES) depth profile analysis, which was performed using a Spectruma Analytik GmbH GDA 750 HR equipped with a 2.5 mm diameter anode and operating in DC excitation mode (constant voltage-constant current mode)(FERNÁNDEZ et al., 2019). Every sample was measured by triplicate. In each one, the glow was obtained in argon atmosphere (5.0 quality) and average discharge pressure of 5 x 10-2 hPa. The excitation parameters for the measurements were 1000 V and 12 mA and the sputtering rate was calculated so that the measuring depth was at least 75 µm. Quantitative profiles of Mass Concentration [%] vs Depth were obtained automatically using the standard WinGDOES software(FERNÁNDEZ et al., 2019).

Residual stress analyses were carried out using a MRD-XL (Panalytical, The Netherlands) diffractometer equipped with Mo-Kα radiation (0.7093 Å). The residual stresses were determined by the $\sin^2\psi$ method using 7 ψ-tilts for each sample by varying $\sin^2\psi$ from 0 to 0.9 with increments of 0.15(NOYAN et al., 1987). The (422), (511) and (333) diffraction lines of fcc- $Cr_{1-x}Al_xN$ were used for averaging the dhkl,ψ-$\sin^2\psi$ profiles in the stress analyses due to their high multiplicity and their benefits

therefore with respect to the linearization of texture-induced scattering in the dhkl,ψ-$\sin^2\psi$ profiles.

The $Cr_{1-x}Al_xN$ coating morphology and multilayer-like periodicities were investigated by Scanning Electronic Microscopy equipped with a Field Emission Gun (FEG-SEM). The measurements were conducted using a Field Emission Inspect F-50 (FEI, The Netherlands) electron microscope. The FEG-SEM images were acquired from the top surface and cross-section of the samples. Atomic Force Microscopy (AFM) was carried out using a Nanosurf Flex (Nanosurf, Switzerland) in order to measure the surface finishing after deposition in an area of 30 x 30 µm. Focused Ion Beam (FIB) was employed to prepare TEM lamellas. Transmission Electron Microscopy (TEM) images and crystallographic orientation maps by precession electron diffraction were carried out using a FEI TECNAI G2 LaB_6 TEM microscope (FEI, The Netherlands) equipped with an ASTAR system. The orientation maps were processed using the MTEX Matlab tool. EDS mapping at the TEM was conducted using a JEM 2100 LaB6 (JEOL, USA) TEM microscope equipped with an Oxford EDS Detector (Oxford).

$Cr_{1-x}Al_xN$ coating hardness were measured using instrumented nanoindentation tests at normal forces of 50 mN with a PB1000 mechanical tester (Nanovea, USA) equipped with a Berkovich diamond tip. The indenter was calibrated using a fused silica standard. The Oliver and Pharr equations were considered to calculate the hardness values (PHARR, 1992). At least 7 measurements were performed on top of each coating to determine an average value and its respective standard deviation.

5.6. REFERENCES

Holmberg, Kenneth, A. M. COATINGS TRIBOLOGY Properties, Mechanisms, Techniques and Applications in Surface Engineering. Journal of Chemical Information and Modeling 53, (2009).

Jones, M. H. & Scott, D. (Douglas). Industrial tribology : the practical aspects of friction, lubrication, and wear. (Elsevier Scientific Pub. Co., 1983).

Asthana, R., Kumar, A. & Dahotre, N. Materials Processing and Manufacturing Science. Materials Processing and Manufacturing Science (2006). doi:10.1016/B978-0-7506-7716-5.X5000-6

Balogun, M., Huang, Y. & Qiu, W. Updates on the development of nanostructured transition metal nitrides for electrochemical energy storage and water splitting. Biochem. Pharmacol. 0, (2017).

Salamat, A., Hector, A. L., Kroll, P. & Mcmillan, P. F. Nitrogen-rich transition metal nitrides. Coord. Chem. Rev. 257, 2063–2072 (2013).

Sánchez-López, J. C. et al. Mechanical behavior and oxidation resistance of Cr(Al)N coatings. J. Vac. Sci. Technol. A Vacuum, Surfaces, Film. 23, 681–686 (2005).

Shan, L., Wang, Y., Li, J., Jiang, X. & Chen, J. Tribology International Improving tribological performance of CrN coatings in seawater by structure design. Tribiology Int. 82, 78–88 (2015).

Zhou, F. et al. Friction and wear properties of CrN coatings sliding against Si3N4 balls in water and air. Wear 265, 1029–1037 (2008).

Beliardouh, N. E., Bouzid, K., Nouveau, C., Tlili, B. & Walock, M. J. Tribology International Tribological and electrochemical performances of Cr / CrN and Cr / CrN / CrAlN multilayer coatings deposited by RF magnetron sputtering. Tribiology Int. 82, 443–452 (2015).

Wang, Y. X., Zhang, S., Lee, J. W., Lew, W. S. & Li, B. Influence of bias voltage on the hardness and toughness of CrAlN coatings via magnetron sputtering. Surf. Coatings Technol. 206, 5103–5107 (2012).

Kim, G. S. & Lee, S. Y. Microstructure and mechanical properties of AlCrN films deposited by CFUBMS. 201, 4361–4366 (2006).

Lin, J. et al. Int . Journal of Refractory Metals & Hard Materials Structure and properties of selected (Cr – Al – N , TiC – C , Cr – B – N) nanostructured tribological coatings. Int. J. Refract. Met. Hard Mater. 28, 2–14 (2010).

Petford-long, A. K. & Chiaramonti, A. N. Transmission Electron Microscopy of Multilayer Thin Films ∗. (2008). doi:10.1146/annurev.matsci.38.060407.130326

Yashar, P. C. & Sproul, W. D. Nanometer scale multilayered hard coatings. 55, 179–190 (1999).

Wen, M., Tian, H. W., Hu, C. Q., Zeng, Y. & Meng, Q. N. Modulation periodicity dependent structure , stress , and hardness in NbN / W2N nanostructured multilayer films Modulation periodicity dependent structure , stress , and hardness in NbN / W 2 N nanostructured multilayer films. 123525, (2011).

Stueber, M. et al. Concepts for the design of advanced nanoscale PVD multilayer protective thin films. 483, 321–333 (2009).

Barna, P. B. & Adamik, M. Fundamental structure forming phenomena of polycrystalline films and the structure zone models. 27–33 (1998).

Bobzin, K. et al. Fundamental study of an industrial reactive HPPMS (Cr , Al) N process. 15302, (2017).

Haye, E., Colaux, J. L., Moskovkin, P., Pireaux, J. J. & Lucas, S. Wide range investigation of duty cycle and frequency effects on bipolar magnetron sputtering of chromium nitride. Surf. Coatings Technol. 350, 84–94 (2018).

Greczynski, G., Jensen, J., Böhlmark, J. & Hultman, L. Microstructure control of CrNx films during high power impulse magnetron sputtering. Surf. Coatings Technol. 205, 118–130 (2010).

Nedfors, N. et al. Influence of pulse frequency and bias on microstructure and mechanical properties of TiB2 coatings deposited by high power impulse magnetron sputtering. Surf. Coatings Technol. 304, 203–210 (2016).

Robbie, K. & Brett, M. J. Sculptured thin films and glancing angle deposition : Growth mechanics and applications Sculptured thin films and glancing angle deposition : Growth mechanics and applications. 1460, (2014).

Barranco, A., Borras, A., Gonzalez-elipe, A. R. & Palmero, A. Progress in Materials Science Perspectives on oblique angle deposition of thin films : From fundamentals to devices. Prog. Mater. Sci. 76, 59–153 (2016).

Abadias, G. Stress and preferred orientation in nitride-based PVD coatings. Surf. Coatings Technol. 202, 2223–2235 (2008).

Lin, J. et al. Effect of asynchronous pulsing parameters on the structure and properties of CrAlN films deposited by pulsed closed field unbalanced magnetron sputtering (P-CFUBMS). Surf. Coatings Technol. 202, 1418–1436 (2008).

Guimaraes, M. C. R. et al. On the effect of substrate oscillation on CrN coatings deposited by HiPIMS and dcMS. Surf. Coatings Technol. 340, 112–120 (2018).

Abadias, G. Stress and preferred orientation in nitride-based PVD coatings. 202, 2223–2235 (2008).

Langford, J. I. & Wilson, A. J. C. Scherrer after sixty years: A survey and some new results in the determination of crystallite size. J. Appl. Crystallogr. 11, 102–113 (1978).

Noyan, I. C., Cohen, J. B. M., Cohen, J. B. M. specialist & Cohen, J. B. S. en science des matériaux. Residual stress : measurement by diffraction and interpretation. (Springer-Verlag, 1987).

Pharr, G. M. An improved technique for determining hardness and elastic modulus using load and displacement sensing indentation experiments. J. Mater. Res. 7, 1564–1583 (1992).

6. Nitrogen-Enriched Cr1−xAlxN Multilayer-Like Coatings Manufactured by Dynamic Glancing Angle Direct Current Magnetron Sputtering

Pedro Renato Tavares Avila, Alisson Mendes Rodrigues, Monica Costa Rodrigues Guimarães, Magdalena Walczak, Romualdo Rodrigues Menezes, Gelmires de Araújo Neves and Haroldo Cavalcanti Pinto.

This chapter was published in *Materials* **2020**, 13 (16), 3650.

6.1. ABSTRACT

Multilayer-like CrN and $Cr_{1-x}Al_xN$ coatings with different Al contents were deposited onto a stainless steel substrate using dynamic glancing angle deposition direct current magnetron sputtering (DGLAD dcMS) in a N rich atmosphere to understand the role of Al on the growth of the films and mechanical properties of the nitrides with a multilayer architecture. Chemical analysis by means of energy dispersive analysis (EDS) and glow discharge optical emission spectroscopy (GDOES) depth profiling revealed that while CrN samples were close to stoichiometric, the $Cr_{1-x}Al_xN$ coatings presented excess N between 70 and 80% at. An expressive change in texture was observed as the CrN coating changed its preferred orientation from (111) to (200) with the addition of Al, followed by a modification in morphology from grains with faceted pyramidal tops in CrN to dome-shaped grains in $Cr_{1-x}Al_xN$ coatings. Multilayer-like nanostructures of corrugated grains were produced with a periodicity of approximately 30 nm using dynamic glancing angle deposition. The deposition rate was drastically reduced with an increase of Al, meanwhile, the best mechanical performance was achieved for the coating with a higher content of Al, with hardness up to 27 GPa and a higher value of maximum resistance to plastic deformation.

6.2. INTRODUCTION

In the last decades, transition metal (TM) nitride films have been a field of intense study in surface science and technology. In this context, due to the versatility of manufacturing techniques, the properties of several ceramic systems (TiN, AlN, VN, NbN, ZrN, HfN, and CrN) have been evaluated. The wide variety of properties of this class of ceramic coatings has promoted their application and potential use in various areas, such as wear and corrosion protection, production of optical and magnetic devices, biomedical implants, and aesthetic layers, among others (DAVIS, 1991; MEZGER; CREUGERS, 1992; SERRO et al., 2009; TWARDOWSKI et al., 2015).

Reactive direct current magnetron sputtering (dcMS) is a prominent technique of thin-film production. Basically, in this technique, ions or neutrals are sputtered from a precursor target by a plasma of inert gas (Ar, mostly) entrapped in a magnetic field generated by a magnetron in the vicinity of the target. The sputtered species travel

through the deposition chamber and condense on a substrate surface in the presence of a reactive gas (N_2, CH_4, etc.) (BUNSHAH, 2001). Recently, a variation of conventional sputtering, namely dynamic glancing angle deposition (DGLAD), has been introduced, with continuous motion of the substrate as the film grows, affecting the angle of incidence of the sputtered material and changing the morphology of grains to a corrugated or undulated format (GUIMARÃES et al., 2018; JIMENEZ et al., 2019). It was reported that such oscillatory motion is capable of producing multilayer-like structures that can be tuned by the period and range of oscillation [8].

Reactive magnetron sputtering is subject to several control variables that can impact chemical composition, structure, and properties of the coating. Among these control variables, the reactive gas flow rate is an important parameter because it can determine the stoichiometry of the film. Indeed, reactive magnetron sputtering coatings with an excess of N can be manufactured under high N_2 flow rates (HULTMAN et al., 2002; RISTOLAINEN et al., 2002; PENILLA; WANG, 2008; LU et al., 2018). Nitrogen-rich CrN coatings have already been reported by (KHOJIER et al., 2014; GARZON-FONTECHA et al., 2018; DU et al., 2019), and their results showed that films with the N/TM ratio higher than 1 sometimes presented improved mechanical, optical, and magnetic properties as compared with their stoichiometric counterparts, indicating that N-rich TM nitrides could be an interesting choice in the engineering design of thin films.

TM nitride coatings have been improved even further by adding a ternary component to the system, as is the case for (Ti, Al)N and (Cr, Al)N (CHAUHAN; RAWAL, 2014). Cr-based coatings are known to act as an important corrosion and oxidation barriers for metal substrates due to formation of Cr_2O_3 and other Cr-based phases that can passivate the surface, as described in the literature (GILEWICZ et al., 2016; DROZDZ et al., 2017; AMANOV, 2019). The production of ternary CrAlN has been reported to increase even more anticorrosive and oxidation protection, along with hardness and wear resistance (BARSHILIA et al., 2006; TLILI et al., 2010). In (SCHEERER et al., 2005), it was reported that Al addition on CrN structure coatings affected their properties and the machining performance. In addition, nitrogen addition improved the life of the film based on wear and turning tests.

Therefore, this study aims to understand the effects of the Al/Cr ratio on the growth and mechanical properties of multilayer-like coatings of Cr-Al-N prepared by reactive magnetron sputtering with excess N content by fixing a high N_2 flow rate (50

sccm) in the reaction chamber and changing the precursor target Al/Cr content. To our knowledge, this is the first work to address this subject.

6.3. MATERIALS AND METHODS

6.3.1. Manufacturing of the Cr-Al-N Ceramic Coatings

The Cr-Al-N ceramic coatings investigated in the present study were manufactured in a Plasma-HiPIMS 250 deposition plant (Plasma-LIITS, Campinas, Brazil) (AVILA et al, 2019). In this plant, both the sputtering process and negative bias tension are provided by MDX Pinnacle DC by Advanced Energy power sources. The chamber has two heating resistances mounted on opposite walls for substrate heating, each one counting with a thermocouple for temperature monitoring. The substrate holder also counts with a third thermocouple to improve temperature control. All coatings were deposited on an AISI 304 stainless steel disc. Before deposition, the discs were ground with 2000 grit sandpaper and polished using 6, 3, and 1 µm diamond suspension and colloidal silica, resulting in a substrate mean roughness of 3 nm. Next, the discs were cleaned in an ultrasonic bath with acetone for 5 min, and blow-dried. Then, inside the plant, sitting 65 mm apart from the targets, the disc surfaces were pretreated by an ion etching process using Cr^+ ions generated by plugging a pure Cr target to a High Power Impulse Magnetron Sputtering (HiPIMS) power supply. The HiPIMS configurations for the ion etching were as follows: 600 W of average power, frequency of 104 Hz, t_{on} of 50 µs, and 900 V. To improve the energy of the impinging Cr^+ ions, a bias tension of −800 V was applied to the substrate (EHIASARIAN et al., 2007; BAKOGLIDIS et al., 2016). The whole process of ion etching took one hour with the purpose of promoting substrate cleaning and shallow implantation of Cr beneath the substrate to improve adhesion between the stainless steel and the coating. After the ion etching, the substrate received a Cr base layer to improve adhesion between the coatings and the substrate. Alloy targets with compositions 50% at Al/50% at Cr and 70% at Al/30% at Cr were used to produce two different sets of samples, and the Cr-Al-N coating manufactured for them were designated as 50/50 $Cr_{1-x}Al_xN$ and 70/30 $Cr_{1-x}Al_xN$, respectively. A reference coating with composition equal to CrN was manufactured from the Cr target. All targets were manufactured by A.M.P.E.R.E Alloys, France, and had a purity of 99.95%. The deposition parameters used to obtain the ceramic coatings investigated in this study are listed in Table 2. The substrates were

oscillated in a dynamic glancing angle deposition (DGLAD) setup, as described in previous work elsewhere (AVILA et al., 2019), with a range and period of oscillation of −5°/+5°, respectively, and period “t” of 12 s, to verify the effect of this novel technique in fast oscillation motion (See Figure 28).

Figure 28 - Schematic top view of the dynamic glancing angle deposition (DGLAD) apparatus responsible for the oscillatory motion during sputtering (not in scale).

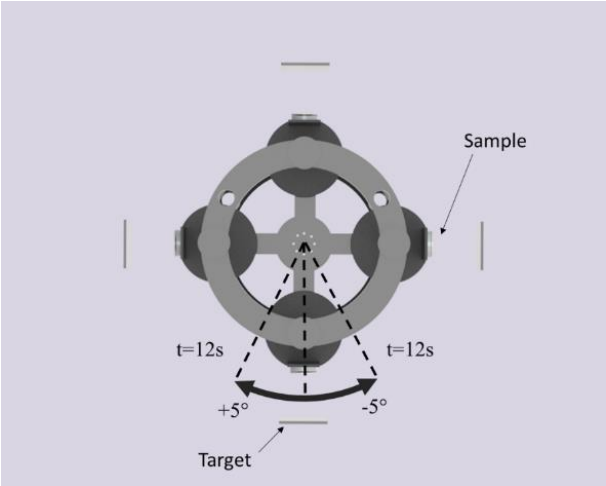

Source: The author.

Table 2 - Constant deposition parameters used to manufacture the CrN and $Cr_{1-x}Al_xN$ ceramic coatings.

Substrate Temperature	400 °C
Ar flow	40 sccm
N_2 flow	50 sccm
DC power	900 W
Negative bias	−120 V
Working pressure	0.266 Pa

Source: The author.

6.3.2. Coating Characterization

Top and cross-section images were acquired with the aid of FEI Inspect-F50 SEM (FEI, Eindhoven, The Netherlands) equipped with a windowless silicon drift detector (SDD) for energy dispersive analysis (EDS) (Apollo X SDD, EDAX, Mahwah, NJ, USA). X-ray diffraction (XRD) analyses in the θ–2θ geometry were carried out using a Rotaflex Ru200B diffractometer (Rigaku, Tokyo, Japan) equipped with a rotative anode and Cu Kα radiation (1.5418 Å).

Coatings chemical compositions were evaluated by glow discharge optical emission spectroscopy (GDOES) depth profile analysis. The measurements were carried out using a GDA 750 HR spectrometer (Spectruma Analytik GmbH, Hof, Germany) with a 2.5 mm diameter anode working in DC excitation mode (constant voltage-constant current mode). Triplicates were measured for each sample. The measurements were conducted under an inert Ar atmosphere (5.0 quality) and average discharge pressure of 5×10^{-2} hPa. The excitation parameters were 1000 V and 12 mA, with a sputtering rate for measuring depth of at least 75 µm. Profiles of mass concentration (%) vs. depth from atomic concentration (%) vs. depth were plotted using the WinGDOES.

Atomic force microscopy (AFM) measurements (area of 30 × 30 µm) in tapping mode were performed using a NanosurfFlex (Nanosurf, Liestal, Switzerland) to measure the coating surface finishing after deposition. The hardness of the coatings and elastic modulus were determined using instrumented nanoindentation tests at maximum normal forces of 50 mN with a PB1000 (Nanovea, Irvine, CA, USA) mechanical tester equipped with a Berkovich diamond tip. The indenter was calibrated using a fused silica standard. The Oliver and Pharr equations were used to calculate the hardness values (PHARR, 1992). At least 7 measurements were performed on top of each coating to determine an average value.

The $\sin^2 \psi$ method with 7 ψ tilts was accomplished to measure residual stresses, for each sample (with $\sin^2 \psi$ ranging from 0 to 0.9) (NOYAN et al., 1987). Due to their high multiplicity, the (422), (511), and (333) diffraction lines of fcc-$Cr_{1-x}Al_x$ N were used for averaging the d hkl-$\sin^2 \psi$ profiles in the stress analyses. A Panalytical MRD-XL (Panalytical, Almelo, The Netherlands) diffractometer equipped with Mo-Kα radiation (0.7093 Å) was used for all measurements.

The scanning transmission electron microscopy (STEM) images were produced using a JEOL JEM-2100 microscope (JEOL, Tokyo, Japan) equipped with a thermionic emission LaB6 electron gun, available at LNNano, Campinas, Brazil.

6.4. RESULTS AND DISCUSSION

Investigations were conducted to understand the impact of fast substrate oscillation during dcMS depositions and also the effect of Al addition to coatings produced under N-rich atmospheres in different aspects of the resulting nitrides, to

indicate whether or not they were suitable for hard coating applications. This section is subdivided concerning the impact of such modifications in different aspects of the coatings.

6.4.1. Chemical Composition and Microstructure

EDS chemical analysis accomplished with a windowless SDD in the CrN coating revealed that its chemical composition was 49 ± 2 at. % N and 51 ± 2 at. % Cr, which is close to stoichiometry. The GDOES was used to evaluate the chemical composition (in-depth profiling) of the $Cr_{1-x}Al_xN$ coatings manufactured with different Al/Cr precursor ratios, see Figure 29. In both $Cr_{1-x}Al_xN$ coatings deposited, a high nitrogen content (~70–80%) was observed, which emphasizes its non-stoichiometric character. The manufactured coatings also had a higher concentration of Cr than Al even when produced using the 70/30 target.

Figure 29 - Glow discharge optical emission spectroscopy (GDOES) chemical depth profiling of the $Cr_{1-x}Al_xN$ coatings.

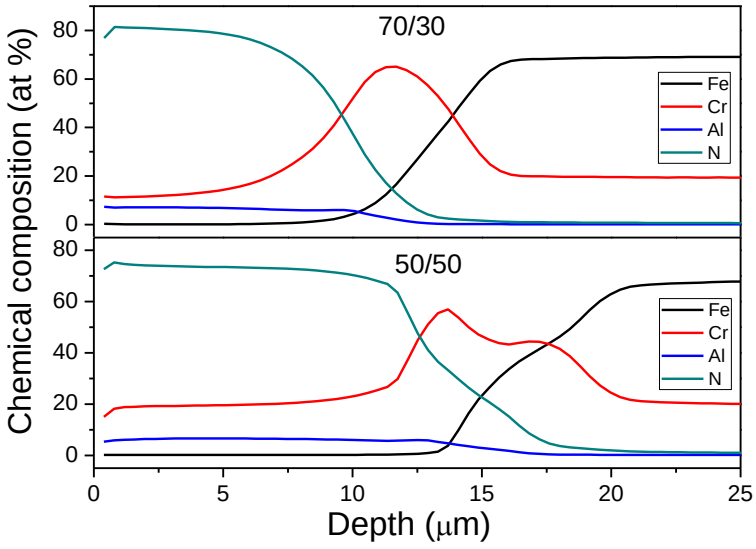

Source: The author.

Gas flow rates from 50 to 40 sccm of N_2 and Ar, respectively, which have been proven to be adequate for deposition of stoichiometric CrN, produced N rich $Cr_{1-x}Al_xN$ coatings. This could possibly be explained by the significantly higher sputtering yield of Cr as compared with Al (LAEGREID; WEHNER, 1961). Additionally, (DING; ZENG, 2005) attributed this lower sputtering yield of Al to the poisoning of the target surface by an AlN layer on the surface of the target. This becomes particularly relevant for

large N2 partial pressures. Such a layer is promoted by the higher amount of Al in the 70/30 target and results in less material arriving from the target to the substrate. The preferential sputtering of Cr due to formation of AlN could possibly explain the small content of Al in coatings produced using the 70/30 nominal target.

A 50% increase in relative Cr content is observed from the 70/30 $Cr_{1-x}Al_xN$ to the 50/50 $Cr_{1-x}Al_xN$ coating. It is important to observe that at the same pace that Cr content increases, the atomic N concentration changes from around 80% in the 70/30 $Cr_{1-x}Al_xN$ to 75% in the 50/50 $Cr_{1-x}Al_xN$. The difference in nitrogen concentration could also be an effect of the lower sputtering yield of the targets containing more Al (formation of the AlN layer). Therefore, with a lower flux of metallic particles arriving at the substrate from the target, the coating tends to be nitrogen richer. Nevertheless, in Figure 29, a broad Cr peak can be observed at approximately 12 µm for the 70/30 $Cr_{1-x}Al_xN$ coating. This corresponds to the metallic Cr interlayer deposited previously on the nitride layer. In the case of the 50/50 $Cr_{1-x}Al_xN$ coating, a double peak is noticed. This indicates that Cr could have been implanted in the substrate as a result of the pretreatment of the surface of the substrate with Cr^+ ion.

In addition, the thickness of the coating can be estimated from the depth profile, since N and Al are meant to be present only in the nitride layer, with the base layer being richer in Cr. One can notice that there is a continuous non-abrupt interface between the two layers and that the Al richer 70/30 coating is roughly 2 microns thinner than the 50/50 coating, although both were deposited under the same deposition parameters.

Figure 30 shows the XRD diffractograms measured from CrN and $Cr_{1-x}Al_xN$ coatings. Coatings containing Al presented sharp peaks related to the (200) plane of the CrN B1 cubic structure, in contrast to previous studies [14,22], in which no AlN or Al peaks were observed, even for the coating with a higher Al/Cr ratio. It was also evident that no other nitrides or oxides were formed, since the CrN cubic structure with Al solid solution was the only phase identified. In agreement with the reference position (dotted line) (EDDINE et al., 1977), (200) peaks were dislocated to smaller 2θ angles, which indicated shrinkage of the interplanar spacing (d). This was an effect of the presence of in-plane compressive residual stresses in the coatings (NOYAN et al., 1987). In addition, the presence of Al contributed to the contraction of the lattice parameters, causing shifting in the CrN peak positions to lower than 2θ.

Figure 30 - Θ–2Θ XRD measurements from coatings showing strong dependency on Al presence. Peaks position is related to the B1-CrN structure (ICSD 00-001-0065 reference).

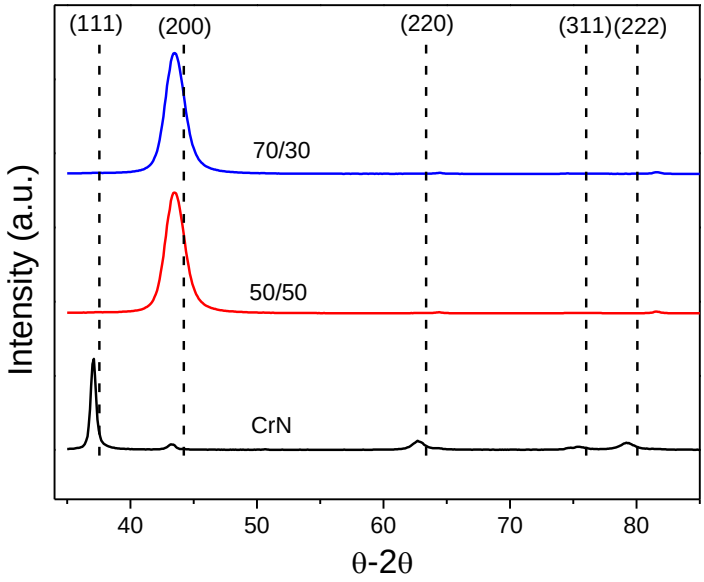

Source: The author.

The XRD diffractogram measured from the CrN reference coating (see Figure 30) also indicated the formation of solely cubic B1-CrN with strong texture related to the (111) plane. The evident difference in texture between the $Cr_{1-x}Al_xN$ and CrN can be explained by the lower sputtering yield of the alloy Cr-Al targets as compared with the Cr target. In the case of the former, while growing in an N-rich atmosphere, the film receives an arriving flow of predominantly N_2 molecules and much smaller flux of Cr or Al neutrals or ions. Therefore, the formation of planes with higher N contents is expected in the surface, at the expense of metal-rich planes, which is the case of (200), in the CrN B1 structure. The lower deposition rate also favors the preferred orientation that minimizes surface energy (LU et al., 2018), which is (200) in the case of CrN, making it even more favorable as the preferential orientation (PELLEG et al., 1991).

In addition, the CrN coating receives a higher flux of metal from the Cr pure target during growth as compared with Cr1−xAlxN, even for the same N_2 flow rate, and develops texture of the type (111), which is a metal richer plane and also minimizes strain energy generated by the higher deposition rate (PETROV et al., 2003; LU et al., 2018).

6.4.2. Coating Morphology

FEG-SEM cross-section images are shown in Figure 31. The CrN coating presents a structure characteristic of Zone II of a structure zone model (SZM)

(PETROV et al., 2003), with a homogeneously dense structure through its entire thickness. The 50/50 $Cr_{1-x}Al_xN$ coating exhibits a less homogeneous structure, with thinner columns at the bottom of the film and “v” shaped grains at the top, which is characterized as a T Zone in the same SZM. The 70/30 $Cr_{1-x}Al_xN$ coating, which is Al-richer, displays a similar morphology to that of the 50/50 condition, in a zone of dense but “V” shaped columnar grains.

Figure 31 - SEM images acquired from the cross-section view of the Cr-Al-N ceramic coatings. All images are in the same scale.

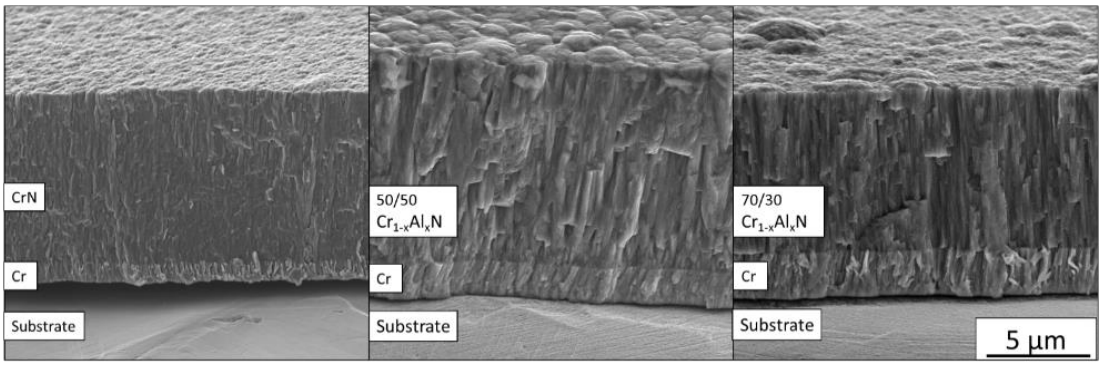

Source: The author.

The average coating thickness follows the trend observed in the GDOES results, i.e., samples with higher contents of Al are the samples with the lower average deposition rate. The lower deposition rates visible in Figure 32 for coatings with a higher Al/Cr ratio also can be explained by the higher sputtering yield of Cr as compared with Al or Cr-Al alloys in reactive sputtering.

Figure 32 - Deposition rate as a function of the Al/Cr ratio.

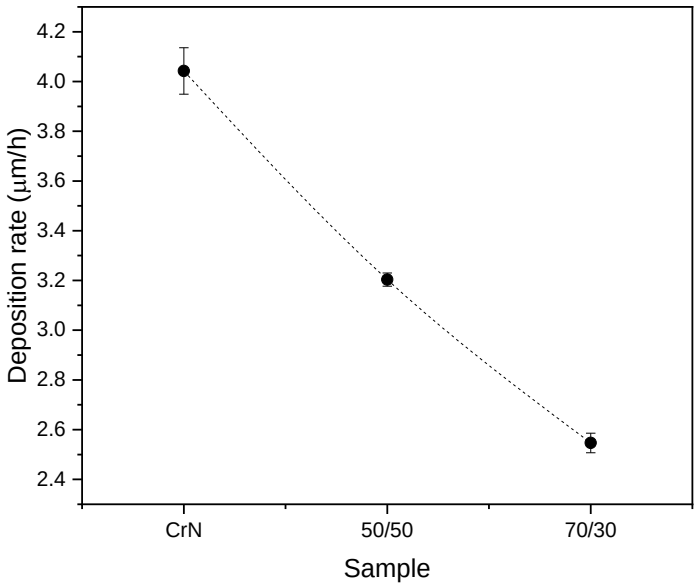

Source: The author.

The top SEM images and the AFM surface profile map are presented in Figure 33. All three coatings show dense surfaces with few pores or voids and densification increasing with Al content. The CrN surface presents a faceted pyramidal shape with some lateral facets, which is typical of nitride films grown with (111) preferential orientation (DELISLE; KRZANOWSKI, 2012; LU et al., 2018). As the Al was added, the grains' top morphology change to round domes, which is also expected for a B1-type crystal textured in the (200) preferential orientation to decrease the overall surface tension (DELISLE; KRZANOWSKI, 2012). These observations on the surface shape of grains confirm the texture change behavior observed in Figure 33.

In both Al-containing coatings, it was possible to see round morphological defects of a few microns distributed along the surface. These defects are inherent in the sputtering process and unavoidable to some level (BISWAS; PURANDARE, Y.; et al., 2018; BISWAS; PURANDARE, YASHODHAN; et al., 2018). We observed that CrN presented finer grains and the addition of Al increased grain size. This was possibly due to the modification in growth morphology related to the change in texture. The 50/50 coating presented apparent larger grains with bigger domes, which are also visible in the cross-section images in Figure 33.

The effects of grain size and the presence of morphological defects have an impact on surface roughness. As illustrated in the surface maps in Figure 33 and presented in Table 3, CrN demonstrates lower roughness than the Al-containing

coatings, with an increase of almost 40% in roughness as Al is added. This is due to the smaller dome size and an apparent absence of morphological defects, as observed in Figure 33. The 70/30 coating has a smoother surface than the 50/50 condition, due also to their difference in dome size.

Figure 33 - SEM images top view and atomic force microscopy (AFM) surface mapping of the Cr–Al–N ceramic coatings. All images are in the same scale.

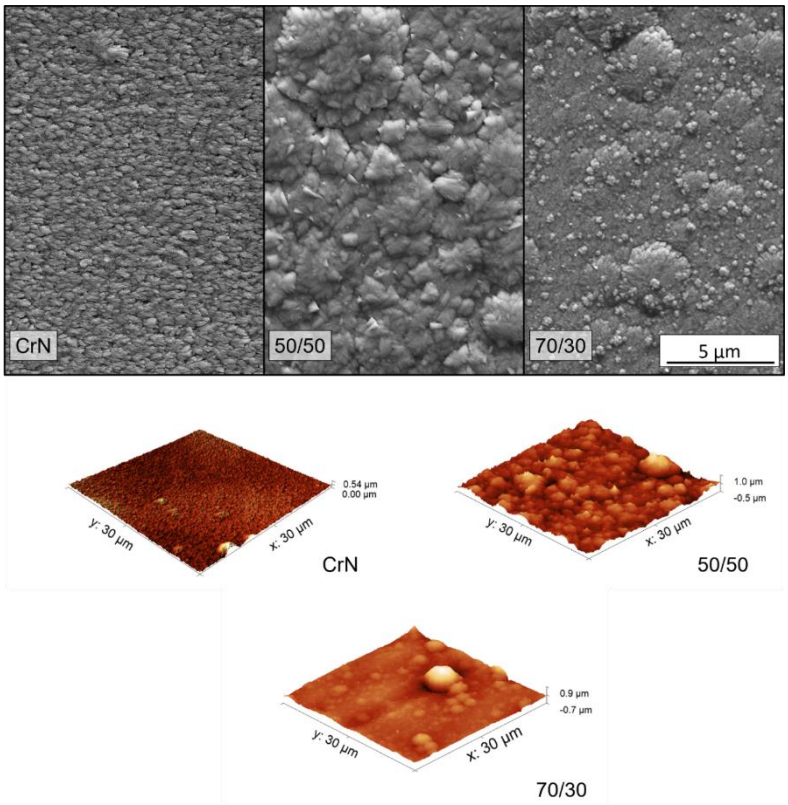

Source: The author.

Table 3 - Values of mean arithmetic roughness and H^3/Er^2

Coatings	Mean Arithmetic Roughness Ra (nm)	H^3/Er^2 (GPa)
CrN	35.3	0.08117
50/50	129.2	0.07398
70/30	76.9	0.17868

Source: The author.

The effect of dynamic glancing angle deposition is demonstrated in Figure 34 for the 70/30 coating. As a result of the oscillatory motion of the substrate during sputtering within the range of +5°/−5° and period of 12 s, the columnar grains present

a corrugated morphology at the boundaries (as exemplified in brackets in Figure 34). These corrugated zig-zag columnar grains are associated with in-grain misorientation due to differences in the angle of sputtering flux (GUIMARAES et al., 2018; AVILA et al., 2019; JIMENEZ et al., 2019). Figure 34 displays corrugated structures with periodicity ten-fold smaller, in the order of 30 nm, indicating that even fast oscillatory motions, with period as small as 12 s, are able to create such grain morphology. It was demonstrated by [8,31], and (JIMENEZ et al., 2020) that for coatings prepared by DGLAD, the properties were dependent on the period of oscillation, such as crystallite size, texture, and hardness. Therefore, these thin undulated features enhanced the performance of the coatings.

Figure 34 - Bright field scanning transmission electron microscopy (STEM) image showing the corrugated nature of grain boundaries as a result of DGLAD growth in the 70/30 coating.

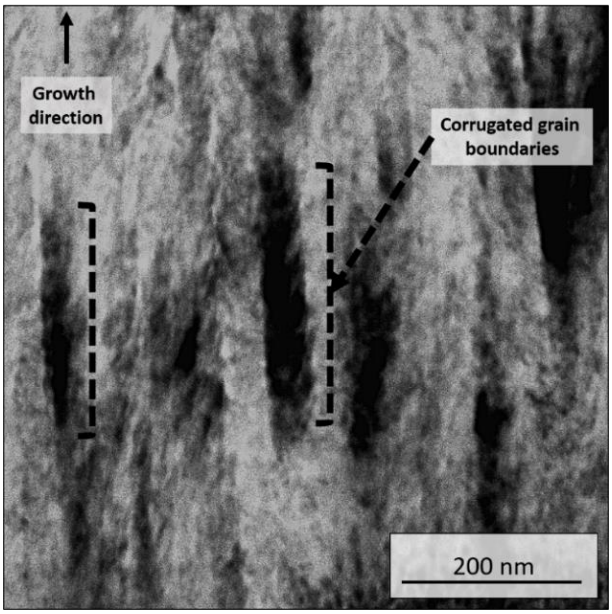

Source: The author.

6.4.3. Mechanical Properties

The presence of residual stresses was confirmed by the XRD measurements performed using the $\sin^2 \psi$ technique, see Figure 35. It shows the compressive stresses of hundreds of MPa as a result of the deposition process. On the one hand, the smallest compressive residual stresses were measured on the CrN coating. On the other hand, higher stress levels were measured on the 50/50 $Cr_{1-x}Al_xN$ coating, which

was slightly more significant than those observed for the 70/30 $Cr_{1-x}Al_xN$ coating. Since all depositions were carried out using the same temperature conditions, power supply, bias, and chamber pressure, the same substrate heat was expected for all processes. Therefore, the difference in the chemical composition of the precursor target must be the only factor influencing the residual stresses on the films. The more significant compressive state of the $Cr_{1-x}Al_xN$ coatings indicates that beyond the octahedral interstices normally occupied by nitrogen in a stoichiometric cubic CrN structure, the tetrahedral interstices in the lattice are also being occupied by the excess N, causing it to be strained (RISTOLAINEN et al., 2002).

Figure 35 - Hardness, elastic modulus, and residual stress as a function of the Al/Cr ratio.

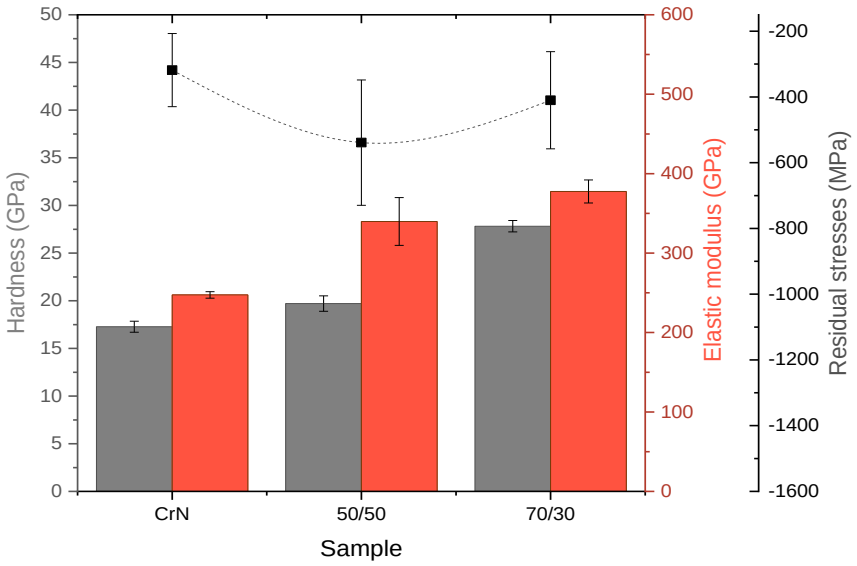

Source: The author.

Figure 35 presents the hardness and elastic modulus values measured by nanoindentation. In general, both hardness and elastic modulus increased with Al addition in the CrN coating. In this way, the highest Al/Cr ratio presented the highest hardness, with an improvement of around 37% as compared with the Al-free CrN reference. The behaviors are both in agreement with previous literature and can be explained by the solid solution hardening mechanism of Al in the CrN lattice (REITER et al., 2005; TLILI et al., 2010; FAN et al., 2017). For the sake of comparison, the bare AISI 304 substrate surface hardness was measured to be 3.4 ± 0.2 GPa, indicating that an expressive improvement in surface mechanical properties is achieved even for the Al free coating.

H^3/Er^2 is often related to resistance to plastic deformation (LEYLAND; MATTHEWS, 2000). Although the reduced elastic modulus (Er) does not take into account plasticity effects [40], it is a simple way to predict the coatings' toughness and response to wear that requires no special sample preparation, especially for monolayer ceramic films. The H^3/Er^2 results are presented in Table 3. The film produced in the 50/50 $Cr_{1-x}Al_xN$ condition presented the lowest value of H^3/Er^2, which could be an effect of the higher value residual stresses, as presented in Figure 35.

6.5. CONCLUSIONS

CrN and $Cr_{1-x}Al_xN$ coatings with different Al contents were successfully manufactured using the DGLAD dcMS technique under an N-richer atmosphere. The DGLAD technique produced a multilayer-like architecture by growing corrugated grains with periodicity around 30 nm, indicating the capacity of this technique to tune the architecture of grains even at small scales. It was observed that the chemical depth profile was not influenced by the multilayer-like structure and, for the same deposition conditions, the CrN coating presented a chemical composition close to stoichiometric, whereas the $Cr_{1-x}Al_xN$ films exhibited excess N, up to almost 80%, caused by a decrease in metal flux to the substrate as the Al-containing suffered poisoning, i.e., formation of the phase AlN on the surface of target. The deviation between the target precursor chemistry and the composition of the resulting coatings could also have been an effect of the target poisoning and a decrease in metal flux during deposition. The nitrogen enrichment changed the preferential growth orientation from (111) in CrN to (200) in Cr1−xAlxN. This change in texture caused the surface morphology of the coatings to go from a pyramid shape to a round dome form. The Al-richest coating presented the best mechanical performance, with higher hardness and resistance to plastic deformation as a result of solution hardening caused by Al. In this study, the presented results indicate that the combination of DGLAD and dcMS produce coatings with competitive mechanical properties as compared with techniques described in the literature, even in conditions of non-stoichiometry, and can serve as prospects for current industrial applications of hard coatings. A systematic variation of the substrate oscillation amplitude during dcMS appears to be a fundamental parameter to optimize grain misorientation within the coatings and further enhance the mechanical and tribological performance of single films with multilayer-like architecture.

6.6. REFERENCES

1. Davis, R.F. III-V Nitrides for Electronic and Optoelectronic Applications. *Proc. IEEE* **1991**, *79*, 702–712, doi:10.1109/5.90133.
2. Serro, A.P.; Completo, C.; Colaço, R.; dos Santos, F.; da Silva, C.L.; Cabral, J.M.S.; Araújo, H.; Pires, E.; Saramago, B. A comparative study of titanium nitrides, TiN, TiNbN and TiCN, as coatings for biomedical applications. *Surf. Coat. Technol.* **2009**, *203*, 3701–3707, doi:10.1016/j.surfcoat.2009.06.010.
3. Mezger, P.R.; Creugers, N.H.J. Titanium nitride coatings in clinical dentistry. *J. Dent.* **1992**, *20*, 342–344, doi:10.1016/0300-5712(92)90021-4.
4. Twardowski, P.; Legutko, S.; Krolczyk, G.M.; Hloch, S. Investigation of wear and tool life of coated carbide and cubic boron nitride cutting tools in high speed milling. *Adv. Mech. Eng.* **2015**, *7*, 1–9, doi:10.1177/1687814015590216.
5. Bunshah, R.F. *Handbook of Hard Coatings Deposition Technologies, Properties and Applications*; William Andrew: New York, NY, USA, 2001; ISBN 9780815514381.
6. Jimenez, M.J.M.; Antunes, V.; Cucatti, S.; Riul, A.; Zagonel, L.F.; Figueroa, C.A.; Wisnivesky, D.; Alvarez, F. Physical and micro-nano-structure properties of chromium nitride coating deposited by RF sputtering using dynamic glancing angle deposition. *Surf. Coat. Technol.* **2019**, *372*, 268–277, doi:10.1016/j.surfcoat.2019.05.023.
7. Guimarães, M.C.R.; De Castilho, B.C.N.M.; Cunha, C.; Correr, W.R.; Mordente, P.; Alvarez, F.; Pinto, H.C. On the effect of aluminum on the microstructure and mechanical properties of CrN coatings deposited by HiPIMS. *Mater. Res.* **2018**, *21*, 1–6, doi:10.1590/1980-5373-MR-2017-0848.
8. Avila, P.R.T.; da Silva, E.P.; Rodrigues, A.M.; Aristizabal, K.; Pineda, F.; Coelho, R.S.; Garcia, J.L.; Soldera, F.; Walczak, M.; Pinto, H.C. On manufacturing multilayer-like nanostructures using misorientation gradients in PVD films. *Sci. Rep.* **2019**, *9*, 1–10, doi:10.1038/s41598-019-52226-1.
9. Ristolainen, E.O.; Molarius, J.M.; Korhonen, A.S.; Lindroos, V.K. A study of nitrogen-rich titanium and zirconium nitride films. *J. Vac. Sci. Technol. A Vac. Surf. Films* **2002**, *5*, 2184–2189, doi:10.1116/1.574950.
10. Hultman, L.; Sundgren, J.-E.; Markert, L.C.; Greene, J.E. Ar and excess N incorporation in epitaxial TiN films grown by reactive bias sputtering in mixed Ar/N_2 and pure N_2 discharges. *J. Vac. Sci. Technol. A Vac. Surf. Films* **2002**, *7*, 1187–1193, doi:10.1116/1.576251.
11. Penilla, E.; Wang, J. Pressure and Temperature Effects on Stoichiometry and Microstructure of Nitrogen-Rich TiN Thin Films Synthesized via Reactive Magnetron DC-Sputtering. *J. Nanomater.* **2008**, *2008*, 267161, doi:10.1155/2008/267161.
12. Lu, L.; Luo, F.; Huang, Z.; Zhou, W.; Zhu, D. Influence of the nitrogen flow rate on the infrared emissivity of TiNx films. *Infrared Phys. Technol.* **2018**, *88*, 144–148, doi:10.1016/j.infrared.2017.11.015.
13. Khojier, K.; Savaloni, H.; Zolghadr, S.; Amani, E. Study of Electrical, Mechanical, and Tribological Properties of CrNx Thin Films as a Function of Sputtering Conditions. *J. Mater. Eng. Perform.* **2014**, *23*, 3444–3448, doi:10.1007/s11665-014-1148-8.
14. Garzon-Fontecha, A.; Castillo, H.A.; Restrepo-Parra, E.; De La Cruz, W. The role of the nitrogen flow rate on the transport properties of CrN thin films produced by DC magnetron sputtering. *Surf. Coat. Technol.* **2018**, *334*, 98–104, doi:10.1016/j.surfcoat.2017.11.009.
15. Du, J.; Zhou, H.; Sun, C.; Kou, H.; Ma, Z.; Wang, X.; Dai, J. Growth structure effect on the corrosion resistance and mechanical properties of CrNx coating. *Surf. Rev. Lett.* **2020**, *27*, 1950091, doi:10.1142/s0218625x19500914.
16. Chauhan, K.V.; Rawal, S.K. A Review Paper on Tribological and Mechanical Properties of Ternary Nitride based Coatings. *Procedia Technol.* **2014**, *14*, 430–437, doi:10.1016/j.protcy.2014.08.055.
17. Amanov, A. Surface engineering-controlled tribological behavior and adhesion strength of Ni-Cr coating sprayed onto carburized AISI 4340 steel substrate. *Surf. Coat. Technol.* **2019**, *370*, 144–156, doi:10.1016/j.surfcoat.2019.04.087.

18. Drozdz, M.; Kyzioł, K.; Grzesik, Z. Chromium-based oxidation-resistant coatings for the protection of engine valves in automotive vehicles. *Mater. Tehnol.* **2017**, *51*, 603–607, doi:10.17222/mit.2016.151.
19. Gilewicz, A.; Chmielewska, P.; Murzynski, D.; Dobruchowska, E.; Warcholinski, B. Corrosion resistance of CrN and CrCN/CrN coatings deposited using cathodic arc evaporation in Ringer's and Hank's solutions. *Surf. Coat. Technol.* **2016**, *299*, 7–14, doi:10.1016/j.surfcoat.2016.04.069.
20. Barshilia, H.C.; Selvakumar, N.; Deepthi, B.; Rajam, K.S. A comparative study of reactive direct current magnetron sputtered CrAlN and CrN coatings. *Surf. Coat. Technol.* **2006**, *201*, 2193–2201, doi:10.1016/j.surfcoat.2006.03.037.
21. Tlili, B.; Mustapha, N.; Nouveau, C.; Benlatreche, Y.; Guillemot, G.; Lambertin, M. Correlation between thermal properties and aluminum fractions in CrAlN layers deposited by PVD technique. *Vacuum* **2010**, *84*, 1067–1074, doi:10.1016/j.vacuum.2010.01.011.
22. Scheerer, H.; Hoche, H.; Broszeit, E.; Schramm, B.; Abele, E.; Berger, C. Effects of the chromium to aluminum content on the tribology in dry machining using (Cr,Al)N coated tools. *Surf. Coat. Technol.* **2005**, *200*, 203–207, doi:10.1016/j.surfcoat.2005.02.112.
23. Bakoglidis, K.D.; Schmidt, S.; Greczynski, G.; Hultman, L. Improved adhesion of carbon nitride coatings on steel substrates using metal HiPIMS pretreatments. *Surf. Coat. Technol.* **2016**, *302*, 454–462, doi:10.1016/j.surfcoat.2016.06.048.
24. Ehiasarian, A.P.; Wen, J.G.; Petrov, I. Interface microstructure engineering by high power impulse magnetron sputtering for the enhancement of adhesion. *J. Appl. Phys.* **2007**, *101*, 054301, doi:10.1063/1.2697052.
25. Pharr, G.M. An improved technique for determining hardness and elastic modulus using load and displacement sensing indentation experiments. *J. Mater. Res.* **1992**, *7*, 1564–1583, doi:10.1557/JMR.1992.1564.
26. Noyan, I.C.; Cohen, J.B.M.; Cohen, J.B.S. En science des matériaux. In *Residual Stress: Measurement by Diffraction and Interpretation*; Springer: New York, NY, USA, 1987; pp. 117–163; ISBN 9781461395713.
27. Laegreid, N.; Wehner, G.K. Sputtering yields of metals for Ar+ and Ne+ ions with energies from 50 to 600 ev. *J. Appl. Phys.* **1961**, *32*, 365–369, doi:10.1063/1.1736012.
28. Ding, X.Z.; Zeng, X.T. Structural, mechanical and tribological properties of CrAlN coatings deposited by reactive unbalanced magnetron sputtering. *Surf. Coat. Technol.* **2005**, *200*, 1372–1376, doi:10.1016/j.surfcoat.2005.08.072.
29. Eddine, M.N.; Bertaut, E.F.; Roubin, M.; Paris, J. Etude cristallographique de Cr1−xVxN à basse temperature. *Acta Crystallogr. Sect. B Struct. Crystallogr. Cryst. Chem.* **1977**, *33*, 3010–3013, doi:10.1107/s0567740877010164.
30. Pelleg, J.; Zevin, L.Z.; Lungo, S.; Croitoru, N. Reactive-sputter-deposited TiN films on glass substrates. *Thin Solid Films* **1991**, *197*, 117–128, doi:10.1016/0040-6090(91)90225-M.
31. Petrov, I.; Barna, P.B.; Hultman, L.; Greene, J.E. Microstructural evolution during film growth. *J. Vac. Sci. Technol. A Vac. Surf. Films* **2003**, doi:10.1116/1.1601610.
32. Delisle, D.A.; Krzanowski, J.E. Surface morphology and texture of TiAlN/CrN multilayer coatings. *Thin Solid Films* **2012**, *524*, 100–106, doi:10.1016/j.tsf.2012.09.073.
33. Biswas, B.; Purandare, Y.; Khan, I.; Hovsepian, P.E. Effect of substrate bias voltage on defect generation and their influence on corrosion and tribological properties of HIPIMS deposited CrN/NbN coatings. *Surf. Coat. Technol.* **2018**, *344*, 383–393, doi:10.1016/j.surfcoat.2018.03.009.
34. Biswas, B.; Purandare, Y.; Sugumaran, A.; Khan, I.; Hovsepian, P.E. Effect of chamber pressure on defect generation and their influence on corrosion and tribological properties of HIPIMS deposited CrN/NbN coatings. *Surf. Coat. Technol.* **2018**, *336*, 84–91, doi:10.1016/j.surfcoat.2017.08.021.
35. Guimaraes, M.C.R.; de Castilho, B.C.N.M.; de Souza Nossa, T.; Avila, P.R.T.; Cucatti, S.; Alvarez, F.; Garcia, J.L.; Pinto, H.C. On the effect of substrate oscillation on CrN coatings deposited by HiPIMS and dcMS. *Surf. Coat. Technol.* **2018**, *340*, 112–120, doi:10.1016/j.surfcoat.2018.02.028.
36. Jimenez, M.J.M.; Antunes, V.G.; Zagonel, L.F.; Figueroa, C.A.; Wisnivesky, D.; Alvarez, F. Effect of the period of the substrate oscillation in the dynamic glancing angle deposition technique: A

columnar periodic nanostructure formation. *Surf. Coat. Technol.* **2020**, *383*, 125237, doi:10.1016/j.surfcoat.2019.125237.

37. Reiter, A.E.; Derflinger, V.H.; Hanselmann, B.; Bachmann, T.; Sartory, B. Investigation of the properties of Al1-xCrxN coatings prepared by cathodic arc evaporation. *Surf. Coat. Technol.* **2005**, *200*, 2114–2122, doi:10.1016/j.surfcoat.2005.01.043.
38. Fan, Q.X.; Zhang, J.J.; Wu, Z.H.; Liu, Y.M.; Zhang, T.; Yan, B.; Wang, T.G. Influence of Al content on the microstructure and properties of the CrAlN coatings deposited by arc ion plating. *Acta Metall. Sin.* **2017**, *30*, 1221–1230, doi:10.1007/s40195-017-0656-6.
39. Leyland, A.; Matthews, A. On the significance of the H/E ratio in wear control: A nanocomposite coating approach to optimised tribological behaviour. *Wear* **2000**, *246*, 1–11, doi:10.1016/S0043-1648(00)00488-9.
40. Chen, X.; Du, Y.; Chung, Y.W. Commentary on using H/E and H3/E2 as proxies for fracture toughness of hard coatings. *Thin Solid Films* **2019**, *688*, 137265, doi:10.1016/j.tsf.2019.04.040.

7. Impact of the range of substrate oscillation on microstructure and mechanical performance of Cr-Al-N coatings produced by HiPIMS and dcMS in Dynamic Glancing Angle setup

7.1. INTRODUCTION

Transition metal nitrides have been widely studied in the past decades as candidates for coatings applied to metal surface to provide protection against severe wear and corrosion conditions in diverse industrial branches e.g., machining, automotive, aerospace, bioengineering and others (MEZGER; CREUGERS, 1992; HOVSEPIAN et al., 2008; BRÄUER et al., 2010; GARCIA et al., 2010; BOUSSER et al., 2014; FERREIRA et al., 2020). One of the nitride systems studied is the Cr-Al-N with interesting mechanical properties, good corrosion resistance and high thermal stability, making it an important candidate when designing conjugated systems in surface engineering (BOBZIN et al., 2007; BAGCIVAN et al., 2013; SÁNCHEZ-LÓPEZ et al., 2014).

Several production routes are available to thin films. Magnetron Sputtering (MS) is one of the most important in the manufacturing of hard coatings producing dense and well adhered films (KELLY; ARNELL, 2000; BRÄUER et al., 2010). Along the last decades, variations of MS techniques have been developed focusing on different aspects, being direct current Magnetron Sputtering (dcMS) and High-Power Impulse Magnetron Sputtering (HiPIMS) two of the most studied. DcMS consists in applying direct power to the target and presents higher deposition rate, which is a fundamental factor when considering costs in industrial application (ALTUN; SEN, 2005; SCHMIDT et al., 2016). On the other hand, HiPIMS depositions applies high intensity and short duration power peaks to the target, allowing to significantly enhance ionization of the sputtered materials. This can improve deposition energy and produce denser and harder coatings at the expanse of deposition rate (MÜNZ et al., 2008; ANDERS, 2010a, 2017; HAYE et al., 2018; AVILA et al., 2019).

Along with the materials and techniques chosen for the manufacture of coatings, the deposition geometry is also an important factor. The description of production of films by means of Glancing Angle Depostion (GLAD) is extense in literature (ROBBIE; BRETT, 1997; ROBBIE, 1998; SIT et al., 1999; BARRANCO; BORRAS; GONZALEZ-ELIPE, AGUSTIN R.; et al., 2016; ABADIAS et al., 2019; RYDOSZ et al., 2020). In this type of deposition, the substrate is placed at an oblique angle in relation to the sputtering target, so that the flux of arriving species is off-normal with relation to the substrate surface (BARRANCO; BORRAS; GONZALEZ-ELIPE, AGUSTIN R.; et al., 2016). This geometry propitiates the formation of films with high porosity due to

shadowing effect and tilted columnar grains (MUKHERJEE; GALL, 2013). If the substrate is spun around its normal axis the columnar shape of the grains can be changed to a variety of sculptured formats e.g., helix, zig-zag, etc (BARRANCO; BORRAS; GONZALEZ-ELIPE, AGUSTIN R.; et al., 2016). Several authors reported changes in properties related to these grains sculptures that suggest applications in fields as optics, electronics and chemical catalysis (HAWKEYE; BRETT, 2007; LEONTYEV et al., 2008; MANSOUR et al., 2010; RYDOSZ et al., 2020).

Recently, studies indicated zig-zag grains produced by GLAD present changes in microstructure such as texture and residual stresses that can also impact its mechanical properties (KECKES et al., 2018; DANIEL et al., 2020). A variation of GLAD in which the substrate is rocked in front of the target during deposition, continuously changing the angle of arrival of the sputtered material has been proposed and received the designation of Dynamic Glancing Angle Deposition (GUIMARAES et al., 2018; JIMENEZ et al., 2019). This technique also produces coatings with nanosculpted grains, in the form of zig-zag, for instance. Authors found correlations between these structures and variations on hardness and texture of the coatings (JIMENEZ et al., 2020), as well as misorientation gradients along the zig-zag grains correspondent to the oscillatory motion of the substrate (AVILA et al., 2019), showing a potentiality in tailoring the mechanical performance of hard coatings by engineering the sculpture of its grains.

Despite the studies published addressing the nanostrucuted sculped coatings, its properties, and mechanical characteristics, to our knowledge, none have evaluated the effect of these features in wear performance. Furthermore, the potential of the DGLAD technique has not yet been completely clarified by the lack of a study on the role of the magnitude of angular oscillation. This work aims to understand it by systematically varying the range of oscillation used during DGLAD and observing it in the changes in microstructure and wear bearing capacity of coatings of Cr-Al-N produced by HiPIMS and dcMS.

7.2. MATERIALS AND METHODS

7.2.1. DEPOSITION OF COATINGS

304 AISI stainless steel substrate were prepared metallographically prepared using abrasive SiC sandpaper with progressive grits up to # 2000 and polished using

6, 3 and 1 µm diamond suspensions and colloidal silica to achieve a mirror finish. Prior to deposition, the substrates were cleaned in ultrasonic bath with acetone and blow dried. All depositions were carried out in a HiPIMS 250 PVD chamber (PLASMA-LIITS, Campinas, Brazil). The substrates were mounted 65 mm apart from the targets. The sample holder is part of a carousel that can perform oscillatory movements rocking the sample in front of the target surface in predetermined angular range and period. This particular setup has been described in detail in previous publications and is responsible for creating the DGLAD motion (ZHANG et al., 2008; GUIMARAES et al., 2018; AVILA et al., 2019; AVILA et al., 2020). By rocking the substrate, the angle of incidence of the flux from the target (zenith) is continuously varied between the angular limits established and in a speed correspondent to the period of duration of the oscillations. Both the period of duration and the angular limits can be chosen by the operator. In this paper the period of duration of the oscillation was kept constant for all samples (30 s), and the oscillatory range was systematically varied for investigation (0, ± 5°, ± 10°, ± 15°, ± 20°).

The depositions were carried out in an atmosphere of N_2 and Ar with flow rate of 50 and 40 sccm, respectively, and pressure of 0.266 Pa at 400°C. A Pinnacle MDX (Advanced Energy, Fort Collins, USA) dc power supply was used to provide -180 V substrate bias tension. HiPIMS coatings used a TRUMPF HÜTTINGER power supply (Stuttgart, Germany) set for 900 W of average power, 500 Hz of pulse frequency and 200 µs of ton. The dcMS deposited coatings used another Pinnacle MDX power supply with 900 W of power. CrAl 30/70 at % targets with purity of 99.5% were utilized.

Prior to the deposition all samples were ion etched for 1 hour using Cr^+ ions provided by HiPIMS discharges with 600 W average power, 104 Hz of pulse frequency, 50 µs of t_{on} and -800 V to clean the substrate's surface from residual contamination and promote ionic implantation to improve adhesion between the coating and the steel. A base layer of metallic Cr was deposited before the Cr-Al-N layer in all samples with about 10% of the total thickness of the coating.

7.2.2. CHARACTERIZATION

Morphology and thickness of the coatings were assessed by means of SEM using a FEG-Inspect F-50 microscope (FEI, Eindhoven, The Netherlands). Roughness measurements and surface maps were obtained by AFM using a NanosurfFlex (Nanosurf, Liestal, Switzerland) in tapping mode.

EDS analyses were performed using a silicon drift windowless Apollo X SDD detector from EDAX (Mahwah, USA). The measurements were calibrated using a sample of Cr-Al-N of known composition as reference.

X-ray Diffraction was performed in Θ-2Θ geometry using a Panalytical MRD-XL (Panalytical, Almelo, The Netherlands) with Mo Kα radiation (0.7093 Å).

Nanoidentation tests were performed using a PB1000 mechanical tester (Nanovea, Irvine, USA) with load of 50 mN. 7 different indentations were made for each sample with a diamond Berkovich tip and mean and standard deviation were calculated. Hardness and Elastic modulus were calculated using the Oliver-Pharr relation (PHARR, 1992).

Linear reciprocating sliding wear tests were performed using the same PB1000 mechanical tester according to the ASTM G113 standard. The tests were performed at 23°C with no lubrication. Al_2O_3 spheres of 6 mm were chosen as counter-body. The normal load applied was 10 N. Mean sliding speed was 60 mm/s alternating in a reciprocating motion and to a track of 3 mm of length for 200 cycles, totalizing a sliding distance of 1200 mm.

Wear in the coatings and in the Al_2O_3 spheres surfaces were visualized using a non-contact optical profilometer. ASTM G133-05 standard was followed to calculate wear volume and wear rate 6 cross section profiles from the trench of each sample were extracted and their area were calculated to obtain a mean area of loss material, that was multiplied by the total sliding distance to determine the average wear volume.

7.3. RESULTS AND DISCUSSION

7.3.1. MORPHOLOGY, STRUCTURE AND CHEMICAL COMPOSITION

Figure 36 presents the XRD measurements for all samples produced both by dcMS and HiPIMS. Peaks from the γ-steel substrate are visible along with Cr peaks from the base layer. Besides these two materials only peaks from B1-CrN are detected regardless of the type of magnetron sputtering technique applied or of the oscillatory range of the substrate during deposition. There is no expressive change in texture related to the oscillatory range of the substrate.

The (200) is the preferential orientation for all coatings, which is expected for Cr-Al-N in conditions of high adatom mobility (PELLEG et al., 1991; AVILA et al., 2020). There is an increase in the intensity of the (220) peaks for HiPIMS depositions in

contrast with the dcMS coatings. This may be explained by the higher degree of mobility required for the formation of this plane. HiPIMS discharges provide higher ionization of the sputtered materials which are accelerated by the negative bias and collide with more energy with the substrate or the growing film. This causes heating of the later and improve conditions for diffusion, promoting the formation of less favorable planes to minimize strain energy, such as (220) (WANG et al., 2010; AVILA et al., 2019).

Figure 36 - X-ray diffraction of the dcMS and HiPIMS deposited samples at different oscillatory ranges.

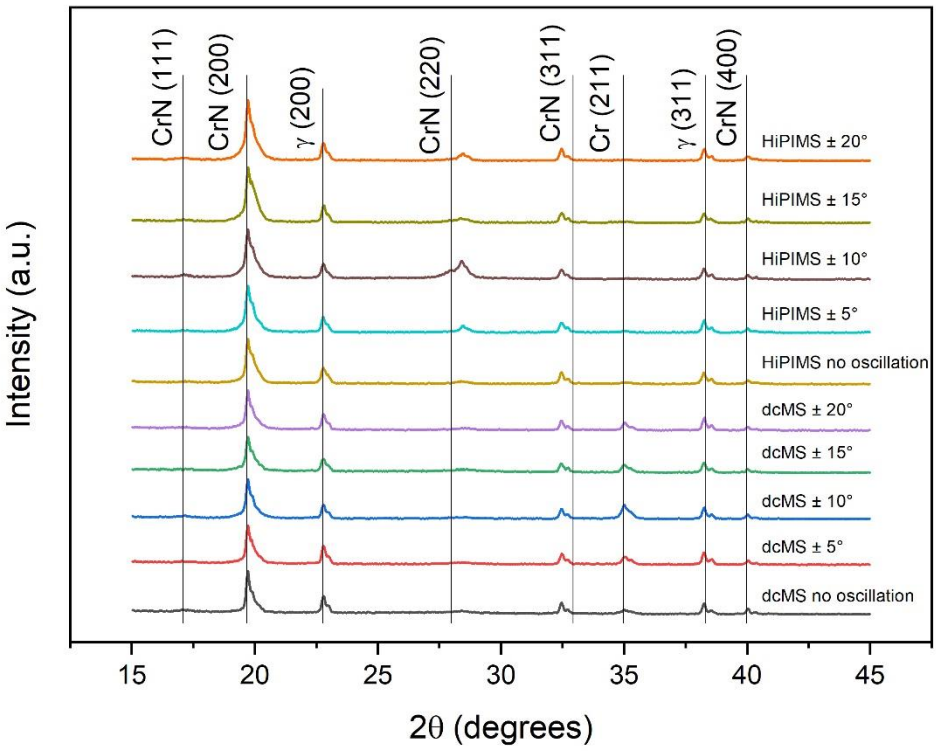

Source: The author.

Cross sectional images of the dcMS coatings are presented in Figure 37. The brighter layer corresponds to the Cr metallic base layer. The coatings present a fiber morphology with columnar grains. An increase in the thickness of the Cr-Al-N coatings from the condition of no oscillation up to ± 10° along with a gradual decrease from ± 10° to ± 20° is noticeable. Since all depositions were made using the same total time of 2 hours, these results indicates that the deposition rate is dependent of the oscillatory range in DGLAD.

Figure 37 – Cross section SEM images of dcMS produced coatings (BSE mode).

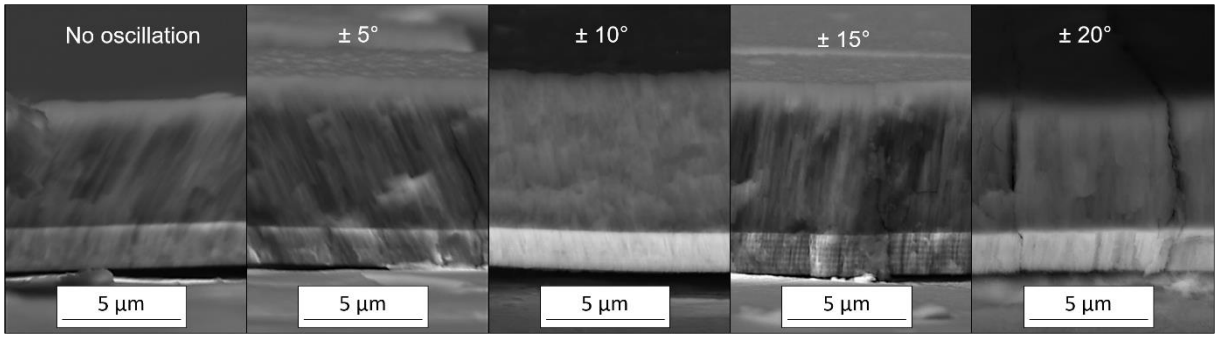

Source: The author.

The effect of the DGLAD oscillatory motion is most visible in the base layer of the ± 15° and ± 20° coatings in the form of multilayer like nanostructures or corrugated grains, as evidenced in other studies (AVILA et al., 2019; JIMENEZ et al., 2019). Figure 38 presents those structures in higher magnification. Examples of the nanostructures are highlighted in brackets and arrows. The corrugated grains are more visible in the metallic base layer due to its higher deposition rate in comparison to the Cr-Al-N ceramic film. Higher deposition rates yield thicker corrugated layers. The periodicity of the nanostructures for the base layer is around 250 nm, which is consistent with the 30 s period of oscillation used in all depositions.

Figure 38 - dcMS samples presenting the corrugated structure of the grains in details. a) ± 15° and b) ± 20°.

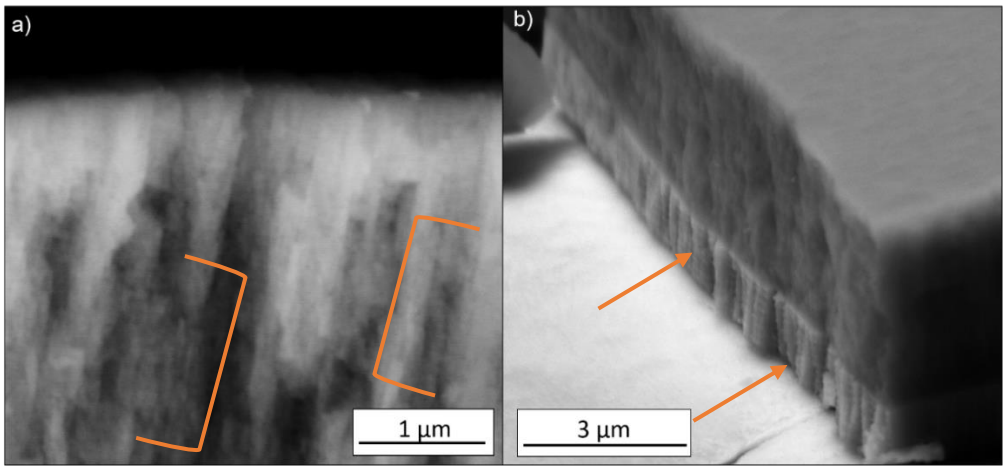

Source: The author.

The cross section view of the HiPIMS prepared samples are visible in Figure 39. In this case, the coatings presented a dense structure with almost no columns or voids, which is typical of highly energetic HiPIMS produced coatings.

Figure 39 – Cross section SEM images of the HiPIMS deposited samples (BSE mode).

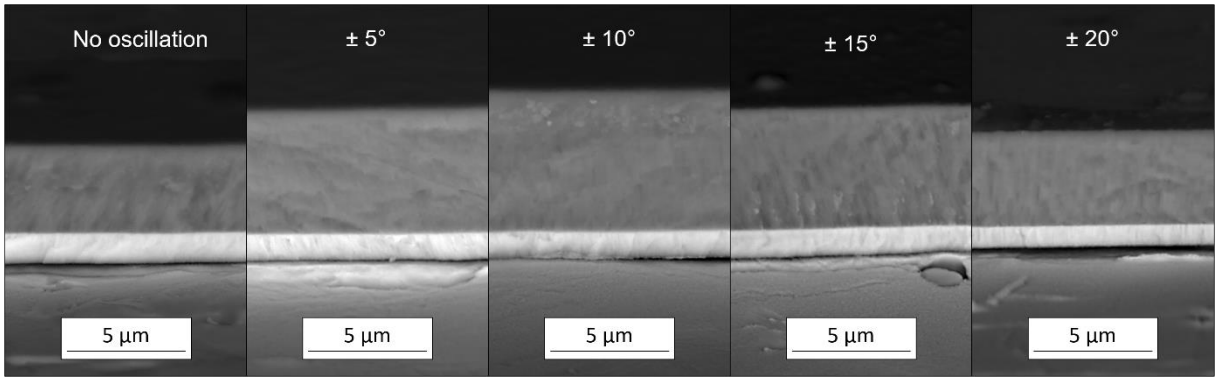

Source: The author.

As for the dcMS samples, for the HiPIMS coatings there is a dependence on coating's thickness on the oscillatory range, with thicker coatings for the condition of ± 10°, as can be seen in Figure 39. The deposition rate for the different conditions of oscillation for both dcMS and HiPIMS sample are plotted in Figure 40. An expressive deposition rate maximum at the ± 10° oscillatory range is visible, corresponding to an increase of about 1.5 times when compared to the no oscillation condition for HiPIMS depositions. Deposition rate is a fundamental aspect for coatings in industrial applications since higher deposition rate usually indicates lower costs of production (ANDERS, 2010a).

One possible explanation for the dependence of deposition rate on oscillatory range takes in consideration that: (i) the region of high density of the plasma corresponds not to a point but to an area in front of the target that is typically wider that the substrate dimensions in the shape of the so-called racetrack and (ii) sputtering is a line-of-sight process. Therefore, the rocking oscillatory motion of the substrate during DGLAD may provide better utilization of the whole sputtering cloud. This is illustrated by the progressively thicker coatings observed in Figures 37 and 39 when the oscillatory range increases from 0 to ± 10°. On the other hand, if the substrate is oscillated in a too wide range, it may possibly get out of the target's line-of-sight for a short period and cause the film to stop growing temporarily, as is the case of the ± 15° and ± 20° in Figures 37 and 39 and experience a drop in deposition rate.

Figure 40 - Deposition rate as a function of oscillatory range for HiPIMS and dcMS.

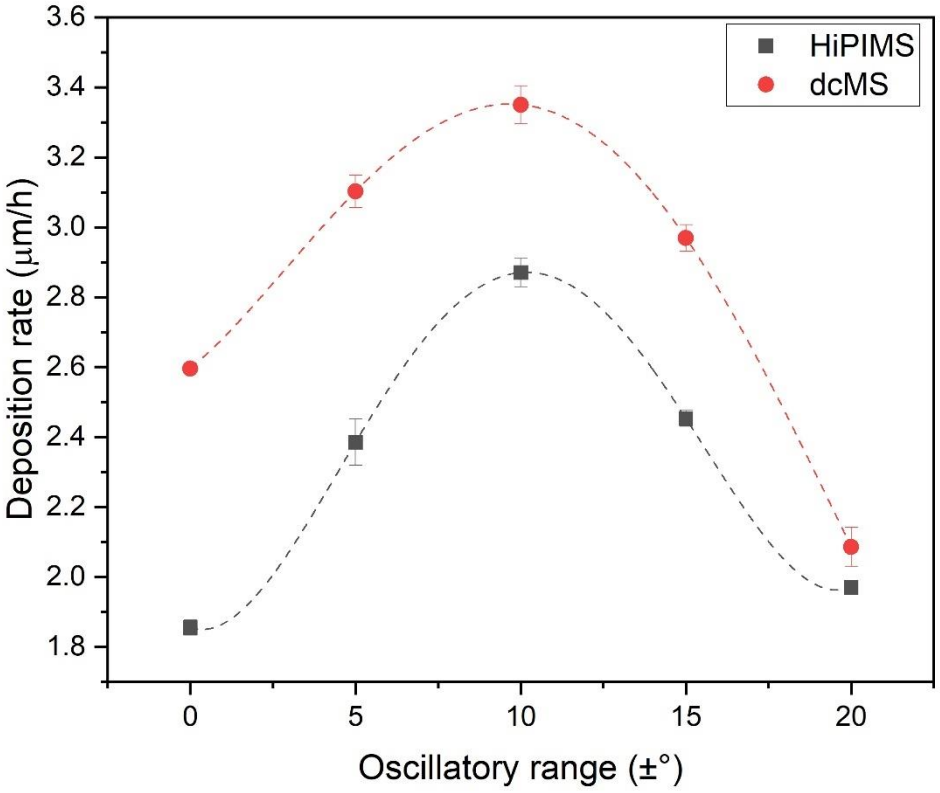

Source: The author.

The results of EDS measurements for the conditions of no oscillation, ± 10° and ± 20° for dcMS and HiPIMS samples are listed in Table 4. It is evident that the coatings presented high N content as a result of target poisoning and low sputtering yield of Al containing targets in reactive atmosphere (AVILA et al., 2020). No systematic dependence of the chemical composition with the oscillatory range can be observed.

Table 4 - EDS chemical analysis of dcMS and HiPIMS samples.

Oscillatory range (°)	Deposition technique	Cr (at%)	Al (at%)	N (at%)
No oscillation	dcMS	9.08 ± 0.45	21.05 ± 0.83	69.82 ± 5.98
± 10	dcMS	7.31 ± 0.37	23.07 ± 0.87	71.38 ± 4.99
± 20	dcMS	11.35 ± 0.35	15.72 ± 0.67	72.81 ± 4.72
No oscillation	HiPIMS	9.14 ± 0.45	20.24 ± 0.81	71.11 ± 4.81
± 10	HiPIMS	8.67 ± 0.44	20.86 ± 0.81	71.40 ± 4.95
± 20	HiPIMS	7.62 ± 0.39	22.34 ± 0.85	71.80 ± 5.05

Source: The author.

Figures 41 and 42 show the surface maps from the data collected in the tapping-AFM tests for the dcMS and HiPIMS samples, respectively. The coatings produced using direct current presented facets and an almost defect free surface, with small concentration of cone shaped growth defects (e.g., in samples ± 10° and 15°). These defects are associated with flakes and impurity particles that attach to the substrate or to the growing film surface in early stages of the deposition, most of the time originated from the chamber walls (produced during thermal expansion of the component, for instance) (BISWAS et al., 2017).

Figure 41 - Surface maps of the dcMS samples.

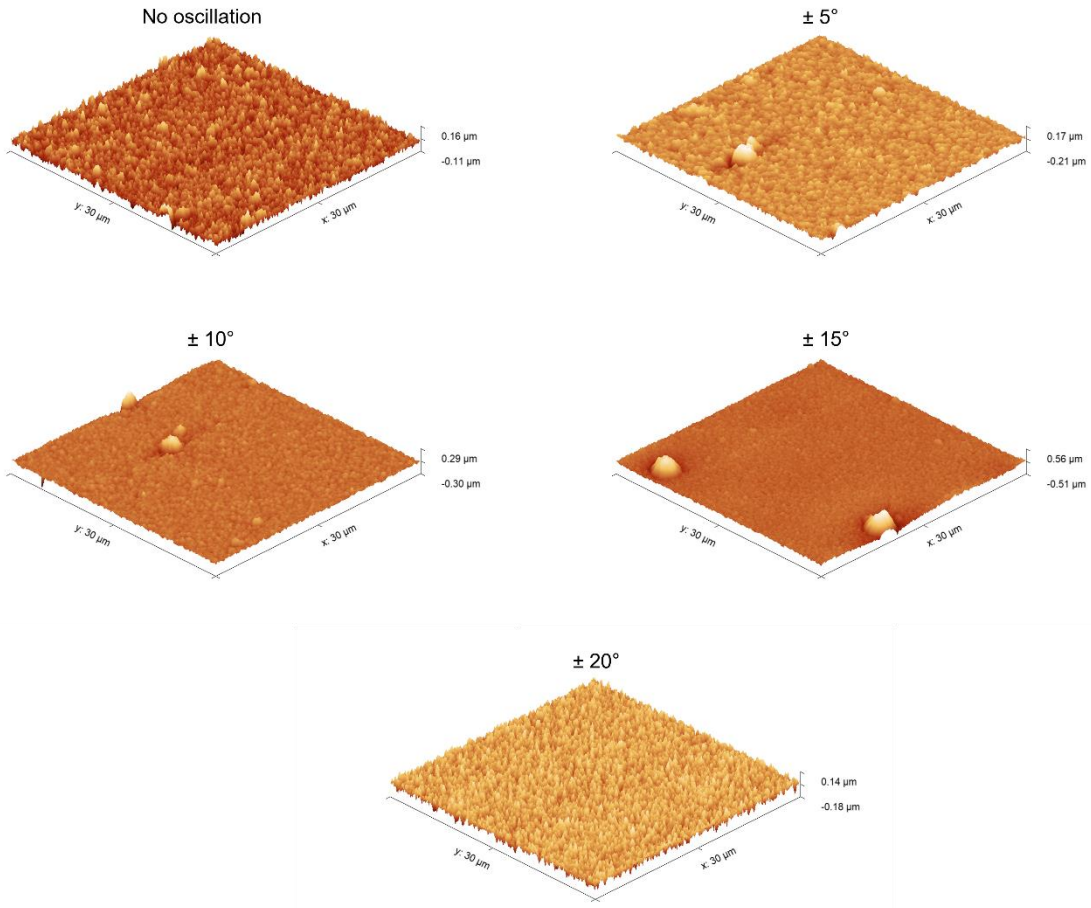

Source: The author.

Figure 42 - Surface maps of th HiPIMS samples.

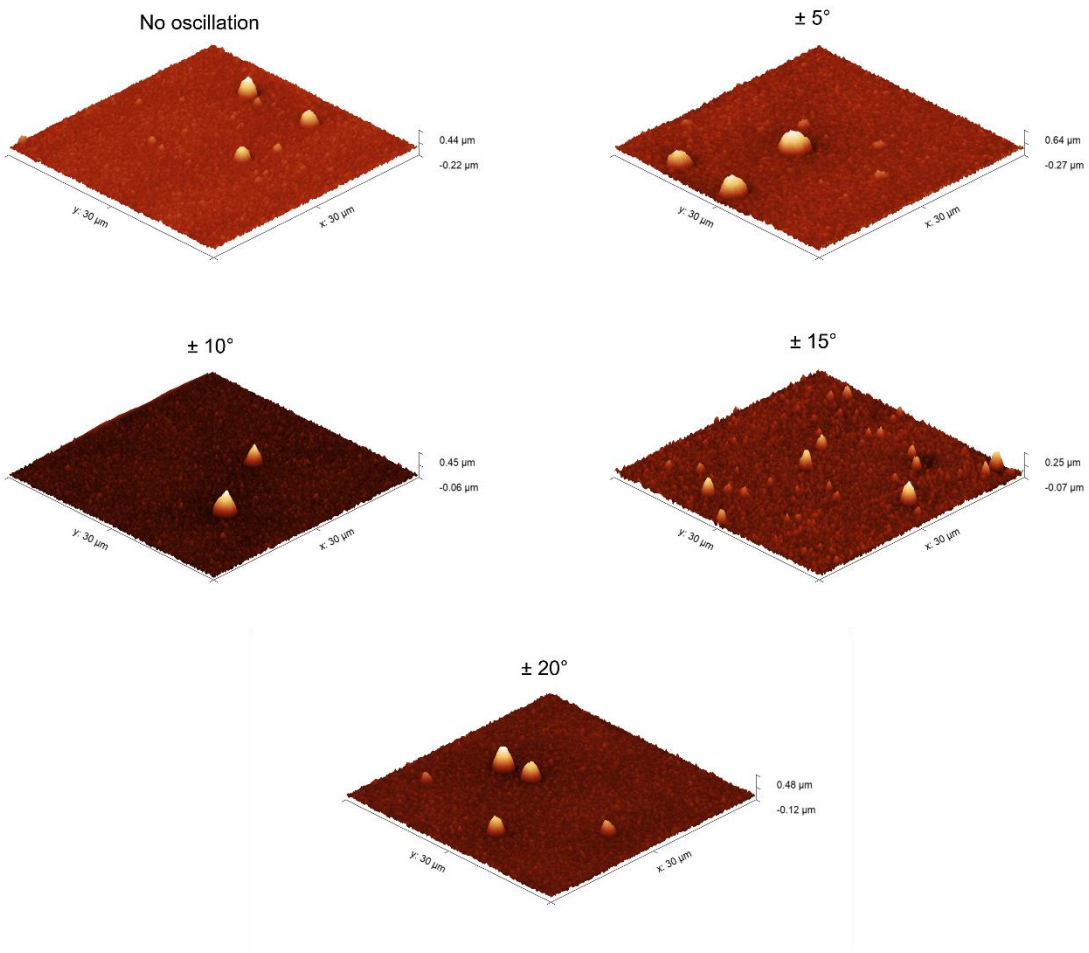

Source: The author.

These cone-shaped morphological defects are much more present in the surface of the HiPIMS coatings. One possible explanation for the difference between dcMS and HiPIMS defect concentration is the higher energy and ionization provided by the HiPIMS discharge, which may implicate in more particles detached from the chamber components (GUIMARAES et al., 2018). The values of roughness are quantified in Table 5. The mean arithmetic (Ra) as well as the root mean squared roughness (Rrms) values do not seem to vary systematic with respect to deposition type or oscillatory range. The skewness roughness (Rsk), on the other hand, is expressive higher for the HiPIMS coatings. Rsk can be interpreted as the asymmetry of the amplitude distribution function, i.e: a positive value of Rsk indicates a prevalence of peaks while a negative Rsk corresponde to a predominance of valleys in the

amplitude distribution function (HUTCHINGS; SHIPWAY, 2017). Therefore, the higher positive values of Rsk of the HiPIMS coatings are another indicative of the higher concentration of morphological defects on the surface.

Table 5 - Roughness values for coatings produced by dcMS and HiPIMS under different range of oscillatory motion of the substrate. Data is presented in terms of Mean Arithmetic Roughness (Ra), Root Mean Square Roughness (Rrms) and Skewness (Rsk).

Oscillatory range	Deposition technique	Ra	Rrms	Rsk
No oscillation	dcMS	20.98	26.55	0.27
± 5	dcMS	17.26	23.01	0.51
± 10	dcMS	14.76	20.74	1.23
± 15	dcMS	27.39	49.73	2.82
± 20	dcMS	26.62	33.36	0.11
No oscillation	HiPIMS	17.27	29.72	5.01
± 5	HiPIMS	32.64	60.41	4.73
± 10	HiPIMS	15.06	25.87	6.17
± 15	HiPIMS	13.35	20.28	3.02
± 20	HiPIMS	17.39	32.60	6.15

Source: The author.

7.3.2. MECHANICAL AND WEAR PERFORMANCE

The results of hardness measured by instrumented nanoindentation are presented in Figure 43. A dependence of hardness on the oscillatory range is visible for the HiPIMS coatings. As the DGLAD conditions are altered from no oscillation to ± 5°, hardness tends to increase. However, there is a sharp gain in hardness from ± 10° and on, with the higher condition being ± 15° (about 38 GPa). The coatings produced by dcMS presented a similar trend, however less expressive, being ± 15° the harder condition (about 25 GPa). These results are associated with the corrugated nature of the nanostructures formed by substrate oscillation since no texture or chemical composition changes are evident. In previous works from this research group and from others the zig-zag architecture of the grains formed by oblique deposition are associated with periodic variations in residual stresses and misorientation gradients (KECKES et al., 2018; AVILA et al., 2019). These features act as barriers for plastic deformation, which increase hardness. Also, a common failure mechanism for PVD coatings is through intergranular fractures that propagate along the columnar grains (REZAEI et al., 2018). Since the oscillatory motion of the substrate produces films with

corrugated grains, the propagation of intergranular cracks must follow its corrugated nature and constantly change its direction, losing an amount of energy each time (DANIEL et al., 2020). This is accentuated by larger oscillatory ranges.

Figure 43 - Hardness as a function of the oscillatory range of coatings produced using dcMS and HiPIMS.

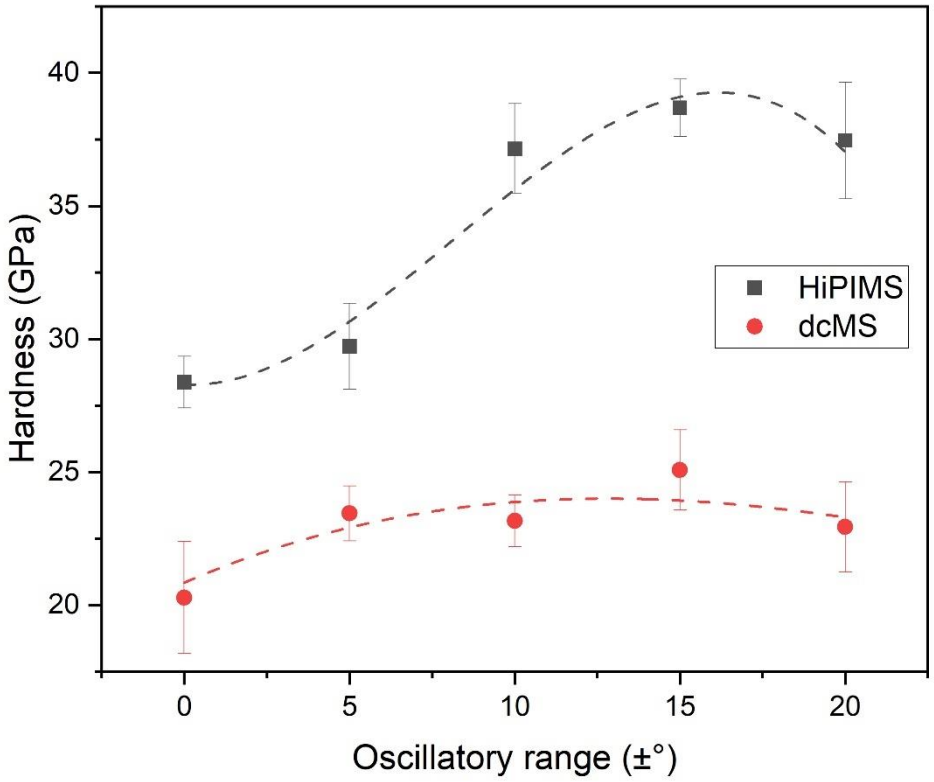

Source: The author.

Figure 44 exhibits the performance of the different dcMS coatings in the linear reciprocating test in terms of wear volume and wear rate. Both features present a decreasing trend with increasing oscillatory range from 0 up to ± 10° and star to increase for the conditions of ± 15° and ± 20°. A reduction in worn volume of about 3 times is evident from the condition of no oscillation to the condition of ± 10°.

Figure 44 - Effect of the oscillatory movement of the substrate on the volume loss and wear rate of the dcMS coatings under linear reciprocating tests.

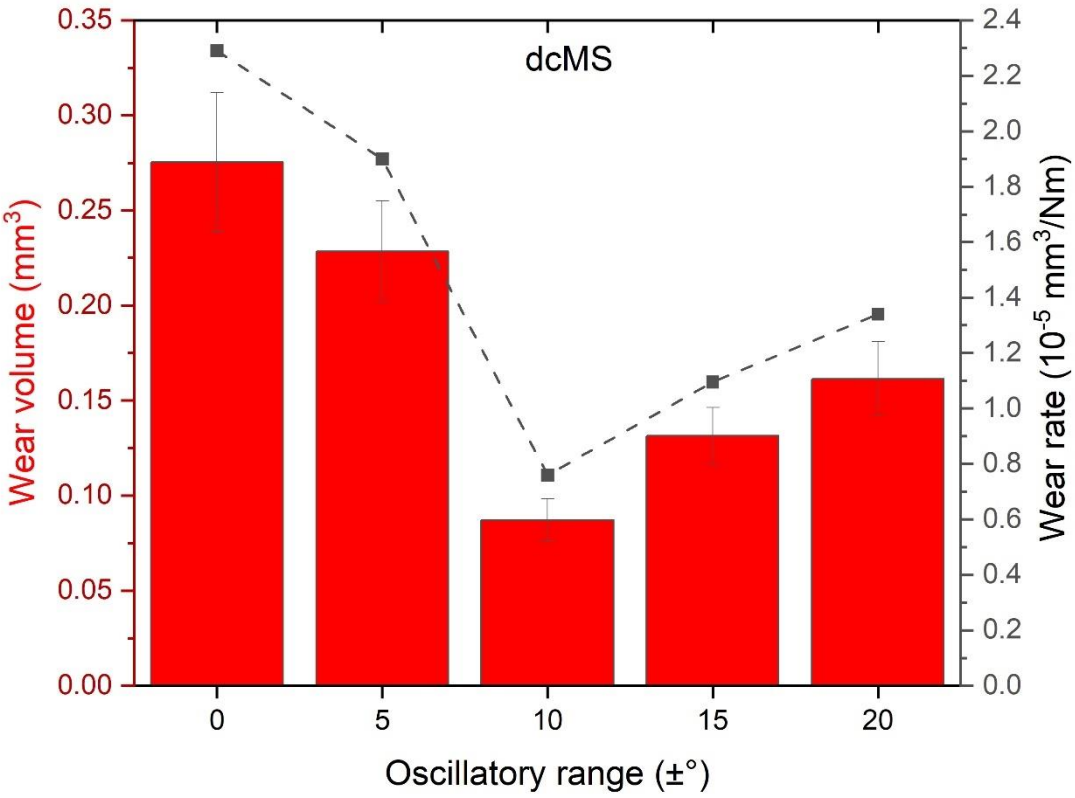

Source: The author.

The results of the HiPIMS coatings for the linear reciprocating test is presented in Figure 45. It is visible that the overall performance of the HiPIMS coating is superior in comparison with the dcMS results in Figure 44, which is expected mostly due to the higher ionization ratio and higher energy of the HiPIMS depositions, that produces highly densified and better adhered films that are more wear resistant (HSIAO et al., 2013; CHINCHANIKAR; CHOUDHURY, 2014). One can notice a decrease in wear volume and wear rate with change from no oscillation condition to ± 5° oscillation. A reduction of about 1.4 times in wear volume is registered. As the oscillatory range increases so does both wear volume and wear rate for all other deposition conditions.

Figure 45 - Effect of the oscillatory movement of the substrate on the volume loss and wear rate of the HiPIMS coatings under linear reciprocating tests.

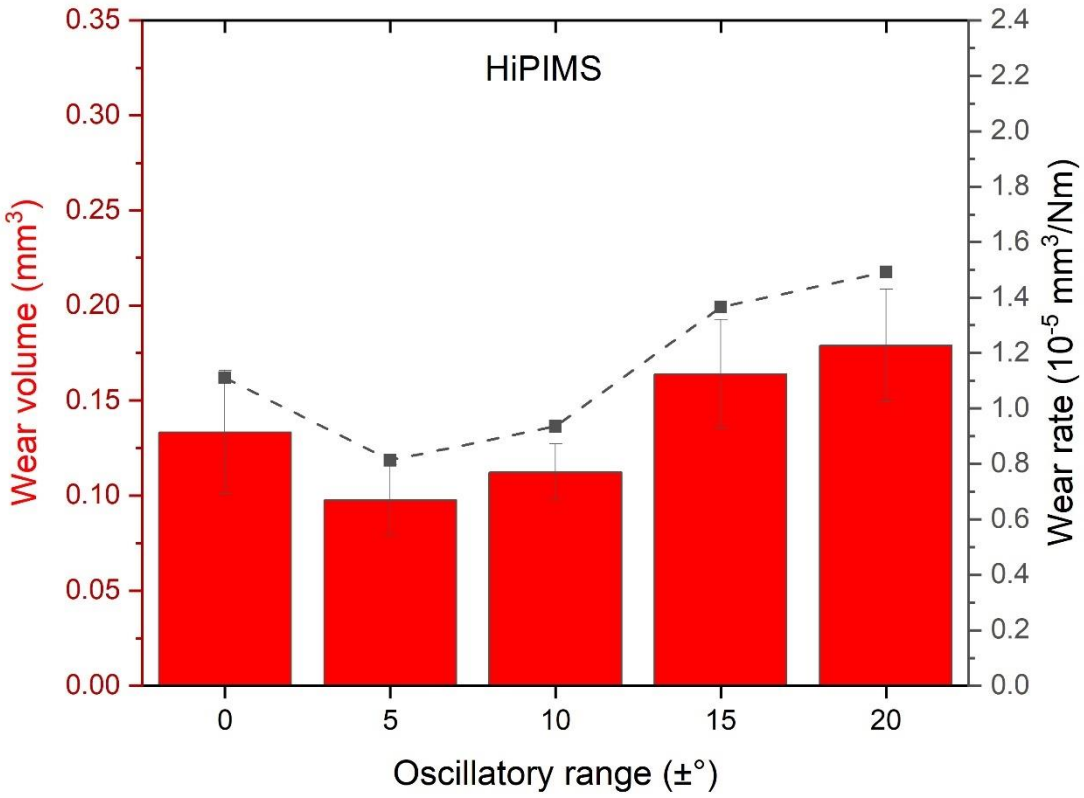

Source: The author.

Figures 46 and 47 present the wear tracks generated from the linear reciprocating wear tests as measured by optical profilometry for the dcMS and HiPIMS coatings, respectively. In Figure 46 all trenches presented pile-up of material at the edges. Also, grooves at the bottom of the tracks were visible, indicating the occurrence of abrasive wear (indicated by arrows).

Figure 46– Wear tracks produced by the Linear Reciprocating Wear test on the surface of the coatings deposited by dcMS

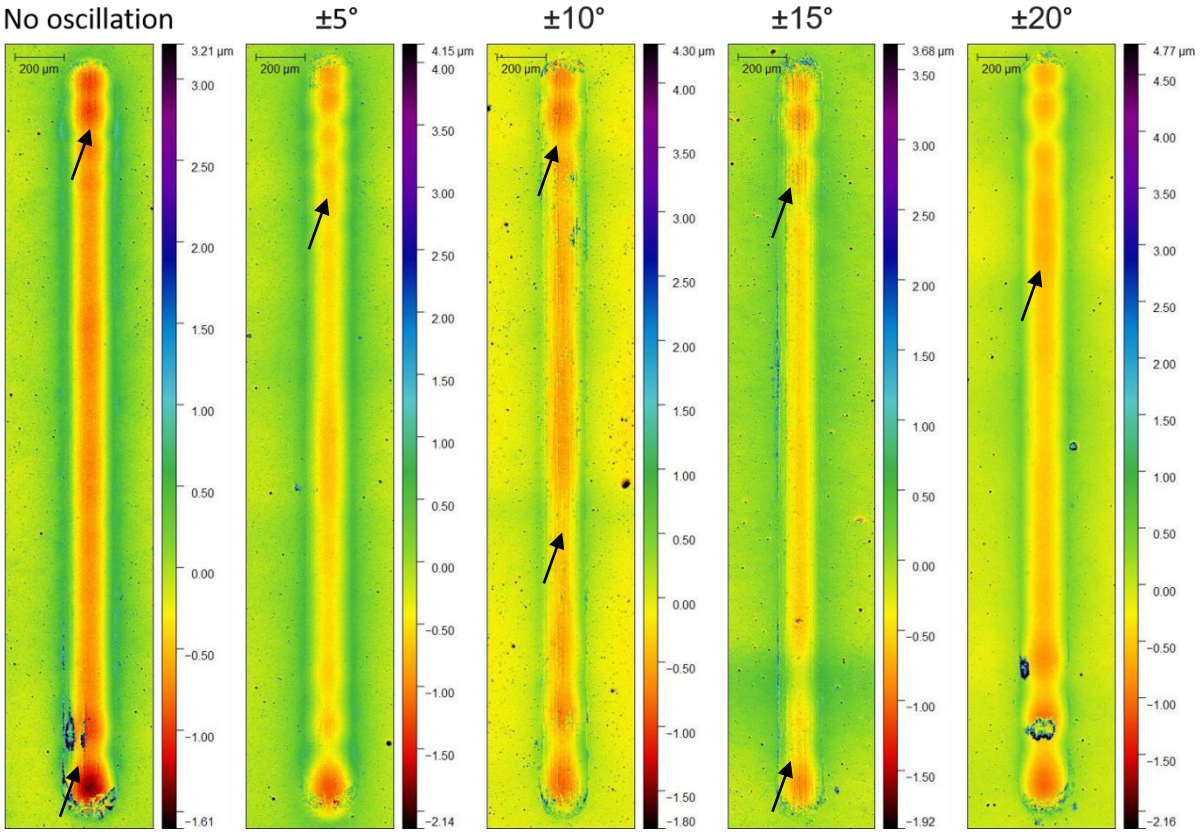

Source: The author.

In Figure 47, the wear marks on the HiPIMS coatings also presented pile-up and grooves. Qualitatively, the condition of ± 5° presented a shallower trench, which is consistent with results from Figure 45.

Figure 47 - Wear tracks produced by the Linear Reciprocating Wear test on the surface of the coatings deposited by HiPIMS.

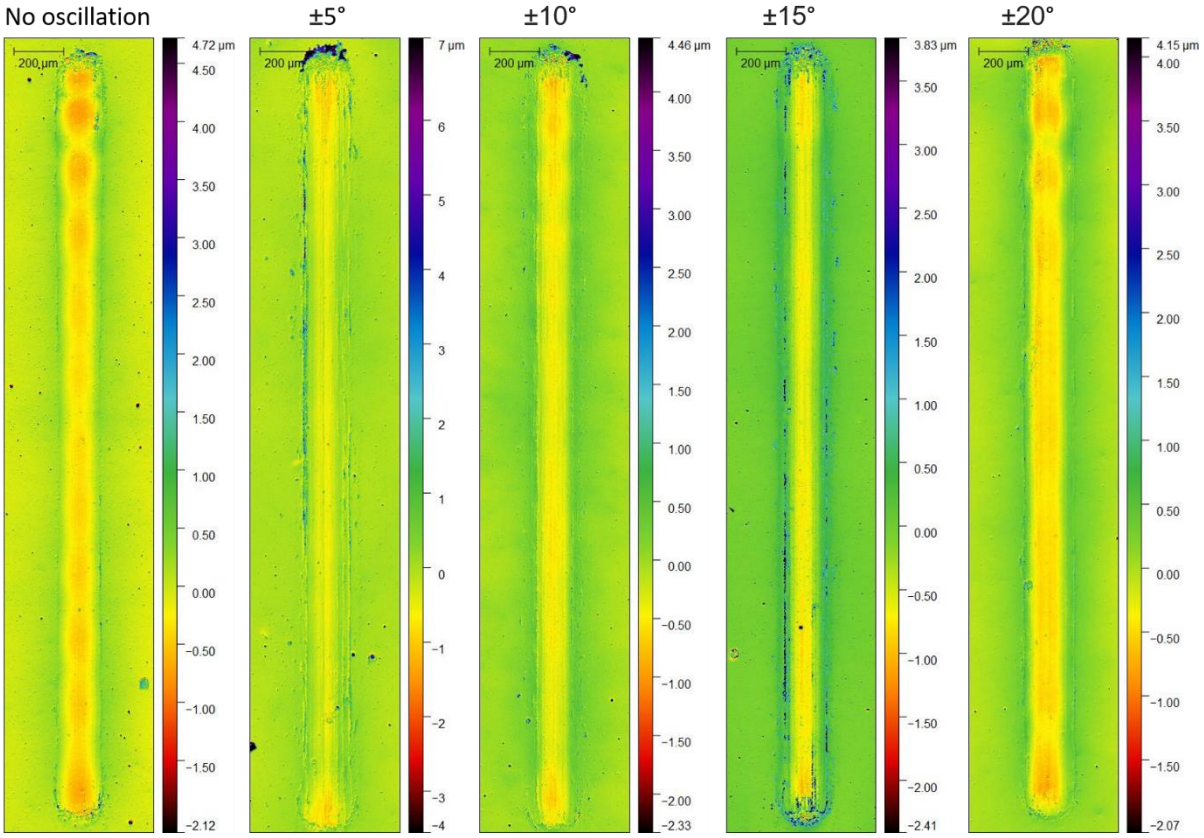

Source: The author.

The wear signals on the counter body are also relevant and can help elucidate the wear mechanisms present on the system (SHARMA et al., 2013). Figures 48 and 49 show the worn surface of the Al_2O_3 sphere surface as measured using optical profilometry after tests against dcMS and HiPIMS coatings, respectively.

The spheres used for the test of the dcMS coatings (Figure 48) presented a clear circular shape of wear marks indicating removal of a calotte of material along the tests, as expected for abrasive wear mechanisms. The worn calottes follow the trend in wear rate from Figure 44 and decrease in radius with increase of oscillatory range up to ± 10°, when they start to increase up to ± 20°.The only exceptions to this was the sphere used in the test against the coating of ± 10° and ± 15° condition, which exhibited signs of material adhered to the surface.

Figure 48 – Wear of the Al_2O_3 sphere counter body slid against the dcMS coatings. Yellow arrows indicate the adhered material.

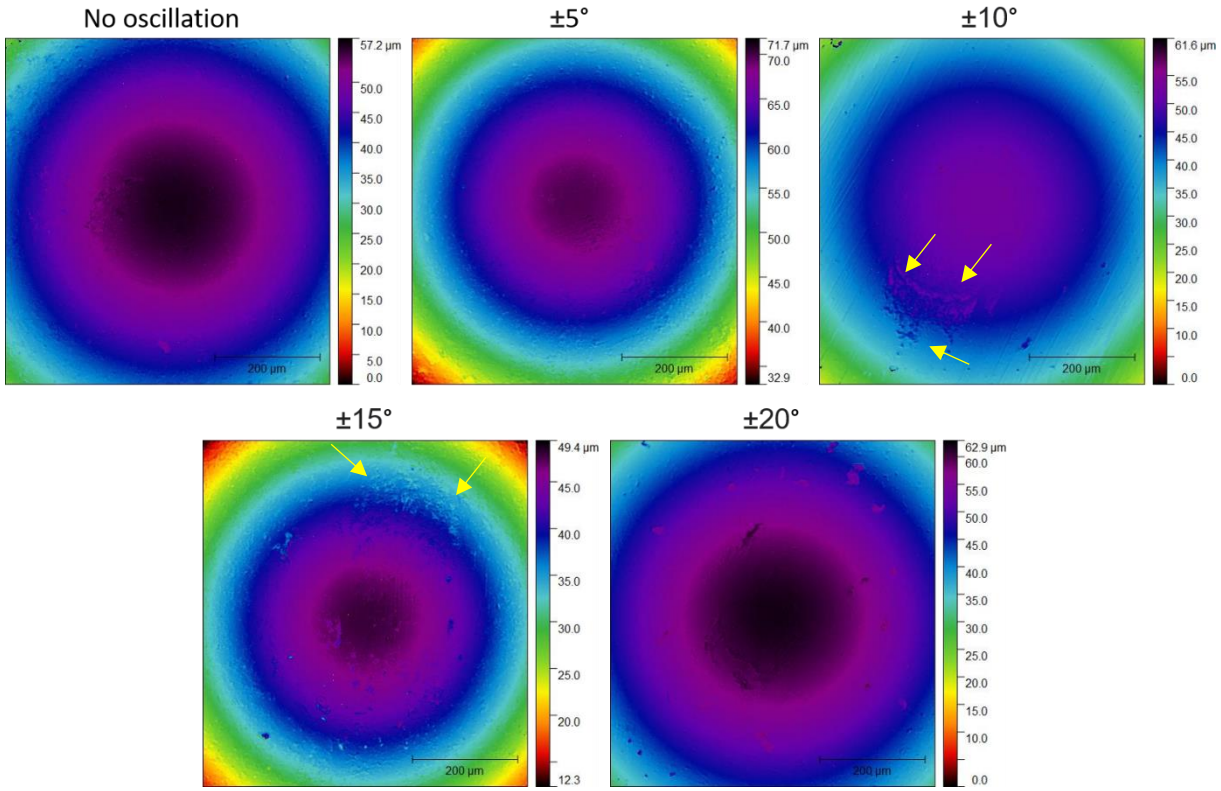

Source: The author.

The surface of the spheres tested against the HiPIMS coatings presented two different behaviors (Figure 49). The sample produced with no oscillation presented a round centralized wear calotte similar to the spheres slid against the dcMS samples (Figure 48). Differently, the coatings deposited with oscillatory ranges of ± 10°, ± 15° and ± 20° exhibited noticeable quantities of adhered material. This indicates that there is possibly a transition in the mechanism of wear from abrasion to adhesion. The condition of ± 5° presents an intermediary behavior, with the surface of the counter body showing small quantities of adhered material along with a worn calotte.

Figure 49 – Wear of the Al_2O_3 sphere counter body slid against the HiPIMS coatings.

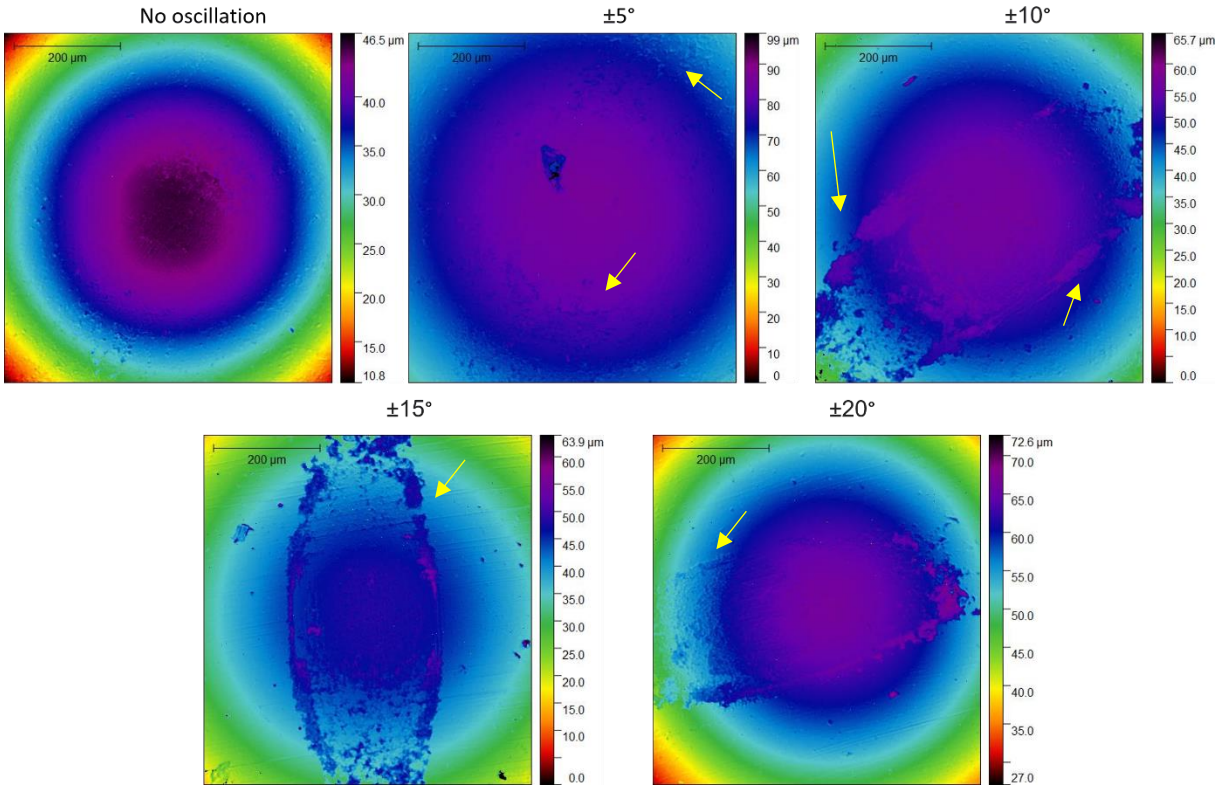

Source: The author.

Another important feature for understanding the wear phenomena of a system and that is usually measured in linear reciprocating tests is the coefficient of friction (μ). Figures 50 and 51 present the variation of μ along the test for the different dcMS and HiPIMS coatings, respectively. The variation between positive and negative values of μ indicate the changes in sliding direction.

In Figure 50 all samples presented a rapid and steep increase in μ in the first few cycles of the test. This is expected as the asperities present in the surface of the coatings and on the sphere touch each other in the Hertzian contact and cause resistance to the sliding force, causing the coefficient of friction to increase. Once the asperities are removed μ stabilizes. At the final part of the tests a slower increase is observed, typically caused by debris formed from the wear and accumulated in the trenches (LIU et al., 2012).

Figure 50 – Coefficient of friction between the Al_2O_3 sphere and the dcMS coatings for different oscillatory ranges measured continuously along the Linear Reciprocating Wear tests.

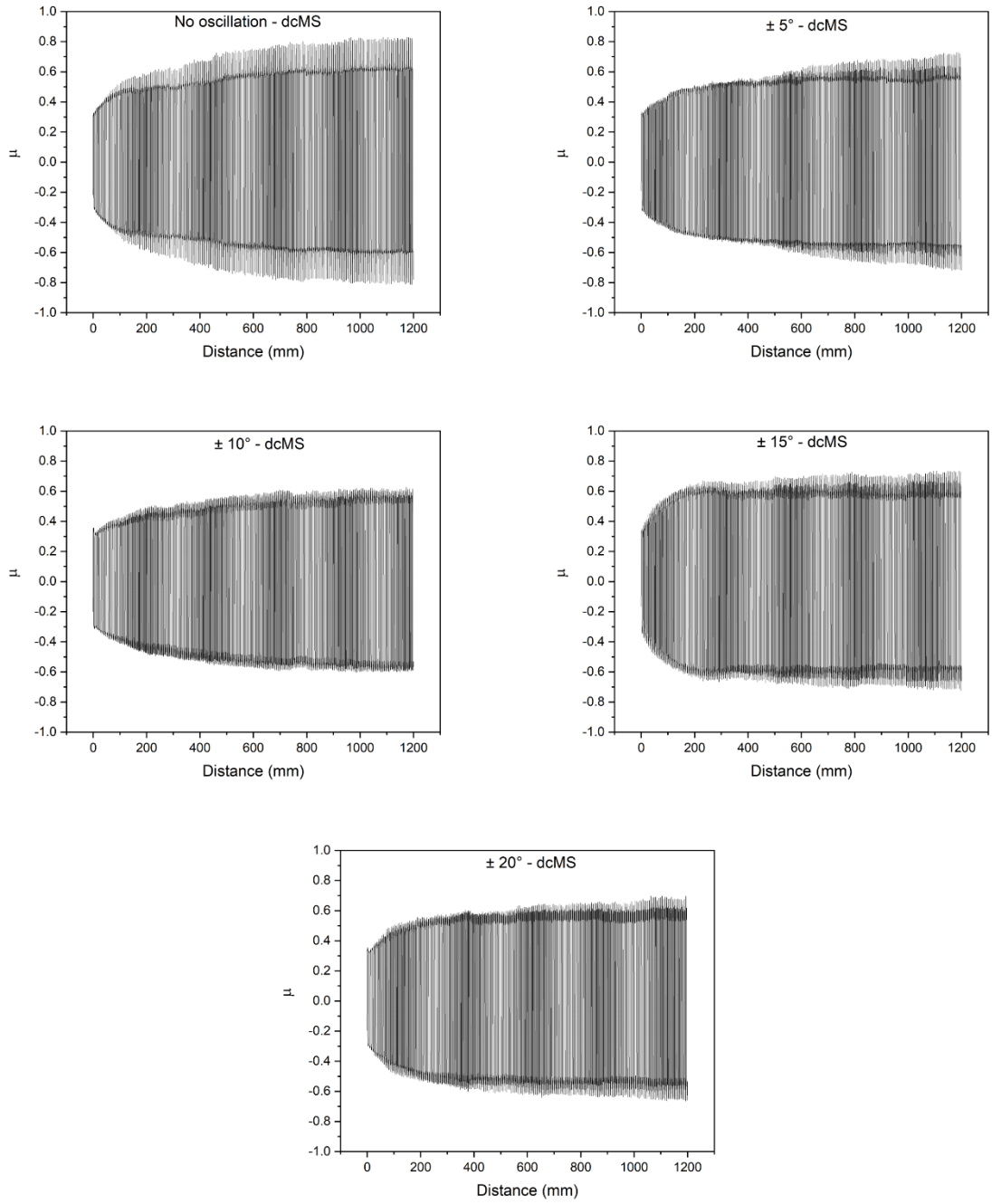

Source: The author.

The HiPIMS coatings presented two different behaviors of evolution of the coefficient of friction with sliding distance, as observed in Figure 51. The no oscillation condition presented a μ evolution similar to the ones observed and discussed for the dcMS samples, with rapid increase of μ followed by a close to constant status. The

samples produced under other conditions also exhibited an expressive scaling in μ within the initial cycles, however it was followed by a decrescent trend and stabilization in the last cycles.

A likely explanation to these two different natures of μ evolution is a difference in the wear mechanisms between the samples. In the condition of no oscillation, the mechanisms controlling wear are typically abrasive, as indicated by the wear marks on the counter body in Figure 49, and the asperities and peaks present in the system coating-sphere are worn out progressively, causing accumulation of debris in the trench. This is the mechanism expected also for the dcMS samples taking in consideration the evidence of Figures 48 and 50.

For the HiPIMS coatings produced on conditions of ± 5°, ± 10°, ± 15° and ± 20° there are indications of relevant role of adhesive wear as seen in Figure 49. In this scenario, the asperities and contacts between the coating's surface and the sphere which contribute to the generation of the friction force get adhered to the sphere surface in the first cycles, causing the resistance to the sliding and consequently the coefficient of friction to drop significantly. The subsequent sliding cycles are now performed between the Cr-Al-N coating surface and a combination of the Al_2O_3 and the coating material transferred to its surface. Since there are materials of similar hardness sliding against each other a "polishing" effect may result in stabilization of μ.

Figure 51 - Coefficient of friction between the Al_2O_3 sphere and the HiPIMS coatings for different oscillatory ranges measured continuously along the Linear Reciprocating Wear tests.

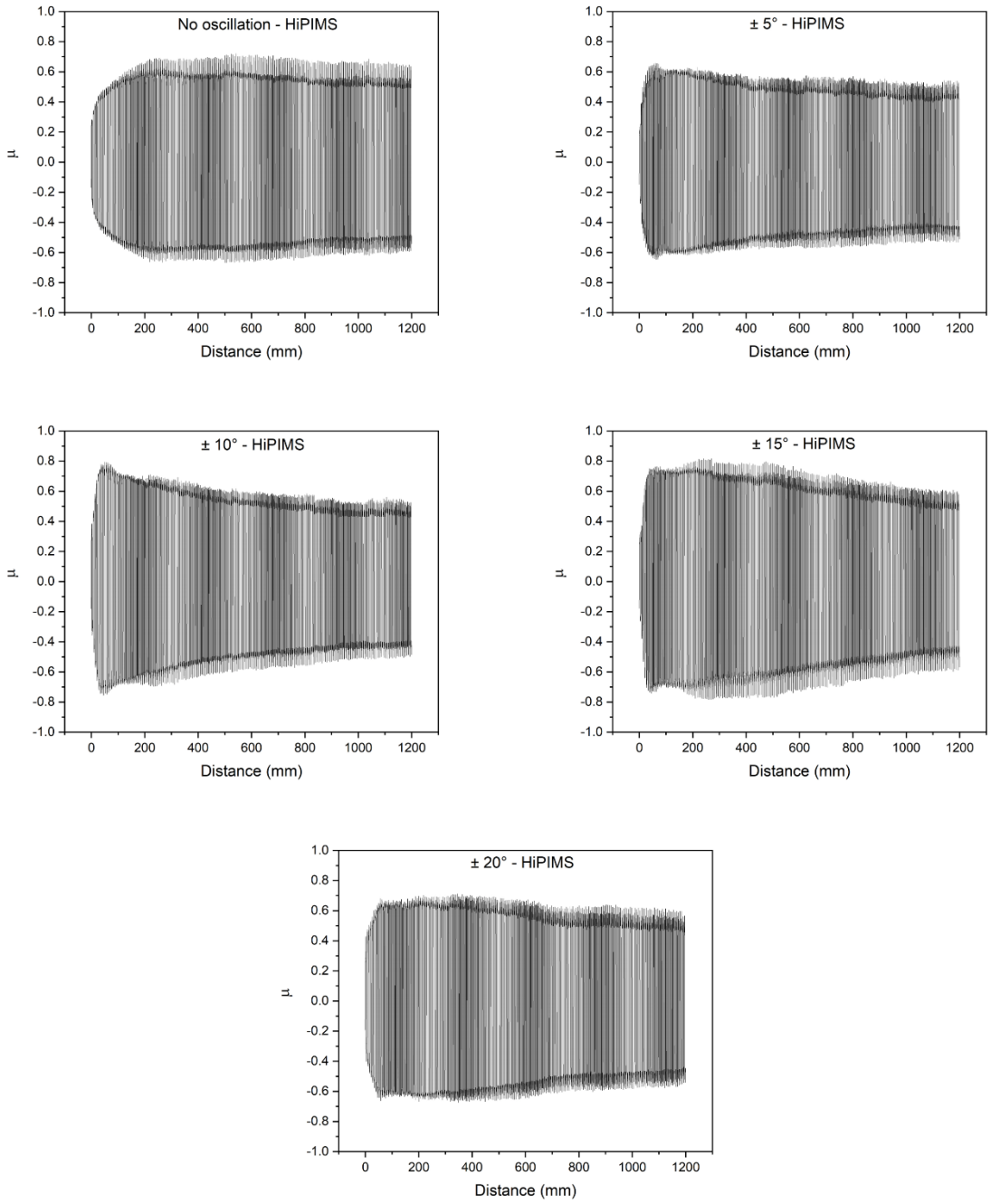

Source: The author.

The peak values of μ in both directions (μ_{max} and μ_{min}) for dcMS and HiPIMS samples under all oscillatory ranges are presented in Table 6. Since the coefficient of friction measured in linear reciprocating wear tests is a sinusoidal function with different regimes, sometimes other values besides maximum and minimum are relevant. μ_{rms}

stands for root mean square coefficient of friction and is an effective value for μ, a statistical measurement of the magnitude of its variation along the test (ŽIVIĆ et al., 2011). The values of μrms are also presented in Table 6. There is a positive relation between μ_{rms} and the wear rate for the HiPIMS and dcMS coatings (Figure 44), being a minimum of μrms correspondent to the lower wear rate (± 10° condition).

Table 6 - Coefficient of friction of the coatings produced using dcMS and HiPIMS under several oscillatory ranges.

Oscillatory range	Deposition technique	μ_{rms}	$\mu_{máx}$	$\mu_{mín}$
No oscillation	dcMS	0,572	0,831	-0,813
± 5	dcMS	0,524	0,728	-0,719
± 10	dcMS	0,495	0,626	-0,604
± 15	dcMS	0,571	0,735	-0,723
± 20	dcMS	0,519	0,698	-0,665
No oscillation	HiPIMS	0,538	0,720	-0,667
± 5	HiPIMS	0,489	0,658	-0,647
± 10	HiPIMS	0,529	0,812	-0,796
± 15	HiPIMS	0,589	0,778	-0,719
± 20	HiPIMS	0,550	0,712	-0,674

Source: The author.

The understanding of the phenomena that drive the tribological performance of PVD coatings is complex and depends on several factors such as mechanical properties of the film, surface roughness and lubrication conditions. Hardness and reduced elastic modulus (Er) are two of the relevant mechanical properties easily measurable by using nanoindentation tests and can indicate if the response of the coating will be through elastic or plastic mechanisms. The ratio H^3/Er^2 is described as the resistance to plastic deformation, being higher values of H^3/Er^2 indications of higher toughness, i.e., lower energy dissipation to permanent deformation (TSUI et al., 1995; MUSIL et al., 2002).

The values of H^3/Er^2 are plotted in Figure 52. An increase trend in resistance to plastic deformation with increase in oscillatory range is visible, especially for HiPIMS coatings as an effect of the expressive dependence of the hardness on oscillatory range. It is worth noticing that the conditions of lower wear volume and wear rate present similar H^3/Er^2 values (within the two blue dashed lines in Figure 46). That may indicate that there is an optimal value for the resistance to plastic deformation around 0.1 GPa.

Figure 52 – H^3/Er^2 as a function of the oscillatory range of coatings produced using dcMS and HiPIMS.

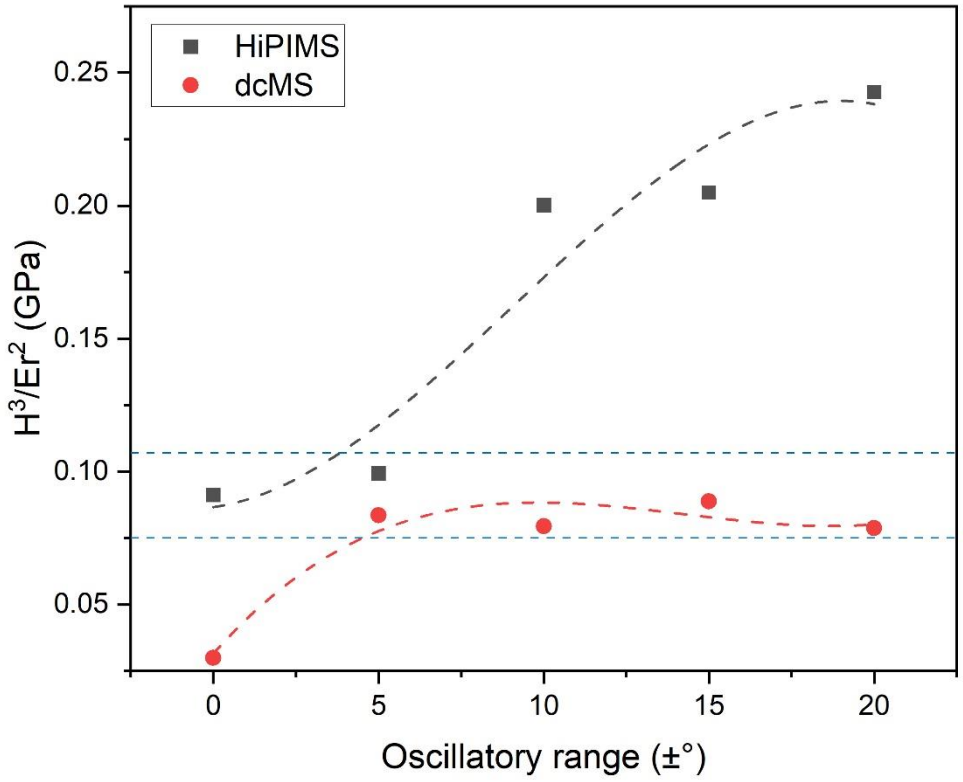

Source: The author.

This optimal range of toughness may be the cause of the change in wear nature previously discussed. In the case of low H^3/Er^2 as for the dcMS sample produced under no oscillation condition, when put in sliding contact against a counter body it can suffer brittle wear mechanisms due its low toughness. On the other side, if the coating presents very high resistance to plastic deformation it may be susceptible to other wear mechanisms, such as adhesive wear. Therefore, an intermediary condition between these two scenarios presents better tribological performance.

This intermediary condition is better visualized once the coefficient of friction is taking in consideration. Figure 53 plots H^3/Er^2 vs μ_{rms} and indicates that the coatings that performed better on wear tests present similar values of resistance to plastic deformation and effective coefficient of friction (see also Figures 44 and 45). This again is an indicative of a transition wear behavior between debris formation and condition of no adhesion to adhesion and transfer of coating material to the counter body.

Figure 53 - Classification of the coatings taking in consideration their resistance to plastic deformation and coefficient of friction. Data labeled as "H" refers to HiPIMS, while "dc" refers to dcMS. The improved conditions for wear are signalized in red.

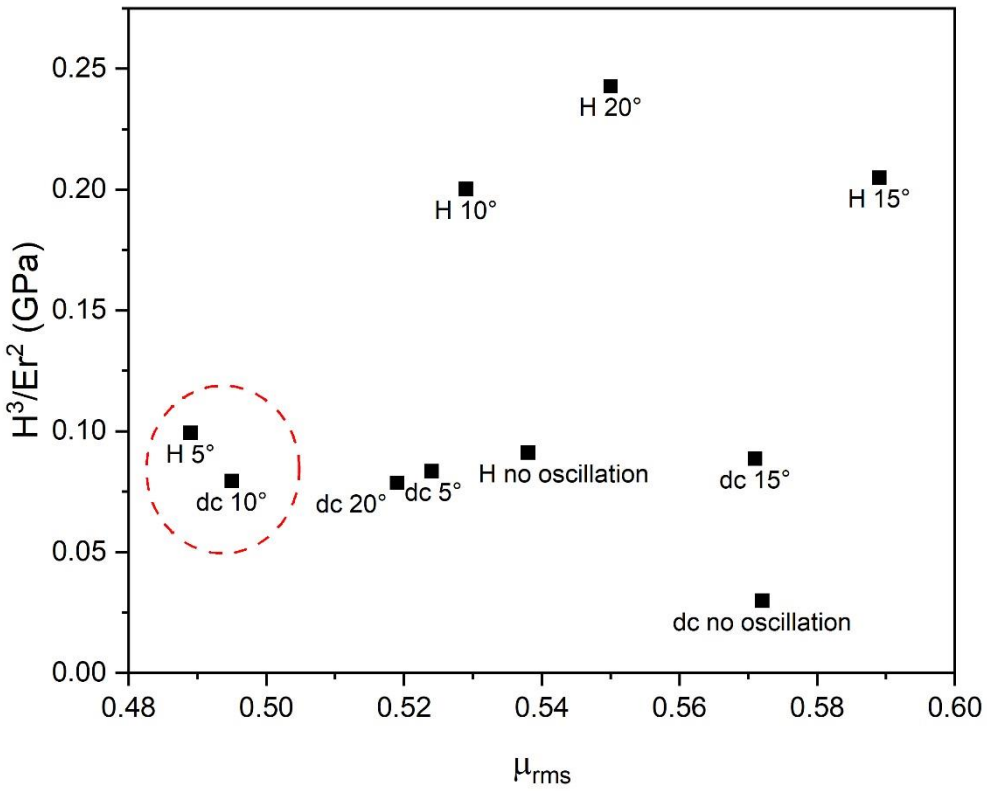

Source: The author.

7.4. CONCLUSIONS

After the production of dcMS and HiPIMS coatings under DGLAD with different oscillatory ranges (no oscillation, ± 5°, ± 10°, ± 15 ° and ± 20°) and characterization, the following conclusions can be observed:

- No systematic texture or chemical composition alteration with variations in the oscillatory range were noticed.

- Deposition rate is dependent on the oscillatory range, being ± 10° the optimal condition for both dcMS and HiPIMS.

- Significant hardness improvement from ~28 up to ~38 GPa was obtained with increase in oscillatory range for HiPIMS depositions.

- A transition from no adhesive to adhesive wear mechanisms was observed for DGLAD HiPIMS coatings with increase in oscillatory range, possibly due to larger ratios of H^3/Er^2

- ± 5° condition presented best wear performance among HiPIMS due to intermediary H^3/Er^2.

- ± 10° condition presented best wear performance among dcMS coatings due to a combination of intermediary H^3/Er^2 and lower coefficient of friction.

8. GENERAL CONCLUSIONS

Along the works presented in this thesis coatings of Cr-Al-N were successfully fabricated by reactive magnetron sputtering. HiPIMS and dcMS were utilized in the manufacture of the films with the objective of optimization of its parameters for the obtainment of hard, dense and wear protective coatings.

Regarding the deposition parameters, lower pulse frequencies in HiPIMS depositions yielded harder and thinner coatings due to more intense peaks. Cr-Al-N films produced using 70/30 precursor targets presented superior mechanical properties and indicated better wear protection. HiPIMS coatings exhibited superior hardness and wear resistance although its deposition rate decreased in comparison with dcMS produced films.

Dynamic glancing angle deposition was used to produce nanostructured coatings with corrugated zigzag grains resembling conventional multilayer architectures but with no modulation of chemical composition. The DGLAD aspects were systematically investigated. The oscillatory motion of the substrate caused continuous variation of the zenith angle, i.e., the angle of incident of the flux of sputtered material. This variation was found to be the cause of the corrugated nanostructures and also to cause misorientation step gradients inside the grains of the coatings. Nanostructures ranging from ~ 500 to ~ 10 nm of thickness were found by varying the oscillatory period during deposition.

The oscillatory range parameter was found to have major impact in DLGAD, being capable of controlling the performance and thickness of the Cr-Al-N coatings. Therefore, the use of DGLAD is indicated as a potentially important fabrication route for tailoring hardness, wear protection and deposition rate of nitride films for industrial applications.

9. SUGGESTIONS FOR FUTURE WORK

- Investigate the effect of the gas mixture ratio (N_2/Ar) in the stoichiometry of the Cr-Al-N coatings.
- Investigate the impact of the DGLAD multilayer-like structure on corrosion performance.
- Measure the in-depth residual stresses on the DGLAD manufactured coatings by means of nanodiffraction or Energy Dispersive X-Ray Diffraction in a synchrotron facility.
- Measure the in-grain misorientation gradients formed in coatings produced using different oscillatory ranges.
- Investigate the fracture toughness of the DGLAD manufactured coatings using micro-pillars indentation.
- Evaluate the wear performance of the Cr-Al-N and DGLAD prepared coatings in high temperatures.

-

REFERENCES

ABADIAS, G. Stress and preferred orientation in nitride-based PVD coatings. **Surface and coatings Technology**, v. 202, p. 2223–2235, 2008.

ABADIAS, G.; ANĞAY, F.; MAREUS, R.; MASTAIL, C. Texture and stress evolution in HfN films sputter-deposited at oblique angles. **Coatings**, v. 9, n. 2, 712, 2019.

ALTUN, H.; SEN, S. The effect of DC magnetron sputtering AlN coatings on the corrosion behaviour of magnesium alloys. **Surface and Coatings Technology**, v. 197, p. 193–200, 2005.

AMANOV, A. Surface engineering-controlled tribological behavior and adhesion strength of Ni-Cr coating sprayed onto carburized AISI 4340 steel substrate. **Surface and Coatings Technology**, v. 370, p. 144–156, 2019.

ANDERS, A. Deposition rates of high power impulse magnetron sputtering: Physics and economics. **Journal of Vacuum Science & Technology A: Vacuum, Surfaces, and Films**, 28, 783, 2010a.

ANDERS, A. A structure zone diagram including plasma-based deposition and ion etching. **Thin Solid Films**, v. 518, n. 15, p. 4087–4090, 2010b.

ANDERS, A. Tutorial : Reactive high power impulse magnetron sputtering (R-HiPIMS). **Journal of Applied Physics**, 121, 171101, 2017b.

ARIF, M.; SANGER, A.; SINGH, A. Sputter deposited chromium nitride thin electrodes for supercapacitor applications. **Materials Letters**, v.220, p. 213-217, 2018.

ASTHANA, R.; KUMAR, A.; DAHOTRE, N. **Materials Processing and Manufacturing Science**. Elsevier Scientific Pub. Co., 2006.

AVILA, P. R. T.; RODRIGUES, A. M.; GUIMARÃES, M. C. R.; et al. Nitrogen-enriched Cr1-xAlxN multilayer-like coatings manufactured by dynamic glancing angle direct current magnetron sputtering. **Materials**, v. 13, n. 16, p. 3650, 2020.

AVILA, P.R.T.; SILVA, E. P. DA; RODRIGUES, A. M.; et al. On manufacturing multilayer-like nanostructures using misorientation gradients in PVD films. **Scientific Reports**, v. 9, n. 1, p. 1-10, 2019.

BAGCIVAN, N.; BOBZIN, K.; THEISS, S. (Cr 1 − x Al x) N : A comparison of direct current , middle frequency pulsed and high power pulsed magnetron sputtering for injection molding components. **Thin Solid Films**, v. 528, p. 180–186, 2013.

BAKOGLIDIS, K. D.; SCHMIDT, S.; GRECZYNSKI, G.; HULTMAN, L. Improved adhesion of carbon nitride coatings on steel substrates using metal HiPIMS pretreatments. **Surface and Coatings Technology**, v. 302, p. 454-462, 2016.

BALOGUN, M.; HUANG, Y.; QIU, W. Updates on the development of nanostructured transition metal nitrides for electrochemical energy storage and water splitting. **Materials Today**, v. 20, p. 425-451, 2017.

BAPTISTA, A.; SILVA, F.; PORTEIRO, J.; MÍGUEZ, J.; PINTO, G. Sputtering Physical Vapour Deposition (PVD) Coatings: A Critical Review on Process Improvement and Market Trend Demands. **Coatings**, v. 8, n. 11, p. 402, 2018.

BARNA, P. B.; ADAMIK, M. Fundamental structure forming phenomena of polycrystalline films

and the structure zone models. **Thin Solid Films**, v. 317, p. 27-33, 1998.

BARNETT, S.; MADAN, A. Superhard superlattices. **Physics World**, v.11, 1998.

BARRANCO, A.; BORRAS, A.; GONZALEZ-ELIPE, AGUSTIN R.; PALMERO, A. Perspectives on oblique angle deposition of thin films: From fundamentals to devices. **Progress in Materials Science**, v. 76, p. 59-153, 2016.

BARSHILIA, H. C.; SELVAKUMAR, N.; DEEPTHI, B.; RAJAM, K. S. A comparative study of reactive direct current magnetron sputtered CrAlN and CrN coatings. **Surface and Coatings Technology**, v. 201, p. 2193-2201, 2006.

BELIARDOUH, N. E.; BOUZID, K.; NOUVEAU, C.; TLILI, B.; WALOCK, M. J. Tribology International Tribological and electrochemical performances of Cr / CrN and Cr / CrN / CrAlN multilayer coatings deposited by RF magnetron sputtering. **Tribiology International**, v. 82, p. 443–452, 2015.

BERG, S.; NYBERG, T. Fundamental understanding and modeling of reactive sputtering processes. **Thin Solid Films**, v. 476, p. 215-230, 2005.

BERG, S.; NYBERG, T.; KUBART, T. Modelling of Reactive Sputtering Processes. **Springer Series in Materials Science**, v. 109, 2008.

BISWAS, B.; PURANDARE, YASHODHAN; KHAN, I.; HOVSEPIAN, P. E. Effect of substrate bias voltage on defect generation and their influence on corrosion and tribological properties of HIPIMS deposited CrN/NbN coatings. **Surface and Coatings Technology**, v. 344, p. 383–393, 2018.

BISWAS, B.; PURANDARE, Y.; SUGUMARAN, A. A.; et al. Defect growth in multilayer chromium nitride/niobium nitride coatings produced by combined high power impulse magnetron sputtering and unbalance magnetron sputtering technique. **Thin Solid Films**, v. 636, p. 558-566, 2017.

BISWAS, B.; PURANDARE, Y.; SUGUMARAN, A.; KHAN, I.; HOVSEPIAN, P. E. Effect of chamber pressure on defect generation and their influence on corrosion and tribological properties of HIPIMS deposited CrN/NbN coatings. **Surface and Coatings Technology**, v 336, p. 84-91, 2018.

BOBZIN, K.; BRÖGELMANN, T.; KRUPPE, N. C.; et al. Fundamental study of an industrial reactive HPPMS (Cr,Al)N process. **Journal of Applied Physics**, v. 122, p. 015302, 2017.

BOBZIN, K.; LUGSCHEIDER, E.; NICKEL, R.; BAGCIVAN, N.; KRÄMER, A. Wear behavior of Cr1-xAlxN PVD-coatings in dry running conditions. **Wear**, v. 263, p. 1274-1280, 2007.

BOUSSER, E.; MARTINU, L.; KLEMBERG-SAPIEHA, J. E. Solid particle erosion mechanisms of protective coatings for aerospace applications. **Surface and Coatings Technology**, v. 257, p. 165-181, 2014.

BRÄUER, G. Magnetron Sputtering. **Comprehensive Materials Processing**, 2014.

BRÄUER, G.; SZYSZKA, B.; VERGÖHL, M.; BANDORF, R. Magnetron sputtering - Milestones of 30 years. **Vacuum**, v. 84, p. 1354-1359, 2010.

BUNSHAH, R. F. Vapor Deposition Technologies. **HANDBOOK OF HARD COATINGS Deposition Technologies , Properties and Aplications**, p. 4–72, 2001.

CABANA, J.; LING, C. D.; ORÓ-SOLÉ, J.; et al. Antifluorite-type lithium chromium oxide nitrides: Synthesis, structure, order, and electrochemical properties. **Inorganic Chemistry**, v.

43 (22), p. 7050-7060, 2004.

CHATEAUMINOIS, A. ASM Handbook: Surface Engineering (Vol 5). **Tribology International**, v. 33, n. 1, p. 67, 2000.

CHAUHAN, K. V.; RAWAL, S. K. A Review Paper on Tribological and Mechanical Properties of Ternary Nitride based Coatings. **Procedia Technology**, v. 14, p. 430-437, 2014.

CHAVDA, M. R.; DAVE, D. P.; CHAUHAN, K. V.; RAWAL, S. K. Tribological Characterization of TiN Coatings Prepared by Sputtering. **Procedia Technology**, v. 23, p. 36-41, 2016.

CHEN, F. F. **Introduction to Plasma Physics and Controlled Fusion**. Sprnger-Verlag, 2016.

CHINCHANIKAR, S.; CHOUDHURY, S. K. Hard turning using HiPIMS-coated carbide tools : Wear behavior under dry and minimum quantity lubrication (MQL). **Measurement**, v. 55, p. 536–548, 2014.

COLOMBO, D. A.; ECHEVERRÍA, M. D.; LAINO, S.; DOMMARCO, R. C.; MASSONE, J. M. Rolling contact fatigue resistance of PVD CrN and TiN coated austempered ductile iron. **Wear**, v 308, p. 35-45, 2013.

DANIEL, R.; MEINDLHUMER, M.; ZALESAK, J.; et al. Multi-scale interface design of strong and damage resistant hierarchical nanostructured materials. **Materials and Design**, v. 196, p. 109169, 2020.

DAVIS, R. F. III-V Nitrides for Electronic and Optoelectronic Applications. **Proceedings of the IEEE**, v.79, n. 5, 1991.

DELISLE, D. A.; KRZANOWSKI, J. E. Surface morphology and texture of TiAlN/CrN multilayer coatings. **Thin Solid Films**, v. 524, p. 100-106, 2012.

DING, X. Z.; ZENG, X. T. Structural, mechanical and tribological properties of CrAlN coatings deposited by reactive unbalanced magnetron sputtering. **Surface and Coatings Technology**, v. 200, p. 1372-1376, 2005.

DROZDZ, M.; KYZIOŁ, K.; GRZESIK, Z. Chromium-based oxidation-resistant coatings for the protection of engine valves in automotive vehicles. **Materiali in Tehnologije**, v. 51, n. 4, p. 603-607, 2017.

DU, J.; ZHOU, H.; SUN, C.; et al. Growth structure effect on the corrosion resistance and mechanical properties of CrNx coating . **Surface Review and Letters**, v. 1950091, p. 1950091, 2019.

EDDINE, M. N.; BERTAUT, E. F.; ROUBIN, M.; PARIS, J. Etude cristallographique de Cr 1− x V x N à basse temperature . **Acta Crystallographica Section B Structural Crystallography and Crystal Chemistry**, v. 33, n. 10, p. 3010–3013, 1977.

EHIASARIAN, A. P.; WEN, J. G.; PETROV, I. Interface microstructure engineering by high power impulse magnetron sputtering for the enhancement of adhesion. **Journal of Applied Physics**, v. 101, p. 054201, 2007.

FAN, Q. X.; ZHANG, J. J.; WU, Z. H.; et al. Influence of Al content on the microstructure and properties of the CrAlN coatings deposited by arc ion plating. **Acta Metallurgica Sinica**, v. 30, n. 12, p. 1221–1230, 2017.

FERNÁNDEZ, A. G.; PINEDA, F.; WALCZAK, M.; CABEZA, L. F. Corrosion evaluation of alumina-forming alloys in carbonate molten salt for CSP plants. **Renewable Energy**, v. 140, p. 227–233, 2019.

FERREIRA, R.; MARTINS, J.; CARVALHO, Ó.; et al. Tribological solutions for engine piston ring surfaces: an overview on the materials and manufacturing. **Materials and Manufacturing Processes**, v. 35, n. 5, p. 498-520, 2020.

GÅHLIN, R.; BROMARK, M.; HEDENQVIST, P.; HOGMARK, S.; HÅKANSSON, G. Properties of TiN and CrN coatings deposited at low temperature using reactive arc-evaporation. **Surface and Coatings Technology**, v. 76-77, p. 174-180, 1995.

GARCIA, J.; PITONAK, R.; WEISSENBACHER, R.; KÖPF, A. Production and characterization of wear resistant Ti(C,N) coatings manufactured by modified chemical vapor deposition process. **Surface and Coatings Technology**, v. 205, n. 7, p. 2322-2327, 2010.

GARZON-FONTECHA, A.; CASTILLO, H. A.; RESTREPO-PARRA, E.; LA CRUZ, W. DE. The role of the nitrogen flow rate on the transport properties of CrN thin films produced by DC magnetron sputtering. **Surface and Coatings Technology**, v.334, p. 98-104, 2018.

GASSNER, M.; REBELO DE FIGUEIREDO, M.; SCHALK, N.; et al. Energy consumption and material fluxes in hard coating deposition processes. **Surface and Coatings Technology**, v. 299, p. 49-55, 2016.

GILEWICZ, A.; CHMIELEWSKA, P.; MURZYNSKI, D.; DOBRUCHOWSKA, E.; WARCHOLINSKI, B. Corrosion resistance of CrN and CrCN/CrN coatings deposited using cathodic arc evaporation in Ringer's and Hank's solutions. **Surface and Coatings Technology**, v. 299, p. 7-14, 2016.

GRECZYNSKI, G.; JENSEN, J.; BÖHLMARK, J.; HULTMAN, L. Microstructure control of CrNx films during high power impulse magnetron sputtering. **Surface and Coatings Technology**, v. 205, n. 1, p. 118–130, 2010.

GRECZYNSKI, GRZEGORZ; JENSEN, J.; HULTMAN, L. CrNx films prepared by DC magnetron sputtering and high-power pulsed magnetron sputtering: A comparative study. IEEE Transactions on Plasma Science. **IEE Transactions on Plasma Science**, v. 38, n. 11, p. 3046-3056, 2010.

GREENE, J. E. Review Article: Tracing the recorded history of thin-film sputter deposition: From the 1800s to 2017. **Journal of Vacuum Science & Technology A: Vacuum, Surfaces, and Films**, v. 34, p. 05C204, 2017.

GUIMARAES, M. C. R.; CASTILHO, B. C. N. M. DE; NOSSA, T. DE S.; et al. On the effect of substrate oscillation on CrN coatings deposited by HiPIMS and dcMS. **Surface and Coatings Technology**, v. 340, n. November 2017, p. 112–120, 2018.

GUIMARÃES, M. C. R.; CASTILHOA, B. C. N. M. DE; CUNHA, C.; et al. On the effect of aluminum on the microstructure and mechanical properties of CrN coatings deposited by HiPIMS. **Materials Research**, v. 21, n. 3, p. 1–6, 2018.

HAWKEYE, M. M.; BRETT, M. J. Glancing angle deposition: Fabrication, properties, and applications of micro- and nanostructured thin films. **Journal of Vacuum Science & Technology A: Vacuum, Surfaces, and Films**, v. 35, p. 1317, 2007.

HAYE, E.; COLAUX, J. L.; MOSKOVKIN, P.; PIREAUX, J. J.; LUCAS, S. Wide range investigation of duty cycle and frequency effects on bipolar magnetron sputtering of chromium nitride. **Surface and Coatings Technology**, v. 350, p. 84–94, 2018.

HECIMOVIC, A.; GUDMUNDSSON, J. T. Preface to Special Topic: Reactive high power impulse magnetron sputtering. **Journal of Applied Physics**, v. 121, p. 171801, 2017.

HELMERSSON, U.; TODOROVA, S.; BARNETT, S. A.; et al. Growth of single-crystal TiN/VN

strained-layer superlattices with extremely high mechanical hardness. **Journal of Applied Physics**, v. 62, p. 481, 1987.

HOLMBERG, KENNETH, A. M. **COATINGS TRIBOLOGY Properties, Mechanisms, Techniques and Applications in Surface Engineering**. 2009.

HOLMBERG, K.; ERDEMIR, A. Influence of tribology on global energy consumption, costs and emissions. **Friction**, v. 5, p. 263-284, 2017.

HOVSEPIAN, P. E.; EHIASARIAN, A. P.; DEEMING, A.; SCHIMPF, C. Novel TiAlCN / VCN nanoscale multilayer PVD coatings deposited by the combined high-power impulse magnetron sputtering / unbalanced magnetron sputtering (HIPIMS / UBM) technology. **Vacuum**, v. 82, p. 1312–1317, 2008.

HSIAO, Y. C.; LEE, J. W.; YANG, Y. C.; LOU, B. S. Effects of duty cycle and pulse frequency on the fabrication of AlCrN thin films deposited by high power impulse magnetron sputtering. **Thin Solid Films**, v. 549, p. 281-291, 2013.

HULTMAN, L. Synthesis, Structure, and Properties of Superhard Superlattice Coatings. **Nanostructured Coatings**, p. 539-584, 2007.

HULTMAN, L.; SUNDGREN, J. -E.; MARKERT, L. C.; GREENE, J. E. Ar and excess N incorporation in epitaxial TiN films grown by reactive bias sputtering in mixed Ar/N 2 and pure N 2 discharges . **Journal of Vacuum Science & Technology A: Vacuum, Surfaces, and Films**, v. 7, n. 3, p. 1187–1193, 2002.

HUTCHINGS, I.; SHIPWAY, P. **Tribology: Friction and wear of engineering materials**. Butterworth-Heinemann, 2017.

JIMÉNEZ-PIQUÉ, E.; GONZÁLEZ-GARCÍA, L.; RICO, V. J.; GONZÁLEZ-ELIPE, A. R. Nanoindentation of nanocolumnar TiO2 thin films with single and stacked zig-zag layers. **Thin Solid Films**, v. 550, p. 444-449, 2014.

JIMENEZ, M. J. M.; ANTUNES, V.; CUCATTI, S.; et al. Physical and micro-nano-structure properties of chromium nitride coating deposited by RF sputtering using dynamic glancing angle deposition. **Surface and Coatings Technology**, v. 372, p. 268-277, 2019.

JIMENEZ, M. J. M.; ANTUNES, V. G.; ZAGONEL, L. F.; et al. Effect of the period of the substrate oscillation in the dynamic glancing angle deposition technique: A columnar periodic nanostructure formation. **Surface and Coatings Technology**, v. 383, p. 125237, 2020.

JONES, ANTHONY C., M. L. H. **Chemical vapour deposition: precursors, processes and applications**. Royal Society of Chemistry, 2009.

JONES, M. H.; SCOTT, D. (DOUGLAS). **Industrial tribology : the practical aspects of friction, lubrication, and wear**. Elsevier Scientific Pub. Co., 1983.

KASMI, A. EL; TIAN, Z. Y.; VIEKER, H.; BEYER, A.; CHAFIK, T. Innovative CVD synthesis of Cu 2 O catalysts for CO oxidation. **Applied Catalysis B: Environmental**, v. 186, p. 10-18, 2016.

KECKES, J.; DANIEL, R.; TODT, J.; et al. 30 nm X-ray focusing correlates oscillatory stress, texture and structural defect gradients across multilayered TiN-SiOx thin film. **Acta Materialia**, v.144, p. 862-873, 2018.

KELLY, P. J.; ARNELL, R. D. Magnetron sputtering: A review of recent developments and applications. **Vacuum**, v. 56, n. 3, p. 159-172, 2000.

KHOJIER, K.; SAVALONI, H.; ZOLGHADR, S.; AMANI, E. Study of Electrical, Mechanical, and Tribological Properties of CrNx Thin Films as a Function of Sputtering Conditions. **Journal of Materials Engineering and Performance**, v. 23, n. 10, p. 3444–3448, 2014.

KIM, G. S.; LEE, S. Y. Microstructure and mechanical properties of AlCrN films deposited by CFUBMS. **Surface and Coatings Technology**, v. 201, p. 4361–4366, 2006.

KIM, M. W.; KIM, K. H.; KANG, M. C.; CHO, S. H.; RYU, K. T. Mechanical properties and cutting performance of Cr-Al-N hybrid coated micro-tool for micro high-speed machining of flexible fine die. **Current Applied Physics**, v. 12, n. 2, p. S14-S18, 2012.

KIM, Y. J.; BYUN, T. J.; HAN, J. G. Bilayer period dependence of CrN/CrAlN nanoscale multilayer thin films. **Superlattices and Microstructures**, v. 45, n. 2, p. 73-79, 2009.

KIMURA, A.; KAWATE, M.; HASEGAWA, H.; SUZUKI, T. Anisotropic lattice expansion and shrinkage of hexagonal TiAlN and CrAlN films. **Surface and Coatings Technology**, v. 168-170, p. 367-370, 2003.

KONDO, A.; OOGAMI, T.; SATO, K.; TANAKA, Y. Structure and properties of cathodic arc ion plated CrN coatings for copper machining cutting tools. **Surface and Coatings Technology**, v. 177-178, p. 238-244, 2004.

KOUZNETSOV, V.; MACÁK, K.; SCHNEIDER, J. M.; HELMERSSON, U.; PETROV, I. A novel pulsed magnetron sputter technique utilizing very high target power densities. **Surface and Coatings Technology**, v. 122, n. 2–3, p. 290–293, 1999.

LAEGREID, N.; WEHNER, G. K. Sputtering yields of metals for Ar+ and Ne+ ions with energies from 50 to 600 ev. **Journal of Applied Physics**, v. 32, n. 3, p. 365–369, 1961.

LANGFORD, J. I.; WILSON, A. J. C. Scherrer after sixty years: A survey and some new results in the determination of crystallite size. **Journal of Applied Crystallography**, v. 11, n. 2, p. 102–113, 1978.

LEONTYEV, V.; WAKEFIELD, N. G.; TABUNSHCHYK, K.; et al. Selective transmittance of linearly polarized light in thin films rationally designed by FDTD and FDFD theories and fabricated by glancing angle deposition. **Journal of Applied Physics**, v. 104, p. 104302, 2008.

LEYLAND, A.; MATTHEWS, A. On the significance of the H/E ratio in wear control: A nanocomposite coating approach to optimised tribological behaviour. **Wear**, v. 246, n. 1–2, p. 1–11, 2000.

LI, H.; ZHANG, C.; LIU, C.; HUANG, M. Improvement in corrosion resistance of CrN coatings. **Surface and Coatings Technology**, v. 365, n. 393, p. 158–163, 2019.

LI, Z.; MUNROE, P.; JIANG, Z. T.; et al. Designing superhard, self-toughening CrAlN coatings through grain boundary engineering. **Acta Materialia**, v. 60, n. 16, p. 5735-5744, 2012.

LIN, J.; MOORE, J. J.; MISHRA, B.; et al. Effect of asynchronous pulsing parameters on the structure and properties of CrAlN films deposited by pulsed closed field unbalanced magnetron sputtering (P-CFUBMS). **Surface and Coatings Technology**, v. 202, n. 8, p. 1418–1436, 2008.

LIN, J.; MOORE, J. J.; MOERBE, W. C.; et al. Int . Journal of Refractory Metals & Hard Materials Structure and properties of selected (Cr – Al – N , TiC – C , Cr – B – N) nanostructured tribological coatings. **International Journal of Refractory Metals and Hard Materials**, v. 28, n. 1, p. 2–14, 2010.

LIN, J.; WEI, R. A comparative study of thick TiSiCN nanocomposite coatings deposited by

dcMS and HiPIMS with and without PEMS assistance. **Surface and Coatings Technology**, v. 338, p. 84-95, 2018.

LINTYMER, J.; MARTIN, N.; CHAPPÉ, J. M.; TAKADOUM, J.; DELOBELLE, P. Modeling of Young's modulus, hardness and stiffness of chromium zigzag multilayers sputter deposited. **Thin Solid Films**, v. 503, n. 1-2, p. 177-189, 2006.

LIU, A.; DENG, J.; CUI, H.; CHEN, Y.; ZHAO, J. Friction and wear properties of TiN, TiAlN, AlTiN and CrAlN PVD nitride coatings. **International Journal of Refractory Metals and Hard Materials**, v. 31, p. 82–88, 2012.

LU, L.; LUO, F.; HUANG, Z.; ZHOU, W.; ZHU, D. Influence of the nitrogen flow rate on the infrared emissivity of TiNx films. **Infrared Physics and Technology**, v. 88, p. 144-188, 2018.

MA, Q.; LI, L.; XU, YE; et al. Effect of bias voltage on TiAlSiN nanocomposite coatings deposited by HiPIMS. **Applied Surface Science**, v. 392, p. 826-833, 2017.

MANSOUR, M.; KEITA, A. S.; GALLAS, B.; et al. Optical anisotropy of tilted columns thin films of chromium deposited at oblique incidence. **Optical Materials**, v. 32, n. 9, p. 1146-1153, 2010.

MARTIN, P. M. **Deposition technologies for films and coatings**. 2005.

MATTOX, D. M. **Handbook of Physical Vapor Deposition (PVD) Processing**. 2007.

MEZGER, P. R.; CREUGERS, N. H. J. Titanium nitride coatings in clinical dentistry. **Journal of Dentistry**, v. 20, n. 6, p. 342-344, 1992.

MOVCHAN, B. A.; DEMICHISHIN, A. V. Study of the Structure and Properties of Thick Vacuum Condensates of Nickel, Titanium, Tungsten, Aluminum Oxide and Zirconium Dioxide. **Fiz Metallov I Metalloved**, v. 28, p. 83, 1969.

MUKHERJEE, S.; GALL, D. Structure zone model for extreme shadowing conditions. **Thin Solid Films**, v. 527, p. 158–163, 2013.

MÜNZ, W. D.; SCHENKEL, M.; KUNKEL, S.; PAULITSCH, J.; BEWILOGUA, K. Industrial applications of HIPIMS. **Journal of Physics: Conference Series**, v. 100, p. 082001, 2008.

MUSIL, J.; KUNC, F.; ZEMAN, H.; POLÁKOVÁ, H. Relationships between hardness, Young's modulus and elastic recovery in hard nanocomposite coatings. **Surface and Coatings Technology**, v. 154, n. 2-3, p. 304-313, 2002.

NAVINŠEK, B.; PANJAN, P.; MILOŠEV, I. Industrial applications of CrN (PVD) coatings, deposited at high and low temperatures. **Surface and Coatings Technology**, v. 97, n. 1-3, p. 182-191, 1997.

NEDFORS, N.; MOCKUTE, A.; PALISAITIS, J.; et al. Influence of pulse frequency and bias on microstructure and mechanical properties of TiB2 coatings deposited by high power impulse magnetron sputtering. **Surface and Coatings Technology**, v. 304, p. 203–210, 2016.

NOYAN, I. C.; COHEN, J. B. M.; COHEN, J. B. M. SPECIALIST; COHEN, J. B. S. EN SCIENCE DES MATÉRIAUX. **Residual stress : measurement by diffraction and interpretation**. Springer-Verlag, 1987.

OHRING, M. **The Materials Science of Thin Films**. Academic Press, 2013.

ONO, T.; KENMOTSU, T.; MURAMOTO, T. **Simulation of the Sputtering Process**. Springer-Verlag, 2008.

PAIVA, J. M.; SHALABY, M. A. M.; CHOWDHURY, M.; et al. Tribological and wear performance of carbide tools with TiB 2 PVD coating under varying machining conditions of TiAl6V4 aerospace alloy. **Coatings**, v. 7 (11), p. 187, 2017.

PELLEG, J.; ZEVIN, L. Z.; LUNGO, S.; CROITORU, N. Reactive-sputter-deposited TiN films on glass substrates. **Thin Solid Films**, v. 197, n. 1-2, p. 117-128, 1991.

PENILLA, E.; WANG, J. Pressure and Temperature Effects on Stoichiometry and Microstructure of Nitrogen-Rich TiN Thin Films Synthesized via Reactive Magnetron DC-Sputtering. **Journal of Nanomaterials**, v. 2008, 2008.

PETFORD-LONG, A. K.; CHIARAMONTI, A. N. Transmission Electron Microscopy of Multilayer Thin Films. **Annual Review of Materials Research**, v. 38, p. 559-584, 2008.

PETROV, I.; BARNA, P. B.; HULTMAN, L.; GREENE, J. E. Microstructural evolution during film growth. **Journal of Vacuum Science & Technology A: Vacuum, Surfaces, and Films**, v. 21, p. S117-S128, 2003.

PHARR, G. M. An improved technique for determining hardness and elastic modulus using load and displacement sensing indentation experiments. **Journal of Materials Research**, v. 7, n. 6, p. 1564–1583, 1992.

PULUGURTHA, S. R.; BHAT, D. G. A study of AC reactive magnetron sputtering technique for the deposition of compositionally graded coating in the Cr-Al-N system. **Surface and Coatings Technology**, v. 201, n. 7, p. 4411-4418, 2006.

REITER, A. E.; DERFLINGER, V. H.; HANSELMANN, B.; BACHMANN, T.; SARTORY, B. Investigation of the properties of Al1-xCrxN coatings prepared by cathodic arc evaporation. **Surface and Coatings Technology**, v. 200, n. 7, p. 2114-2122, 2005.

REZAEI, S.; ARGHAVANI, M.; WULFINGHOFF, S.; et al. A novel approach for the prediction of deformation and fracture in hard coatings: Comparison of numerical modeling and nanoindentation tests. **Mechanics of Materials**, v. 117, p. 192-201, 2018.

RISTOLAINEN, E. O.; MOLARIUS, J. M.; KORHONEN, A. S.; LINDROOS, V. K. A study of nitrogen-rich titanium and zirconium nitride films. **Journal of Vacuum Science & Technology A: Vacuum, Surfaces, and Films**, v. 5, n. 4, p. 2184–2189, 2002.

ROBBIE, K. Advanced techniques for glancing angle deposition. **Journal of Vacuum Science & Technology B: Microelectronics and Nanometer Structures**, v. 16, n. 6, p. 1115-1122 1998.

ROBBIE, K.; BRETT, M. J. Sculptured thin films and glancing angle deposition : Growth mechanics and applications. **Journal of Vacuum Science & Technology A: Vacuum, Surfaces, and Films**, v. 15, n. 3, p. 1460-1465, 1997.

ROJAS, T. C.; DOMÍNGUEZ-MEISTER, S.; BRIZUELA, M.; SÁNCHEZ-LÓPEZ, J. C. Influence of Al and Y content on the oxidation resistance of CrAlYN protective coatings for high temperature applications: New insights about the Y role. **Journal of Alloys and Compounds**, v. 773, p. 1172-1181, 2019.

RUPPI, S. Deposition, microstructure and properties of texture-controlled CVD α-Al2O3 coatings. **International Journal of Refractory Metals and Hard Materials**, v.23, n. 4-6, p. 306-316, 2005.

RYDOSZ, A.; DYNDAŁ, K.; ANDRYSIEWICZ, W.; GROCHALA, D.; MARSZAŁEK, K. GLAD magnetron sputtered ultra-thin copper oxide films for gas-sensing application. **Coatings**, v. 10, n. 4, p. 378, 2020.

SALAMAT, A.; HECTOR, A. L.; KROLL, P.; MCMILLAN, P. F. Nitrogen-rich transition metal nitrides. **Coordination Chemistry Reviews**, v. 257, n. 13–14, p. 2063–2072, 2013.

SÁNCHEZ-LÓPEZ, J. C.; CONTRERAS, A.; DOMÍNGUEZ-MEISTER, S.; GARCÍA-LUIS, A.; BRIZUELA, M. Tribological behaviour at high temperature of hard CrAlN coatings doped with Y or Zr. **Thin Solid Films**, v. 550, p. 413-420, 2014.

SÁNCHEZ-LÓPEZ, J. C.; MARTÍNEZ-MARTÍNEZ, D.; LÓPEZ-CARTES, C.; et al. Mechanical behavior and oxidation resistance of Cr(Al)N coatings. **Journal of Vacuum Science & Technology A: Vacuum, Surfaces, and Films**, v. 23, n. 4, p. 681–686, 2005.

SAVVIDES, N.; WINDOW, B. Unbalanced magnetron ion-assisted deposition and property modification of thin films. **Journal of Vacuum Science & Technology A: Vacuum, Surfaces, and Films**, v. 4, n. 3, p. 504-508, 1986.

SCHEERER, H.; HOCHE, H.; BROSZEIT, E.; et al. Effects of the chromium to aluminum content on the tribology in dry machining using (Cr,Al)N coated tools. **Surface and Coatings Technology**, v. 200, n. 1-4, p. 203-207, 2005.

SCHMIDT, S.; CZIGÁNY, Z.; WISSTING, J.; et al. A comparative study of direct current magnetron sputtering and high power impulse magnetron sputtering processes for CNx thin film growth with different inert gases. **Diamond and Related Materials**, v. 64, p. 13–26, 2016.

SERRO, A. P.; COMPLETO, C.; COLAÇO, R.; et al. A comparative study of titanium nitrides, TiN, TiNbN and TiCN, as coatings for biomedical applications. **Surface and Coatings Technology**, v. 203, n. 24, p. 3701-3707, 2009.

SHAN, L.; WANG, Y.; LI, J.; JIANG, X.; CHEN, J. Tribology International Improving tribological performance of CrN coatings in seawater by structure design. **Tribiology International**, v. 82, p. 78–88, 2015.

SHARMA, S.; SANGAL, S.; MONDAL, K. On the optical microscopic method for the determination of ball-on-flat surface linearly reciprocating sliding wear volume. **Wear**, v. 300, n. 1-2, p. 82-89, 2013.

SIT, J. C.; VICK, D.; ROBBIE, K.; BRETT, M. J. Thin film microstructure control using glancing angle deposition by sputtering. **Journal of Materials Research**, v. 14, n. 4, p. 1197-1199, 1999.

STUEBER, M.; HOLLECK, H.; LEISTE, H.; et al. Concepts for the design of advanced nanoscale PVD multilayer protective thin films. **Journal of Alloys and Compounds**, v. 483, p. 321–333, 2009.

SUE, J. A.; CHANG, T. P. Friction and wear behavior of titanium nitride, zirconium nitride and chromium nitride coatings at elevated temperatures. **Surface and Coatings Technology**, v. 76-77, p. 61-69, 1995.

THORNTON, J. A. Influence of apparatus geometry and deposition conditions on the structure and topography of thick sputtered coatings. **J Vac Sci Technol**, v. 11, n. 4, p. 667-670, 1974.

THORNTON, J. A. Structure-Zone Models Of Thin Films. **Modeling of Optical Thin Films**, v. 0821, n. February 1988, p. 95, 1988.

TLILI, B.; MUSTAPHA, N.; NOUVEAU, C.; et al. Correlation between thermal properties and aluminum fractions in CrAlN layers deposited by PVD technique. **Vacuum**, v. 84, n. 9, p. 1067-1074, 2010.

TSUI, T. Y.; PHARR, G. M.; OLIVER, W. C.; et al. Nanoindentation and nanoscratching of hard

carbon coatings for magnetic disks. **Materials Research Society Symposium - Proceedings,** v. 383, p. 447, 1995.

TUNG, H. M.; HUANG, J. H.; TSAI, D. G.; AI, C. F.; YU, G. P. Hardness and residual stress in nanocrystalline ZrN films: Effect of bias voltage and heat treatment. **Materials Science and Engineering A**, v. 500, n. 1-2, p. 104-108, 2009.

TWARDOWSKI, P.; LEGUTKO, S.; KROLCZYK, G. M.; HLOCH, S. Investigation of wear and tool life of coated carbide and cubic boron nitride cutting tools in high speed milling. **Advances in Mechanical Engineering**, v. 7, n. 6, 2015.

VAZ, F.; REBOUTA, L.; GOUDEAU, P.; et al. Structural transitions in hard Si-based TiN coatings: The effect of bias voltage and temperature. **Surface and Coatings Technology**, v. 146-147, p. 274-279, 2001.

WANG, L.; ZHANG, G.; WOOD, R. J. K.; WANG, S. C.; XUE, Q. Fabrication of CrAlN nanocomposite films with high hardness and excellent anti-wear performance for gear application. **Surface and Coatings Technology**, v. 204, n. 21–22, p. 3517–3524, 2010.

WANG, Y. X.; ZHANG, S.; LEE, J. W.; LEW, W. S.; LI, B. Influence of bias voltage on the hardness and toughness of CrAlN coatings via magnetron sputtering. **Surface and Coatings Technology**, v. 206, n. 24, p. 5103–5107, 2012.

WASA, K.; HAYAKAWA, S.; KIYOTAKA WASA; SHIGERU HAYAKAWA; et al. **Handbook of Sputter Deposition Technology: Principles, Technology, and Applications**. William Andrew, 1992.

WEN, M.; TIAN, H. W.; HU, C. Q.; ZENG, Y.; MENG, Q. N. Modulation periodicity dependent structure , stress , and hardness in NbN / W2N nanostructured multilayer films. **Journal of Applied Physics**, v. 109, n. 12, p. 123525, 2011.

WEST, G.; KELLY, P.; BARKER, P.; MISHRA, A.; BRADLEY, J. Measurements of deposition rate and substrate heating in a HiPIMS discharge. **Plasma Processes and Polymers**. v. 6, n. S1, p. S543-S547, 2009.

WINDOW, B.; SAVVIDES, N. Charged particle fluxes from planar magnetron sputtering sources. **Journal of Vacuum Science & Technology A: Vacuum, Surfaces, and Films**, v. 4, n. 2, p. 196-202, 1986.

YASHAR, P. C.; SPROUL, W. D. Nanometer scale multilayered hard coatings. **Vacuum**, v. 55, p. 179–190, 1999.

ZENG, X. T. TiN/NbN superlattice hard coatings deposited by unbalanced magnetron sputtering. **Surface and Coatings Technology**, v. 113, n. 1-2, p. 75-79, 1999.

ZHANG, K.; DENG, J.; GUO, X.; SUN, L.; LEI, S. Study on the adhesion and tribological behavior of PVD TiAlN coatings with a multi-scale textured substrate surface. **International Journal of Refractory Metals and Hard Materials**, v. 72, p. 292-305, 2018.

ZHANG, L.; ZHUO, M.-J.; XU, J. Enhancing bulk metallic glass formation in Ni–Nb–Sn-based alloys via substitutional alloying with Co and Hf. **Journal of Materials Research**, v. 23, n. 03, p. 688–699, 2008.

ZHOU, F.; CHEN, K.; WANG, M.; et al. Friction and wear properties of CrN coatings sliding against Si 3 N 4 balls in water and air. **Wear**, v. 265, p. 1029–1037, 2008.

ŽIVIĆ, F.; BABIĆ, M.; MITROVIĆ, S.; TODOROVIĆ, P. Interpretation of the friction coefficient during reciprocating sliding of Ti6Al4V alloy against Al2O3. **Tribology in Industry**, v. 1 , 2011.